NTNU – Trondheim
Norwegian University of
Science and Technology

In-Situ Tensile Testing Combined with EBSD Analysis of Ti-6Al-4V Samples from Components Fabricated by Additive Layer Manufacture

Martin Borlaug Mathisen

Preface

This work has been carried out at the Norwegian University of Science and Technology (NTNU), Department of Materials Science and Engineering, as a master thesis within the field of physical metallurgy.

Martin Borlaug Mathisen

Trondheim, June 2012

Acknowledgements

Acknowledgements

NTNU

Abstract

ALM-based production of Titanium components shows great promise in supplying cost-effective products within industries such as energy, chemical processing and aerospace. In common for all is high quality demands. This necessitates extensive research into the intricacies of this production process. Complex microstructures comprised of columnar remnants of directionally solidified β-Titanium, with interior inhabited by colonies of finer α-plate structures were found in samples produced by layered plasma welding of alloy Ti-6Al-4V. Utilising the powerful characterisation tool of in-situ tensile tests combined with EBSD analysis allowed qualitative correlation between microstructural features and deformation characteristics. Non-uniform deformation occurs due to a strong variation of strain response between colonies. Prismatic and basal slip systems are active, with the prismatic systems contributing to the most severe deformation through coarse, widely spaced slip bands. Certain colonies behave as microstructural units, with easy slip transmission across the entire colony. Other colonies show significant deformation mismatch, with local build up of strain gradients and stress concentration. Segmentation occurs due to the growth morphology imposed by the columnar grains. Tensile tests perpendicular to columnar structures reveal strong deformation localization. Connections are made between the peculiarities of the production process and the observed microstructure and deformation mechanisms.

Sammendrag

(Norwegian)

Produksjon av titankomponenter ved lagvis deponering av metall er spådd å kunne levere kostnadseffektive komponenter innenfor bransjer som olje og gass, kjemisk prosess og luftfart. Fellesnevneren er meget høye kvalitetskrav. Dette nødvendiggjør omfattende studier av denne ofte veldig komplekse produksjonsprosessen. En sammensatt mikrostruktur dominert av søylekorn dannet ved rettet størkning av β-Titan, som innlemmer kolonier av α-plater ble funnet i prøver produsert ved lagvis plasmasveising av legeringen Ti-6Al-4V. Ved a ta i bruk det kraftige karakteriseringsverktøyet som oppnås i koblingen av in-situ strekktesting og EBSD analyse kan det trekkes kvalitative slutninger rundt mikrostrukturelle forhold og deformasjonsmekanismer. En ujevn deformasjon grunnet varierende tøyningsrespons i kolonistrukturene observeres. Prisme- og basalplan akkomoderer slip. Slip langs prismeplan observeres å gi de største omveltningene i strukturen, gjennom dislokasjonsvandring langs grove, vidstrakte sliplinjer. Enkelte kolonier fremviser uniform deformasjon og opptrer som en mikrostrukturell enhet (krystall). Andre kolonier innehar korn med misforhold i tøyningsrespons som gir lokal spenningsansamling. Tøyning på tvers av søylekorn gir lokalisert deformasjon. Koblinger mellom produksjonsprosessens særegenheter og den observerte mikrostruktur og tøyningsrespons skisseres i denne studien.

Abbreviations list

ALM	Additive Layer Manufacture
BOR	Burger's Orientation Relationship
HCP	Hexagonal Close Packed
BCC	Body Centered Cubic
HAZ	Heat Affected Zone
RT	Room Temperature
CRSS	Critical Resolved Shear Stress
GND	Geometrically Necessary Dislocation
FESEM	Field Emission Scanning Electron Microscope
PPS	Patterns Per Second
SE	Secondary Electron
IPF	Inverse Pole Figure
OIM	Orientation Imaging Microscopy
SEM	Scanning Electron Microscope
FPS	Frames Per Second

NTNU

Table of contents

1 Introduction

A predicted upturn in the aerospace industry and increased use within areas such as energy, chemical processing and medicine sees the demand for complex titanium components increase significantly. Looking at the field of aerospace, the most striking aspect of recent development is the departure from traditional materials in modern civil aircrafts. Taking Boeings 787 and Airbus' A350 as examples, the modern aircraft fuselage is dominated by composite materials, comprising as much as 50% of the total aircraft weight [1]. The use of carbon-fiber based composites, in turn, favours Titanium for components previously fashioned from Aluminium due to the unfavourable galvanic- and thermal coupling of Aluminium and Carbon.

 As weight saving is essential when building aircrafts, most components are usually complex, hollowed out shapes with walls, webs and ribs rather than solid metal shapes. Castings are generally not accepted for structural parts in Titanium due to the frequent occurrence of solidification defects[2] , this means significant machining of pockets and contours in forged titanium billets is required. Titanium, and especially its aero grade alloys are considered difficult and costly to machine. The machining need as these new, high Ti aircrafts are introduced is so large that it has been questioned if the worldwide capacity for Titanium machining is able to meet requirements[3].

Development of processes based on additive layer manufacture(ALM) of intricate Titanium components is motivated by market evaluations similar to those presented above. These processes have in common that they are based on fusing of several layers onto a substrate in order to arrive at a complex, three-dimensional near-net-shape. This means that the machining need is cut from as much as 95% in the case of some forgings [4], to below 10%, depending on the ALM process in question. Such processes also reduce lead times dramatically, meaning new product designs or prototypes can be manufactured in a very short time compared to conventional forging- or casting-based production routes. Design alterations can also be implemented at any stage without long delays in the production cycle.

In order to meet the rigorous demands of modern aircraft builds, extensive research into microstructural features and the related mechanical properties of the produced components is of great importance. Tuning the process parameters to achieve an optimal combination of mechanical properties will be essential in meeting requirements. This is especially true when one considers the strong sensitivity of titanium alloys in the relation between microstructure and properties, and the complex metallurgical reactions taking place during such a production process. Ultimately, thermal and microstructural modelling of the process will be a priority, with predictability and standardisation as incentives.

The report at hand contains results from analysis and characterisation of samples delivered by the company Norsk Titanium Components AS. They are looking to commercialise a plasma-weld based ALM production process with a view to deliver cost-competitive, high-performance components to the aerospace industry. Reference is made to previous work, [5], for a closer description of this process.

In-situ EBSD study of strained tensile specimens was employed in this study, to investigate the behaviour of the complex microstructures obtained in the ALM plasma fusion process. EBSD techniques can yield extensive information on microstructural features, mapping morphology, phase distribution and crystallographic orientation. Combining this with in-situ loading makes this a powerful tool for relating microstructure and mechanical properties in a direct way at the micro-level.

2 Theoretical foundations

To build an understanding of microstructural configurations and the associated strain response, both general Ti-alloy metallurgy and specifics related to the ALM process will be discussed. For in-depth discussion of microstructure evolution, and any quantitative treatment of grain growth, references are made to other works throughout the following sections. The experimental procedure in this work is focused on the connection between microstructure and mechanical properties, while quantitative descriptions of the production process is beyond the scope of this report due to the complexity and limited specific knowledge about the fabrication of the received samples (production parameters are not disclosed).

Finally, important aspects of experimental procedures utilised in this work will be highlighted.

2.1 Phase transformations in α/β-alloys

Titanium alloys exhibit a diverse range of thermochemical reactions. The high reactivity of Titanium means solid solutions are formed with many elements, enabling extensive alloying. A change of crystallographic configuration occurs as the low temperature, HCP-structured α-Ti allotrope transforms to the BCC-structured β-Ti allotrope. The transformation takes place at a temperature which is strongly dependant on solute contents and affords further possibilities for manipulation of microstructure through thermomechanical or thermochemical processing. With this diversity of possible outcomes follows demands for strict control over all processes involved. Relevant mechanisms for growth of microstructures and resulting mechanical properties are presented in the following. Specifics related to the Ti-6Al-4V alloy are of special interest and will be the basis for all theory and later discussion.

Allotropic transformations give a change in crystal structure. In pure titanium, the HCP-structured α-phase is stable up to a temperature of 882°C [6]. Above this temperature, titanium has a BCC structure. Crystal lattices are shown in Figure 1.
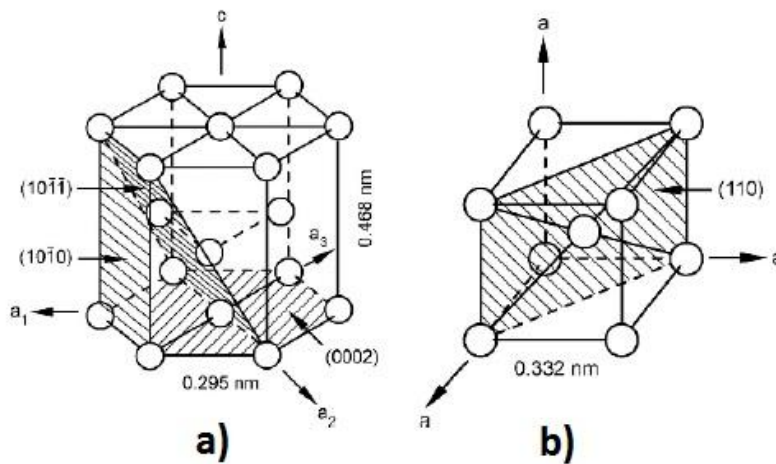
Figure 1: Crystal lattices of the two Titanium allotropes with densely packed planes indicated(hatched). a)α -Titanium, b)β -Titanium[6].

The study of phase transformations in Ti and its alloys is interesting, in part because of the multitude of reactions as discussed above, but also because of the characteristic strict adherence to the orientation relationship originally postulated by Burgers[7]:

$$(110)_\beta \parallel (0002)_\alpha$$

$$[111]_\beta \parallel [11\overline{2}0]_\alpha$$

This is referred to as Burger's orientation relationship(BOR).Planes $(110)_\beta$ and $(0002)_\alpha$ are close packed planes, indicated in Figure 1. The second line gives the crystallographic directions of this relationship. The two $<111>_\beta$ directions lying in a given $(110)_\beta$ plane transforms to two close packed directions of type $[11\overline{2}0]_\alpha$ in the basal plane of the HCP lattice. The third $[11\overline{2}0]_\alpha$ direction coincides with the $[100]_\beta$ direction of the parent β-lattice. This is the relationship which involves the minimum distortion and rotation of the lattice vectors [8]. The transformation from BCC to HCP involves selection of one out of 12 variants, while HCP to BCC result in one of 6 possible orientation variants. The distorted hexagonal lattice in the parent BCC crystal is represented schematically in Figure 2.

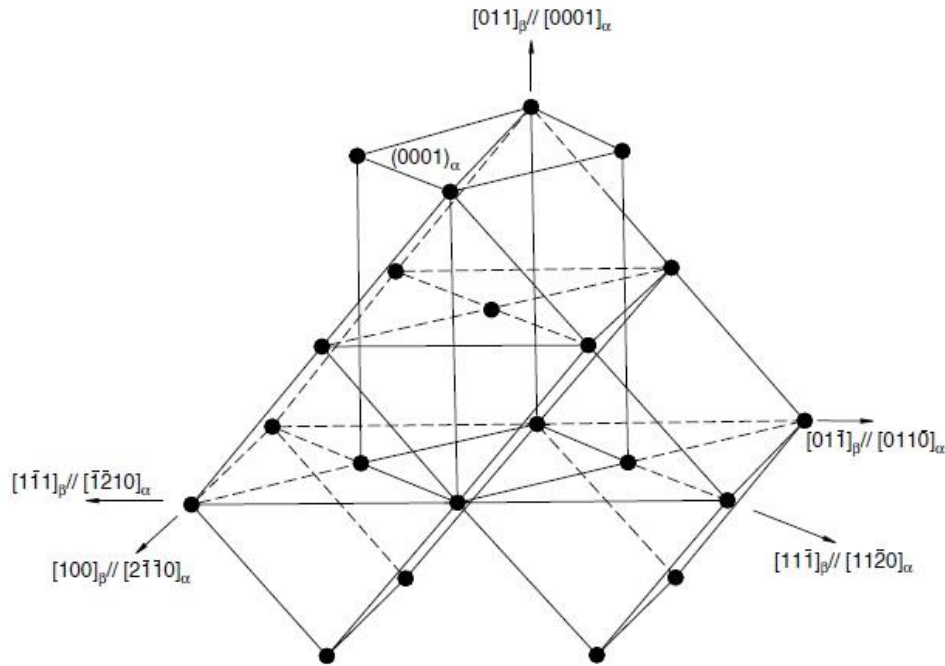**Figure 2:A segment of the HCP α-Ti cell and its relation to the BCC β-Ti lattice [8]**

This strict adherence to the orientation relationship, combined with the lower symmetry of the HCP cell, results in the high resistance to recrystallization observed in α+β titanium alloys[9]. This is caused by the β-fragments retained after cooling, which upon reheating acts as the embryos for regrowth of β-grains. All fragments within a previous β-grain share the same orientation. The significance of lower symmetry of the HCP cell stems from a minimal tendency for relaxation and grain reorientation, meaning that the β-fragments will grow and recombine to a single grain, and previous β-grains are recovered. The HCP to BCC transformation involves a simple shear movement at relatively low stress levels, which means that the orientation relationship is less likely to be broken. This contrasts with steel metallurgy, where the grain size of the high temperature crystallographic modification (Austenite) can be refined through rapid heating above the transformation temperature. This promotes nucleation and growth of several new austenite grains within one previous grain[9]. As nucleus grows, lattice stresses are relaxed through formation of orientationally random grains. Prolonged exposure to temperatures above the β-transus can give significant grain growth in Titanium. While in steels, recrystallisation can occur in the austenite temperature region as a result of the high dislocation density stemming from the stress intensive allotropic transformation.

The mechanism of recrystallisation induced by stored energy in the form of dislocations is well documented and often exploited in the production process of titanium components [6]. This does, however, require a mechanical component to the fabrication, such as rolling or extrusion. Without severe plastic deformation, dislocation density will not be high enough[9].

Binary phase diagrams for systems Ti-Al and Ti-V are presented in Figure 3 and Figure 4. Ti-V is an isomorphous-type binary system. In an isomorphous system there is complete liquid and solid solubility. This is the case when the elements, such as Ti and V, have the same crystal structure (both V and β-Ti are BCC structured), similar atomic radii, electronegativity and valence (Ti and V are neighbours in the periodic system, atomic numbers 22 and 23 respectively). Ti-Al is a peritectoid-type binary system. In this system, intermetallic compounds are formed in what is called ordering reactions. In complete solid solution, for example in the β-region of the Ti-V system, the solute elements (V in that system) are randomly distributed in the Ti lattice. Ordering occurs when a system shows a preference for certain constellations of bonds. For Ti_3Al, the most relevant for Ti-6Al-4V alloy, this entails an atomic arrangement where Al has only Ti atoms as its nearest neighbours in a superlattice (a derivate from the HCP structure). A detailed treatment of ordering in the Ti-Al system can be found in [8](chap 5.2.6). Al content in commercial alloys is often limited to 6% to avoid widespread precipitation of Ti_3Al, as it acts as a stress riser and crack initiation point because of its coherent relationship with the matrix structure(i.e. easy slip transfer)[6].
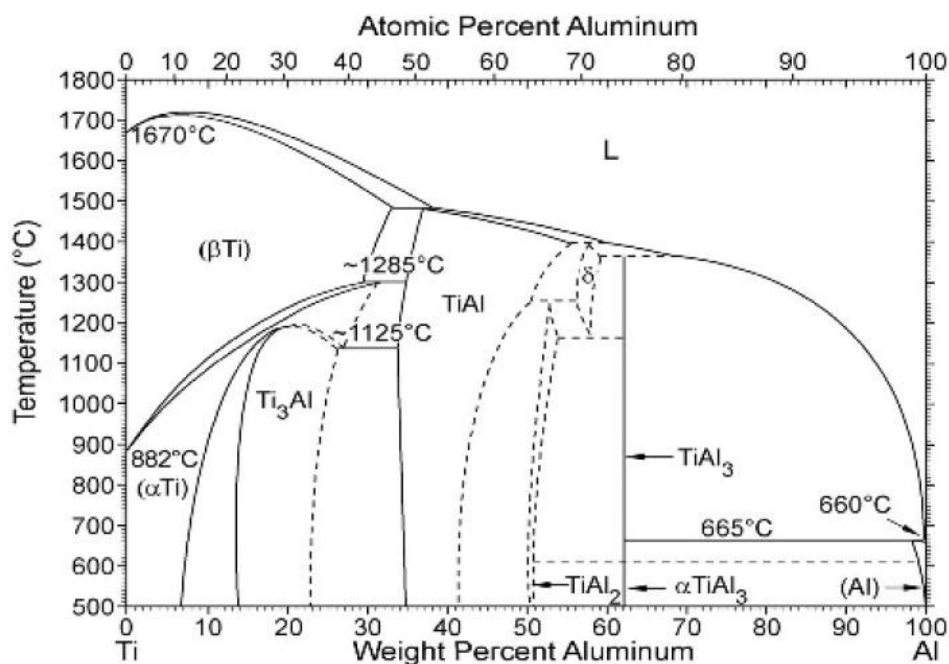
Figure 3: Binary phase diagram; Ti-Al system[6].
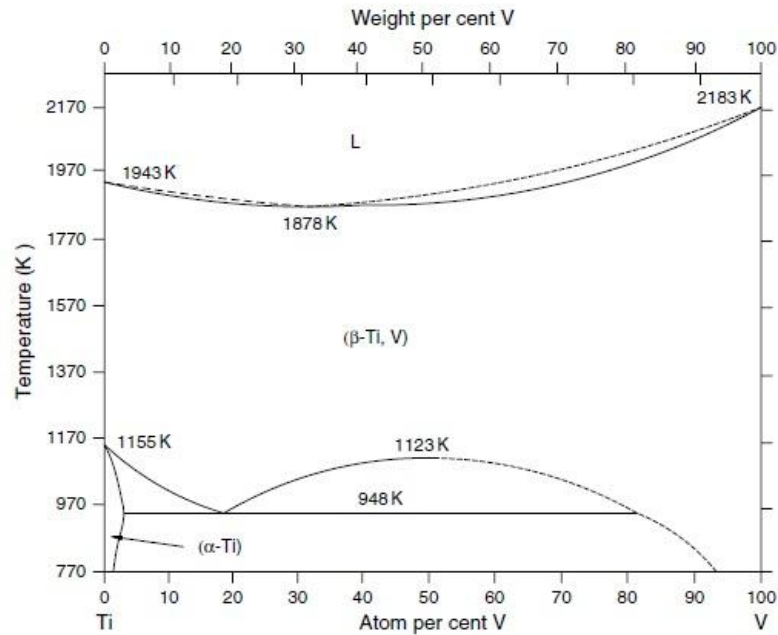
Figure 4: Binary phase diagram; Ti-V system(temperature in kelvin) [8].

In [10], pseudobinary phase diagrams for the Ti-6Al-4V alloy system were calculated (utilising Thermocalc software). This shows the influence of varying the content of each of the two main alloying elements, V or Al, while the other is kept at a fixed concentration (4wt% for V and 6wt% for Al). These diagrams are shown in Figure 5.
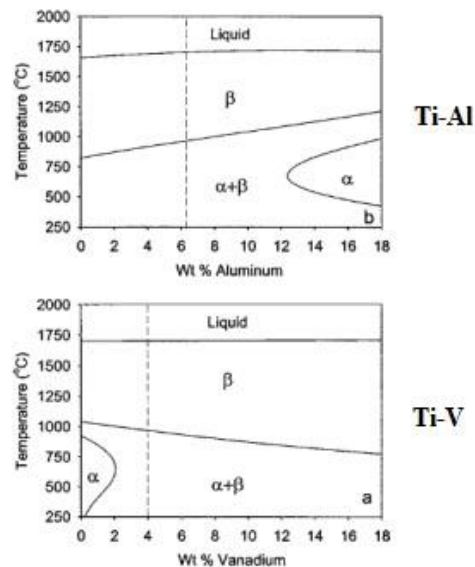
Figure 5: Pseudobinary phase diagrams for the Ti-6Al-4V alloying system [10]

As is apparent from Figure 5, increasing content of V stabilises the β-phase by lowering the transus temperature, while Al has the opposite effect. In the Ti-6Al-4V alloy, and all other commercial α+β-alloys, the β-phase is only present in metastable form at room temperature.

For β to be stable at room temperature, V content in a binary alloy needs to be as high as 15wt% [11].

Oxygen acts as an effective lattice hardener by occupying interstitial sites in the HCP cell [12]. The solubility of O in Ti is as large as 30 atom%[13]. Even if this is the case, the distribution is not necessarily random as one suspects in complete solution. Tendencies for ordering has been apparent within this range of oxygen content (up to 30 atom%). In [14] it was found that ordering of Oxygen can take place in Ti-6Al-4V alloys under low temperature aging treatments (around 350°C). At this temperature oxygen has a certain mobility while substitutional elements such as Al and V require higher temperatures to activate high diffusion rates. At higher aging temperatures, around 550°C, precipitation of Ti_3Al can occur. This reaction was favoured at higher oxygen contents[14].

2.1.1 Solidification

In liquid Titanium, diffusion rates are high relative to solid states. For any small volume of liquid, such as the melt pool formed during welding, the chemical composition will be uniform. As solidification sets in, the nature of this reaction will be governed by the local composition ahead of the solidification front and the local temperature gradient.

In alloys, the solidification morphology is influenced by partitioning of solute elements and resulting fluctuations in local melting points across the solid/liquid interface. There will be a build up of solute elements ahead of the solid front if the solubility in the solid is lower than in the liquid phase, as is apparent from the dotted lines in Figure 6 for the system Ti-Fe, and to a lesser extent Ti-Al (Figure 3) and Ti-V (Figure 4). The composition of the Ti-6Al-4V alloy studied in this work is shown in Table 3 in chapter 3. This indicates the presence of Fe.
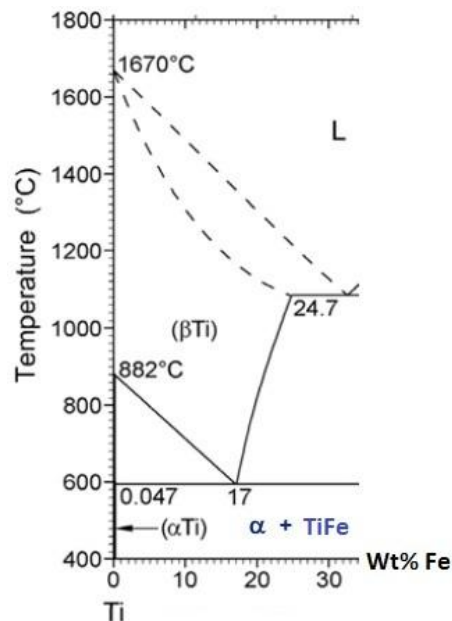
Figure 6: Section of the equilibrium phase diagram for the system Ti-Fe [11]

The solute build up is a driving force for breakup of the plane solid front, even if the heat flow is constant. If the substrate is known to be the heat sink, as is the case for most ALM processes, the solid front growing towards a positive temperature gradient is stabilised. But the solute pile-up in alloys means protrusions in the plane interface may continue to grow due to increased local pile-up, giving undercooled liquid (ref.Figure 7b). In this case cellular or dendritic (at higher undercooling) morphology is promoted.
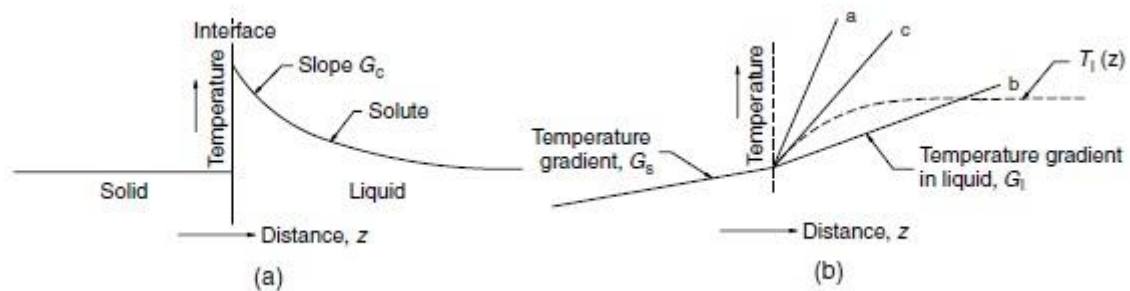
Figure 7: Conditions for constitutional undercooling [8]

This means that high growth rates promote breakup of the solidifying front into cellular (finger-like) or dendritic morphologies when solubility in the liquid phase is higher, such as in the Ti-Fe system. The continued growth of these perturbations is accelerated due to the ability to shed solute normal to the growth direction.

2.1.2 Solid state transformations

As the temperature falls below the β-transus, an allotropic transformation in one of the various guises presented in Figure 8 sets in. The alterations associated with this transformation are superimposed on the solidification structure.
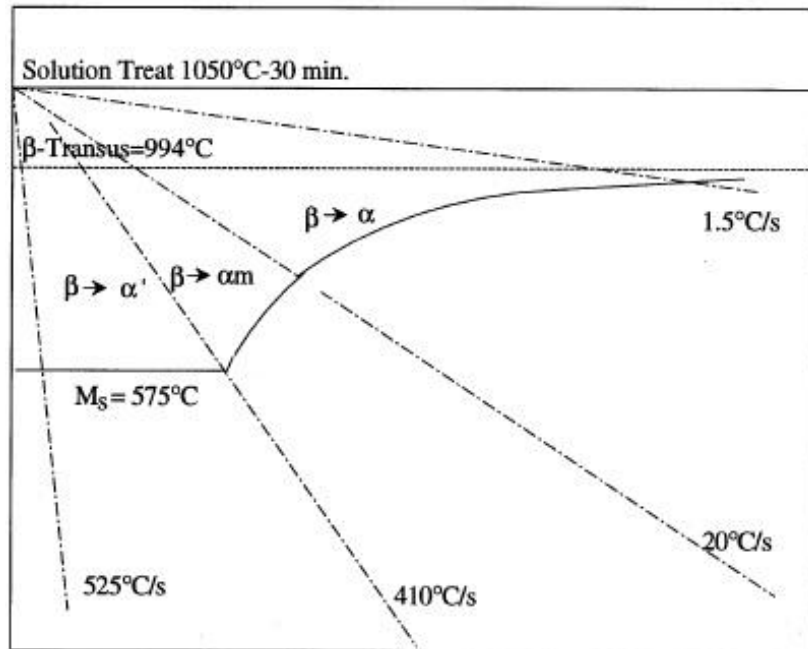
Figure 8: Phase transformation regimes at different cooling rates in alloy Ti-6Al-4V. α'=martensite, αm="massive" α, α=equilibrium α. From [15].

The massive transformation has a lot in common with the martensite transformation. It produces a slightly different, blocky morphology at β-grain boundaries, with high internal dislocation density. The structure inherits the composition from the parent phase. The process is, in contrast with martensitic transformations, diffusion controlled. As the grain grows diffusional jumps across the interface of the growth front control its propagation. The massive transformation is thought to occur mainly in aluminides or systems Ti-Ag, Ti-Au and Ti-Si [8], so it is of minimal interest in this study. Reference is made to [15] for further discussion.

Martensite transformation

This is a non-equilibrium transformation that takes place through diffusionless, cooperative movements of atoms. No thermal activation is involved, so that quenching will not suppress these transformations. In low alloyed systems, the HCP martensite modification referred to as α' will form. With increasing β-stabilising solute content, there is a distortion of the lattice in the resultant martensite, towards the orthorhombic modification α''. Compared to ferrous systems, the driving force necessary to induce martensite transformations in Ti-alloys is far lower. This is due to a significantly lower shear modulus at the transformation temperatures and the nature of the lattice strain during the transformation, which involves far less

inhomogeneous shear due to the crystallographic relation between the parent and the product lattice[8].

The Titanium martensite reaction is associated with significantly lower stress levels. Although martensite in Ti produces a high dislocation density, it is softer than martensite in steels[6]. The lattice strains due to supersaturation are lower because of the modest distortion of the hexagonal lattice produced by interstitial O relative to C or N in Fe.

The so called massive- or packet martensite which forms in low alloyed systems takes on the form of coarse irregular colonies populated by ordered, parallel arrays of small platelets. Higher alloying gives the more disordered acicular morphology, where each lath has its own orientation given by BOR.

The martensite start temperature, M_s, for Ti-6Al-4V alloy lies at around 600°C (650°C reported in [10], while [15] states 575°C). The exact temperature is dependent on the chemical inhomogeneity of the β-phase. Entirely martensitic structure has been found in samples exposed to cooling rates higher than 410°C/s [15].

Diffusional transformations

Upon cooling from the β-phase field, α-phase will form and grow along one of twelve possible orientations, dictated by the burgers orientation relationship, presented as **Feil! Fant ikke referansekilden.**. α precipitates semi-coherently [16] and preferentially along high-angle β-grain boundaries, forming a Burgers orientation relationship with one of the grains along the boundary due to the associated reduction in interfacial energy. Semi-coherency entails existence of some misfit dislocations along the grain boundaries. In special cases, where the misorientation of prior β-grain allow, α obeys/approximates Burgers relation with both grains[8]. A tendency for low energy facets of the hexagonal cell, specifically the basal plane, to align themselves with the previous β-grain boundaries has been observed[8]. This occurs within the confines of the BOR, meaning certain variants are preferred.

α-plates in parallel grow as colonies of plates into β-grains from the grain boundary α, or straight from the previous β-grain boundary. These plates, forming the basketweave widmanstatten morphology, grow with their long direction along former $\{110\}_\beta$-planes[17]. In [18], the growth direction of plates was observed to lie preferentially in the basal plane of the growing HCP crystals for pure Titanium. This is attributed to higher thermal conductivity perpendicular to the c-axis as compared to along it (inferred from electrical resistivity data and Wiedemann-Franz law in original article [18] due to lack of specific thermal data. Wiedemann-Franz law states the proportionality of electrical- and thermal conductivity). Solute elements also have a larger diffusion rate along the c-axis, meaning that shedding of alloy elements to the sides of the plate as growth proceeds is facilitated if the c-axis is perpendicular to the growth direction. Interlamellar β is formed and retained to room temperature as a meta-stable phase. Growth direction and orientation relationships within the colony structure are shown in Figure 9.
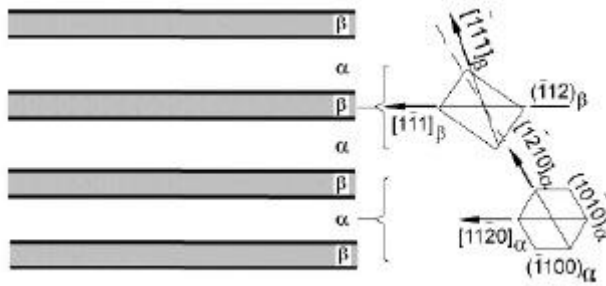
Figure 9: Schematic representation of growing plate colony. From [6].

At high undercooling, associated with high cooling rates, colony size decreases, and an increasing driving force for intragranular precipitation of α is introduced. The width of α-plates is also decreased. These secondary colonies nucleate within the grain interior at some inclusion, or on the side of already formed colonies in what is called *sympathetic nucleation [19]*. Secondary colonies usually grow perpendicular to the original colony to minimise overall elastic strain [6]. The size of grain boundary α decreases slightly with increasing cooling rate, but can never be completely avoided[6, 17]. Very slow cooling rates favour higher diffusion and blocky α-grains can form by a more uniform growth mechanism within prior β-grains [17].

2.1.4 Multiple layer welding and epitaxial growth

As layer upon layer is fused together to build component shapes, previous layers are sequentially reheated and cooled. Different segments receive different heating rates, peak temperatures and cooling rates. This will bring about further changes to the already deposited metal.

In fusion welds, dendrites are often observed towards the weld centreline, where undercooling is the highest [20, 21]. Some methods, such as laser beam, electron beam or resistance welding give a low energy input and result in regions in HAZ with very high cooling rate(100-10000 °C/s). In these regions needle or plate like martensite is usually found, as discussed in the previous chapter. Gas-tungsten, gas metal or plasma arc welding give a higher energy input, and cooling rates of 10-100 °C/s produce a characteristic widmanstatten structure plus retained β. A mixture of this structure and equiaxed α-prime is also found, depending on the time of exposure to elevated temperatures giving rise to alloy element partitioning and growth of equiaxed α. Equiaxed prime-α in a matrix of transformed β originating from the base metal is found in the outer regions of HAZ[2].

For any partial melting process such as welding, the tendency for ordering of solidification products at the solid/liquid-interface imparts another important constraint. This is known as epitaxial growth. A low crystal lattice mismatch is associated with lower surface energy at any interface between existing solid and freshly solidified layers. At such an interface,

partially melted grains in what is known as the mushy zone [20], begin to grow into the liquid pool. The crystallographic orientation of growing grains is inherited from the solid surface in this region. Titanium solidifies as BCC structured β-Ti. The β-phase has preferential directions of growth corresponding to <001> [8, 20]. The phenomenon of epitaxial growth, preferred growth directions, unidirectional heat flow and sequential reheating of some segments in sum leads to certain likely traits of the morphologies. The nature of these traits depend strongly upon the process parameters.

2.2 Microstructure and strain response

Crystal structure, mechanical metallurgy and important microstructural features in Ti-6Al-4V will be discussed in the following sections.

2.2.1 Single crystals

Crystalline materials accommodate plastic deformation along certain planes and directions within the crystal lattice. In a perfect crystal, every node in a network of bonds is occupied by an atom, an ion or a molecule. In what is conventionally referred to as *slip*, plastic strain occurs by a dislodging of a series of nodes across a crystal plane. Relative movement along the interface of the slip plane alters the shape of the crystal. As a general rule, such slip activity occurs preferentially along the most densely packed planes, propagating along densest directions. A shorter distance between nodes means that dislodging and reforming of bonds to produce relative motion occurs more readily as each jump is shorter.

The unit cells of α-Ti and β-Ti are presented in Figure 10 a) and b) respectively. The active slip systems are indicated in this figure(hatched areas) and presented in Table 1 and Table 2.
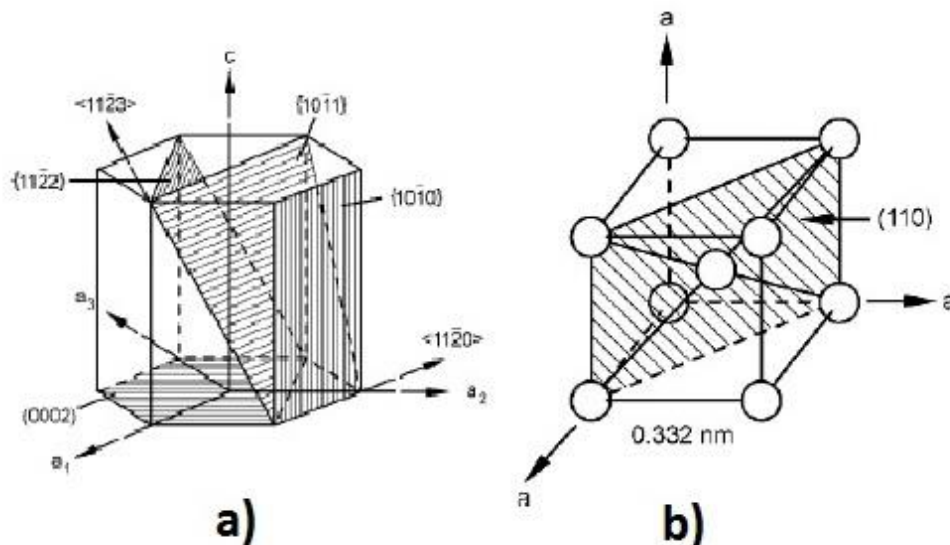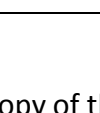

Figure 10: a) HCP unit cell of α-Ti and b) BCC unit cell for β-Ti. Hatched areas indicate active slip planes. Complete presentation of slip planes in Table 1 and Table 2.

Deformation in α-Ti

Of greatest importance for strain response in Ti-6Al-4V at RT, is the HCP structured α-phase.

Slip plane No. of variants		Slip direction No. of variants	Total no of slip systems Designation	Approximate relative CRSS
$\{0001\}$ 1		$< \bar{2}110 >$ 3	3 'Basal'	1
$\{01\bar{1}0\}$ 3		$< \bar{2}110 >$ 1	3 'Prismatic'	0,7
$\{01\bar{1}1\}$ 6		$< \bar{2}110 >$ 1	6 'First-order pyramidal'	3
$\{11\bar{2}2\}$ 6		$< 1\bar{1}00 >$ 1	6 'Second-order pyramidal'	-
$\{11\bar{2}2\}$ 6		$< \bar{2}113 >$ 2	12 '<c+a> pyramidal'	-

The inherent anisotropy of the α-Ti crystal structure comes with important implications for deformation mechanisms. The elastic modulus for tension along the c-axis is in the region of 145 GPa, while it is only 100 GPa perpendicular to the c-axis [6]. When a single crystal of pure Titanium is stressed beyond the yield point, anisotropy manifests itself through the selective activation of slip systems.

As mentioned, the tendency for slip is greater in dense directions along densest crystal planes. The Ti HCP unit cell has a lower c/a ratio than the archetypal hexagonal cell (1.587 compared to 1.633). This compression along the c-axis gives a closer packing of nodes in the prismatic planes (ref. Table 1). These planes, along with the basal planes, are the primary slip planes. The direction of slip is along $< 11\bar{2}0 >$-directions in the basal plane (often $[\bar{2}1\bar{1}0]$ is used to signify what in principle is an equivalent direction due to the symmetry of the cell. How it is denoted is arbitrary in this context).

To quantify how susceptible any given slip system is to activation, two terms are considered. Firstly, the critically resolved shear stress (CRSS) is the in-plane stress component required to cause dislocation movement. This value varies with temperature and alloying content. Second, the geometric relation between the slip plane and the applied stress needs to be

defined. The Schmid factor is commonly used here. This coefficient denote how much of the shear stress is resolved into the slip plane and thereby acting towards dislocation propagation along the slip line (For information, the Schmid factor is defined in Appendix A).
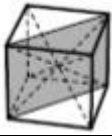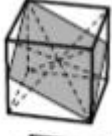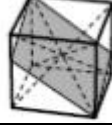
In Ti-6Al-4V, at room temperature, it is generally agreed that the CRSS is lowest for the prismatic slip systems. It is only slightly higher for the basal systems, but significantly greater for the pyramidal systems. The relative values of CRSS between slip systems change markedly with solute content and temperature. Additions of Al to beyond 5-6% has been found to promote basal slip[24]. This effect is suspected to be caused by the shorter bond-length of Al atoms changing the relative density of basal and prism planes. The <c+a> type slip has an especially high CRSS value (Table 1). This means that any deformation along the c-axis requires a very high stress. The systems with basal directions have been shown to be preferential at an angle between c-axis and tensile axis of as little as 14° [25].

Twinning is a mechanism commonly explained as shearing of a portion of the crystal to produce deformation while still being related to the rest of the crystal structure in a definite, symmetric manner [26]. The crystal structure is mirrored across the twinning plane. Deformation by twinning is suppressed by additions of Al and O [11], but it is suspected to be of importance in the CP Titanium grades, in particular those with low Oxygen content. The twinning systems commonly observed in Ti produce deformation along the c-axis, and are favoured in crystals loaded parallel to this direction. In [27], a threefold increase in resistance to twinning when going from high purity(HP) Titanium to commercially pure(CP) Titanium was predicted. This underlines the profound influence of impurities and alloying elements on the relative proportion of slip activity in different systems.

Deformation in β-Ti

The higher symmetry and greater number of (almost) equally active slip systems in BCC-structured β-Ti crystals gives a more isotropic character to deformation. The slip systems are given in Table 2.

Table 2 : The slip systems of the BCC structured β-Ti[22].

Slip plane No. of variants		Slip direction No. of variants	No. of slip systems
{110} 6		$< \bar{1}11 >$ 2	12
{112} 12		$< 11\bar{1} >$ 1	12
{123} 24		$< 11\bar{1} >$ 1	24

As β-Ti is stable only at high temperatures unless heavily alloyed, measurements of the elastic modulus are not directly available. A low modulus of 85GPa for quenched β-Ti and 105GPa for heavily stabilised β-Ti (50% V) indicate a generally lower elastic modulus than α-Ti.

2.2.2 Polycrystals

Conventional microstructures constitute several crystals. Each crystal, usually referred to as a grain, has a different *orientation.* This means that the lattice substructure within each grain has a certain alignment with the global coordinate system. Monocrystal effects, namely the anisotropy of the HCP unit cell discussed in the previous subchapter, are thus carried to the microscopic level of the grain structure. If some macroscopic texture is present, meaning that several grains share the same orientation, the anisotropic deformation characteristics can become apparent at the macro level.

If, upon loading, various grains exhibit different ability to accommodate plastic deformation, there is some *deformation mismatch.* This structural incompatibility is considered the most important contributing factor for fracture of Titanium components[28]. *G*rains oriented for easy prismatic or basal slip are deemed *soft*, while *hard* grains tend to have the c-axis oriented along the direction of applied stress[29], where deformation entails activation of the more resilient <a+c>-tyoe systems (Table 1).

Grain interactions and differing local strain responses have been known to cause local stress build up leading to brittle fracture initiation and local faceting during cyclic loading of Titanium alloys [30]. Brittle fracture usually entails transgranular crack propagation after heavy dislocation pile ups. These effects are magnified in coarse-grained structures, while small grain size gives more uniform deformation characteristics [26]. Boundaries between grains are commonly separated into *high angle* and *low angle* boundaries. Low angle boundaries are commonly defined as misorientations below 15°, although the definition is somewhat arbitrary. The important distinction lies in the nature of the interface. High angle grain boundaries contain immobile dislocations forming local irregularities. For lower misorientations the lattice disturbance is reduced. If misorientation is down to around 1°, an ordered array of regularly spaced dislocations can compensate for this misorientation [26]. Strain gradients across boundaries are present during deformation, and the degree of misfit and irregularities determine how steep these gradients are.

Retained β-phase represent barriers to dislocation propagation and small β-inclusions can act as ductile crack arrest sites.

Strain hardening

Strain hardening is caused by the accumulation of dislocations locally at interfaces or in the grain interior. These dislocations act as effective barriers against further dislocation

movement, as pile-ups produce a back stress opposing dislocation motion[26]. All metals contain an appreciable amount of dislocations prior to any deformation. This stems from growth of the crystals and some ever-present misalignment of growth which will always occur due to tiny shifts in gradients of temperature or composition [26]. The irregularities associated with high angle grain boundaries(ledges and steps) will cause emission of dislocations in early stages of plastic flow (Theoretical treatment in [31]). The effect of grain size and interstitial solutes on strain hardening is through their influence on dislocation density [12]. This means that interfaces such as grain boundaries don't have any intrinsic increase in strength, but provides a hardening effect as they interfere with slip systems within and across grains, and also generate dislocation at boundaries. Figure 11 illustrates the model for macroscopic deformation of microscopically anisotropic polycrystals, proposed by M.F. Ashby in [32].
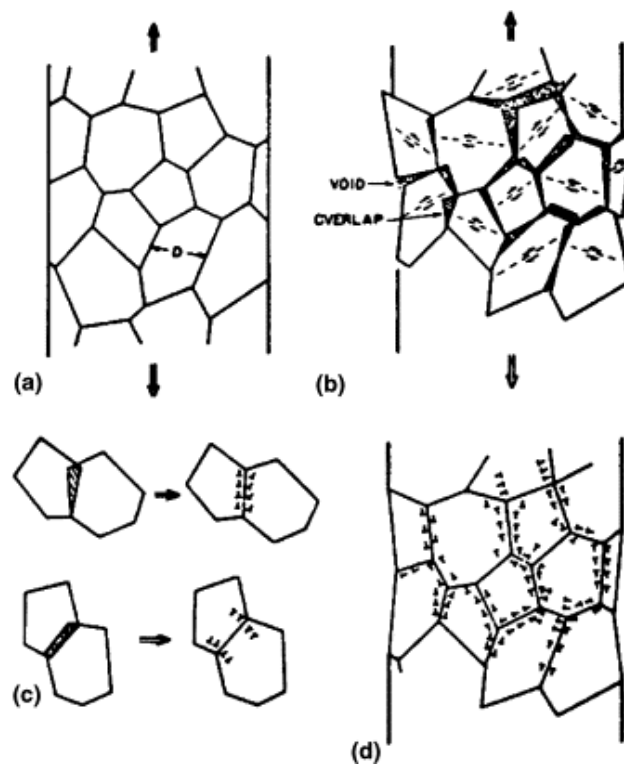
Figure 11: Illustration of how geometrically necessary dislocations compensate for inhomogeneous strain to maintain structural continuity. a) Section of polycrystal under strain. b) Macroscopically uniform deformation produces voids and overlap due to microscopic anisotropic behaviour. c) and d) Geometrically necessary dislocations at grain boundaries compensate for this anisotropy and preserves. From [32].

A finer grain structure would encompass more grain boundary area, thereby producing higher dislocation density and greater strain hardening. The lower strength of coarse grained microstructures is commonly attributed to a higher degree of local dislocation pileups at grain boundaries in large grains, as the number of dislocations along a slip plane is proportional to grain size [22]. Dislocation generation at boundaries is put forth as the primary mechanism for grain boundary strengthening in [33] and [12]. During plastic flow, the cross section area of a tensile specimen is constricted. If the strengthening due to strain

hardening is not enough to compensate for the reduced cross-sectional area, instability and local necking will occur [26].

2.3 In-situ EBSD studies of strained tensile specimens

This chapter aims to deal with some aspects of orientation microscopy and its application for deformed titanium samples. Some general theory and examples of previous work in the same vein as this study will be referenced.

2.3.1 OIM for hexagonal materials

The optical anisotropy of HCP α-Ti means some qualitative orientation information can be obtained using polarised light in an optical microscope [6], but increased awareness of the orientation dependence of mechanical properties have led the way for extensive implementation of OIM-based techniques. Along with this, the EBSD technique has emerged as a powerful tool for analysis of polycrystals.

The EBSD technique is based on diffraction of high-energy incident electrons on atomic planes in a crystalline material. The crystal lattice planes act as mirror-like surfaces giving rise to high-angle backscattered electrons which are diffracted. The diffracted electrons give high intensity bands and form patterns which are imaged on a fluorescent phosphorus screen. A CCD camera behind this screen collects this image. To increase the backscatter signal, the sample is tilted at an angle of 70°. In beam control mode the electron beam traverses a predefined area of interest and diffraction patterns with a set spacing (step size) is collected in each point. This setup is shown schematically in Figure 12.
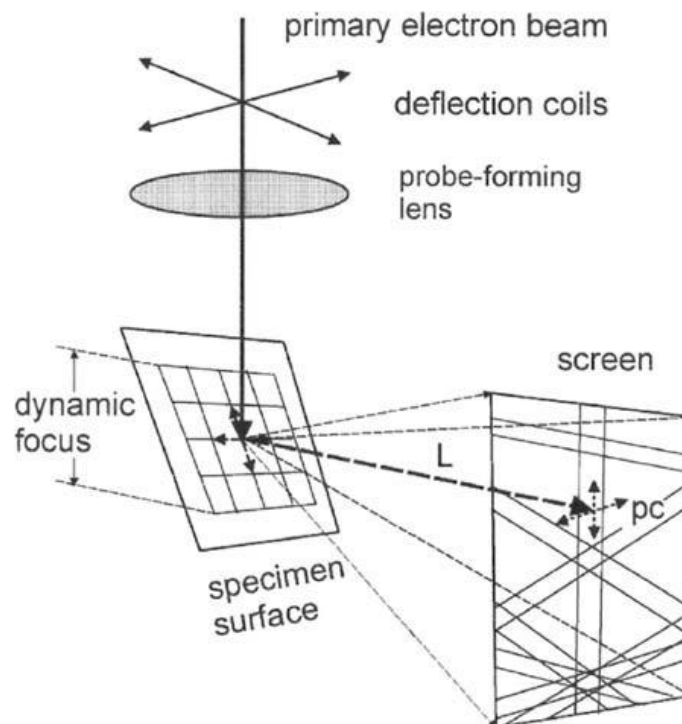

Figure 12: the beam scans the surface according to a raster grid. The diffracted pattern carries information on crystal lattice structure and orientation from each point in the raster. PC, meaning

Pattern Centre, is defined as the normal to the screen which intersects the specimen surface at the point of electron beam impingement.

Alternatively, a stationary beam and a moving stage gives scanning over the desired area of the sample. The patterns which are obtained contain information on crystal structure and orientation. The angles between bands are equal to angles between crystal planes, and the intersections of the bands reflect zone axes in the crystal lattice. In addition, the spatial position of each pattern is logged, to allow mapping of the microstructure. The patterns are correlated with crystallographic axes in known materials in the indexing stage, which can be done alongside pattern aquisition (online EBSD) or after the scan is complete and all patterns are captured and stored for postprocessing (offline EBSD). This means that for indexing of patterns, the phases one expects to find need to be indicated in the indexing software. How distinct the bands are, the band contrast, is quantified by the image quality (IQ) parameter which is also registered for each pattern. Good band contrast requires a high beam current, and, as the emmission volume is less than 100nm deep, a well prepared, deformation free sample surface. CI, or confidence index, is a parameter defined by EDAX, the company behind the OIM analysis software used to process the results. CI is defined in Appendix D.

More detailed description of the principles of EBSD and indexing algorithms can be found in several previous works. Reference is made to [34], chapters 1 and 2.

Combining stage- and beam controlled scanning allows mapping of large areas. An overview of implementation of this technique and representation of orientation data can be found in [5].

2.3.2 Analysis of plastic deformation by EBSD

Elastic strain can be detected by lattice rotations leading to orientation gradients within grains and general degradation of diffraction pattern contrast. EBSD is sensitive to the collective effect of geometrically necessary dislocations. Localised accumulation of GNDs or statistically stored dislocation create lattice imperfections which degrades the EBSD signal or fails to give indexable diffraction patterns alltogether.

For Kernel average misorientation mapping, the arithmetic mean of the scalar misorientation between groups of pixels, or kernels, is calculated and mapped [34]. This gives some indication of strain gradients within grains.

Detection of strain effects of small dimensions is limited by the spatial resolution of EBSD, which is in the order of 10 nm, and the angular resolution of the Hough transform applied during indexing.

3 Experimental

The sample material was received in the form of a large block of welds on a substrate plate (Figure 13). This is a segment from what was to be a circular tool used for "hotbolting". This is a maintenance operation performed on oil pipe-lines where bolts at a flanged pipe connection are changed without shutting down the flow of fluid in the pipe.
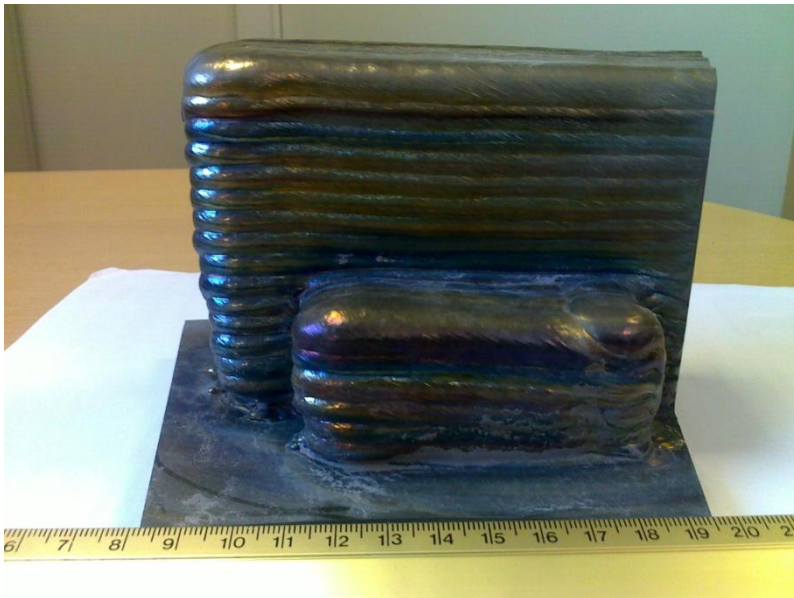
Figure 13: The as-received ALM-manufactured segment. (Photo: SINTEF Manufacturing Raufoss)

The chemistry of the welding wire used in fabrication is given in Table 3.

Table 3: Welding wire chemistry. Mean values for measurements on ingot.

Element	C	Fe	N	O	Al	V	Ti
Mean(wt%)	0,02	0,16	0,02	0,16	6,18	3,98	Bal.

3.1 Preparation of samples for general metallographic and EBSD analysis

This section covers the preparation sequences for the non-tensile specimens. These where analysed to become familiar with the inhomogeneites of the microstructure and determine necessary area for representative scans during in-situ tests.

3.1.1 Cutting

For initial characterisation of the material, samples of about 10x20x4mm where extracted from the received block. Rough cutting was done with a bandsaw, removing a 5mm thick vertical slice from the right hand face of the block in Figure 13. This slice was segmented further using a Struers Discotom 5 cutting machine with Struers abrasive disc type 20S25, for ductile materials. The rotation of the cutting wheel was kept just above 1000 rpm, while the feed rate was kept constant and quite high, estimation: 1mm/s. The cutting machine has water cooling.

3.1.2 Grinding and polishing

For these smaller samples, embedding in PolyFast (Struers) resin was utilised. This sample mounting system is based on a electrically conductive resin (Bakelite with epoxy filler). This enables mounting in automated grinding apparatus Tegra by Struers. The grinding parameters are given in Table 4. The chosen procedure is based on suggestions in [35]. The sample was removed from the resin after polishing. This is easily done by careful mounting in a vice and cracking the resin open with a mallet. This exposes the sample which can be pried out.

Table 4: Parameters used for automated grinding.

Step	Grinding surface	Time	Force per sample	Rotation	Lubricant/suspension
1	220 grit SiC paper	5 min	25 N	300 rpm	Water
2	MD Largo (Struers)	10 min	25 N	150 rpm	9µm grit DP suspension

To achieve a mirror-like surface, chemical-mechanical polishing was performed, with parameters given in Table 5. OPS is an alcohol-silica suspension of grit 0,4 µ. 10 vol% Hydrogen Peroxide solution with 30% H_2O_2 was added as an oxidising agent. This is known to contribute to removal of deformed layers during polishing of Ti. A rinsing step with water was added to remove traces of the solution from the polished surface.

Table 5: Parameters for automated polishing.

Step	Polishing surface	Time	Force per sample	Rotation	Lubricant/suspension
1	MD chem cloth (Struers)	10 min	15 N	150 rpm	OPS + H_2O_2
2	MD chem cloth (Struers)	1 min	10 N	150 rpm	Water

3.1.3 Chemical etching

For examination by optical microscope or in SEM by SE-signal mode, polished samples were submerged in Kroll's reagent (Table 6) for 8 seconds. After etching they were immediately rinsed in ethanol and then water.

Table 6: Kroll's reagent used as macro- and microetchant.

Kroll's reagent
2ml HF
10ml Nitric Acid
88ml Water

3.1.4 Cleaning

After chemical-mechanical polishing(and etching for some specimens), thorough rinsing in ultrasonic aceton bath was performed. Cleaning times of 10 minutes. Samples were then flushed with ethanol. All samples where cleaned in a Fischione Model 1020 plasma cleaner as a final step before insertion into SEM. Cleaning time 5 minutes. Samples where handled with rubber gloves after this final cleaning step.

3.1.5 Ion sputtering

For samples destined for EBSD analysis, Ion sputtering was performed in a HitachiIM-3000 ion mill. This method can be used as a stand-alone final surface preparation after mechanical polishing, but here it was only used lightly as more of a rinsing than eroding process. Lightly meaning that high tilt angle and relatively short time was employed in order to flush the surface clean of contaminants. Parameters are presented in Table 7.

Table 7: Parameters used during ion milling.

Accelerating voltage	3,5
Tilt angle	85
Eccentricity	2-4 mm (maximum)
Time	5-15 min

3.2   Preparation of tensile-test samples for in-situ analysis

The tensile test stage and it's fixing brackets are designed for a specific rectangular profile tensile specimen. The geometry of this is given in Figure 15 b.
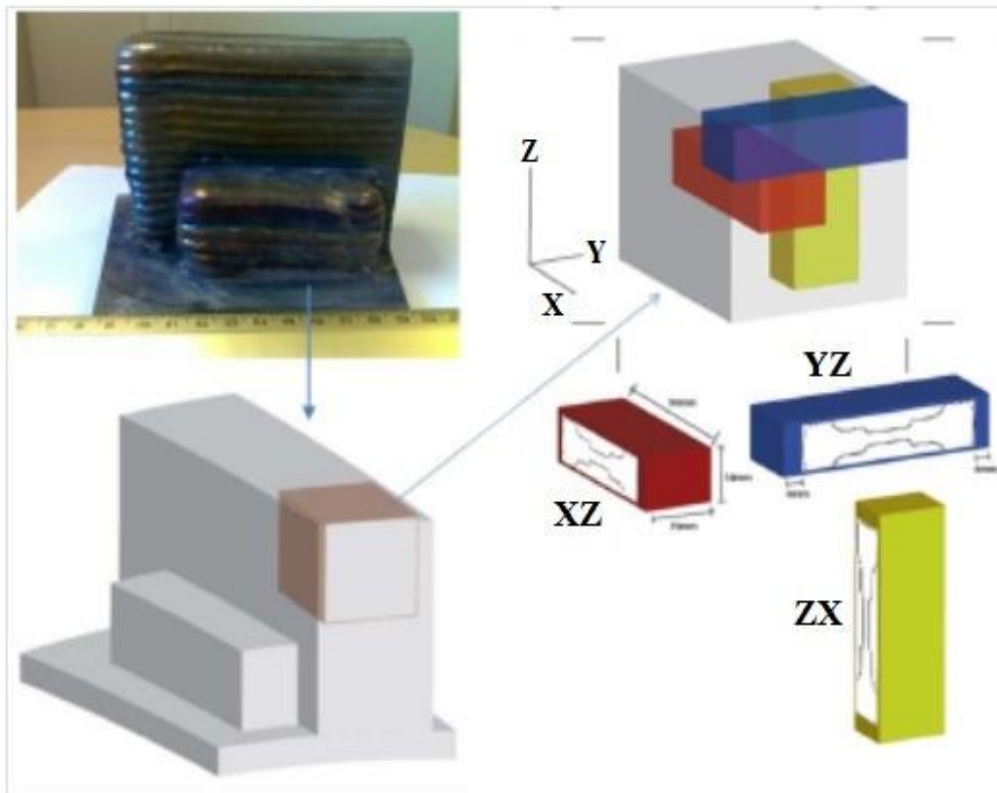
3.2.1 Cutting

Figure 14: The sequence of steps for extraction of tensile test samples.

To study directional effects and preserve absolute orientation, 3 blocks were cut from the sample and marked in the manner schematically shown in Figure 14. Figure 14 also shows the how the different planes for in-situ analysis are denoted. After some initial machining to face the block for clamping, cutting was done with a band saw.

Each of these blocks were then machined to the contours of the tensile specimen and sectioned into 1mm thick slices (Figure 15). This was done by electrical discharge machining to give precise dimensions, relatively neat surfaces low on deformation, and low material wastage. This technique, commonly referred to as spark erosion, utilises an electrode and current to perform cutting, instead of the direct contact of mechanical cutting. The electrode is positioned at a small distance (spark gap) above the workpiece. Both are submerged in a dielectric fluid. A pulsating dc power supply or EDM generator applies voltage pulses between the electrode and workpiece, generating sparks through the gap. Extreme heat is generated in the cutting zone. Each spark result in localised heating, melting the metal. At the end of the pulse duration the molten metal particles are flashed away by the dielectric fluid and remaining liquid material resolidifies [36].

The 15mm thickness of each block gave 10 samples. Allowing for removal of a sheet of about 0,5 mm from the band-sawed surfaces to eliminate deformed layer carrying internal stress which could potentially warp the outer specimens.
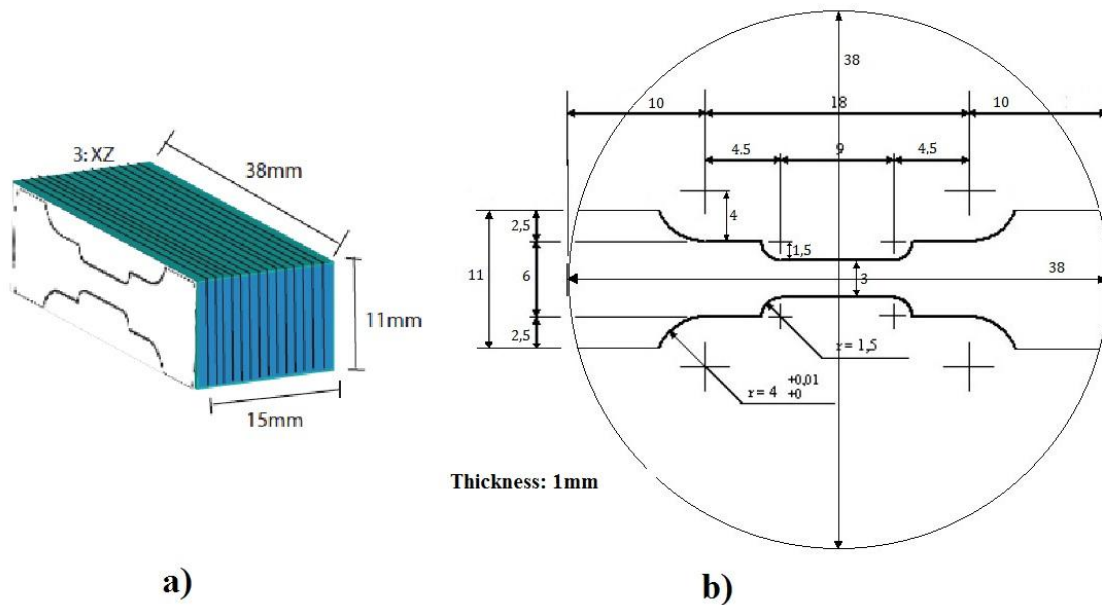
Figure 15: (a) Each block was segmented to produce 10 tensile specimens, (b) Geometry of each specimen presented.

3.2.2 Grinding and polishing

Grinding and polishing of the tensile specimens was done by hand. Two specimens where glued onto a Plexiglas plate with double sided sticky tape. By gluing the samples at each end of the plate one gets a stable platform that is easily handled. Below is a picture showing this method (Figure 16).
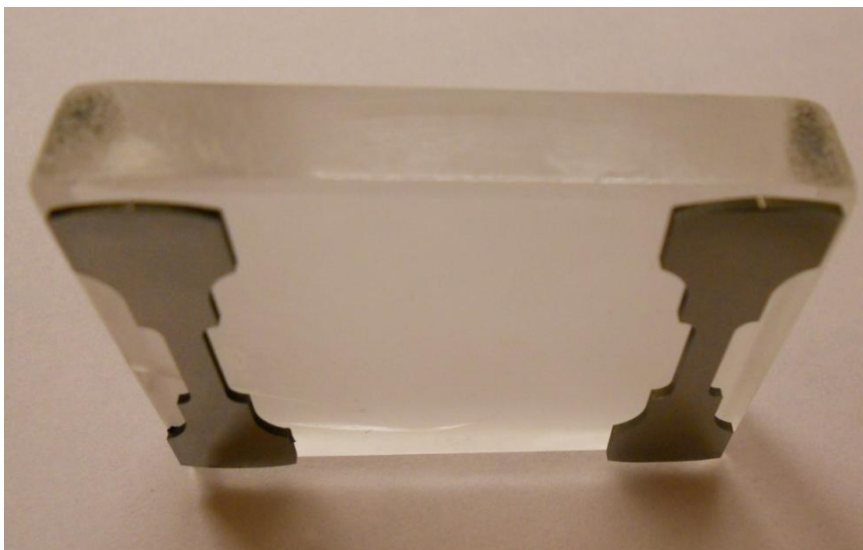
Figure 16: Tensile specimens mounted on a plexiglass plate for convenient handling during mechanical grinding and polishing.

The grinding and polishing procedure is the same as described in chapter3.1.2, although the force is approximate and applied by feel.

3.2.3 Cleaning
Described in chapter 3.1.4.

3.2.4 Ion sputtering
Described in chapter 3.1.53.1.5   Ion sputtering.

3.3   Macro- and micrographic examination
Macroscopic examinations were performed on a Wild Leitz M400 Photomacroscope.

Optical microscopic examinations were performed on a Leica MEF4M instrument.

High resolution (low step-size) EBSD scans were performed on Hitachi SU-6600 high vacuum FESEM. These are presented in Figure 24. Parameters are presented in Appendix C.

3.4   EBSD; combined stage and beam scan
A comprehensive list of parameters for the EBSD comboscans can be found in Appendix B.

Large area combined scans were performed in Zeiss Supra 55-VP low vacuum FESEM with online indexing.

Such scans where deemed necessary to get a representative overview of the morphology in the samples and to reveal the solidification structure. The SEM in question is equipped with a Nordif phosphorous screen EBSD detector coupled with a CCD camera and TSL OIM data collection software from EDAX. Typical areas scanned were in the region of $30mm^2$, with step-sizes ranging from 5 to 10 μm. The resulting scan times ranged from 4 to 8 hours.

To combat deviations because of low magnifications and electron beam displacement, calibration and adjustment of the beam was done at 35X on a Ni test sample.

3.5 Tensile test stage for SEM; mounting and vacuum pumping

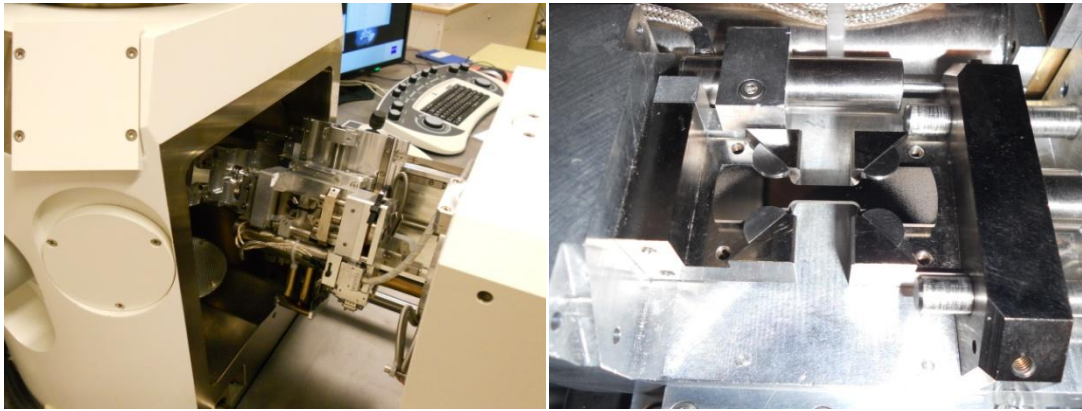Below are pictures of the tensile test setup which mounts to the SEM specimen stage (Figure 17).

Figure 17: Tensile test apparatus mounts to SEM sample stage, is tilted 70° and inserted into the SEM vacuum chamber.

This set up consists of a movable ramp driven by an electrical motor.

Information on apparatus specifications, monitoring software and mounting can be found in [37].

To achieve sufficient vacuum, the SEM was left pumping over night after insertion of the tensile stage assembly, a minimum of around 6 hours. In-situ analysis was done at a maximum pressure of 2×10^{-4} Pa in the SEM chamber.

3.6 In-situ tensile tests

Several tensile tests were performed. Parameters and settings are presented below.

3.6.1 Straining sequence

The samples were tested in uniaxial tension at a strain rate of 1 μ/s.

In-situ analysis was done by straining the samples in increments of 0,5%, 1% or 1,5% elongation. Stress-strain curves will be presented along with other results in chapter 4.2. One or two EBSD scans were performed at each strain level, covering different area or at different magnification within the same area. As will be presented and discussed briefly later (chapter 5.3.3), the strain measurements from this tensile apparatus are overstated because of some tightening effects in the early stages of force application. Real strain values are lower by about 1,5% (estimate based on typical elastic region compared to attained strain curves which are 'delayed' by some elasticity in the mechanism and clamping). Typically the sequence of elongation was 0%-1,5%-2%-2,5%-3%-3,5%-4%-5%.

3.6.2 Scanning parameters

For complete presentation of parameters, consult Appendix C.

These tests were done in Zeiss Ultra 55 LE FESEM, fitted with a Nordif phosphorous screen EBSD detector coupled with a CCD camera. Diffraction patterns were collected in Nordif data collection software to be indexed later, offline.

Scanning during in situ analysis was done at a magnification in the region of 200X-300X. This allows scanning of areas of around 400μm X 250μm. The resolution (step size) was set at between 0,2-0,5μm. The reasoning behind selecting these dimension is the desire to capture colony-wide strain effects, while still being able to resolve slip bands.

3.6.3 Post-processing of results

Indexing of the results for both offline and online scans were done in TSL OIM data collection software from EDAX. A classic Hough-transform was employed. Parameters for this operation are given in Appendix C.

The indexed data sets were post-processed in the TSL OIM analysis software, to produce various grain maps and graphic representations, as presented in the next chapter.

4 Results

In the first section, some preliminary microstructural characterisation will be presented. This analysis was performed to gain an overview of the dominating microstructural features, and to aid selection of locations for tensile sample extraction.

Images and figures will be referred to in the discussion that follows. Selected results will also be refined/processed to highlight important aspects during the discussion.

Global orientation axes will be presented along with the results where this is important. Refer to Figure 14 for definition of these directions.

4.1 Microstructural characterisation

Presentation begins with the macro-scale images that have been captured, before presentation of higher magnification images which reveal the intricate morphology of the structure under study.

4.1.1 Optical macrography and EBSD comboscan

Figure 18 shows how the macrostructure, or solidification structure, is revealed by studying the etched sample in an optical macroscope at low magnification.
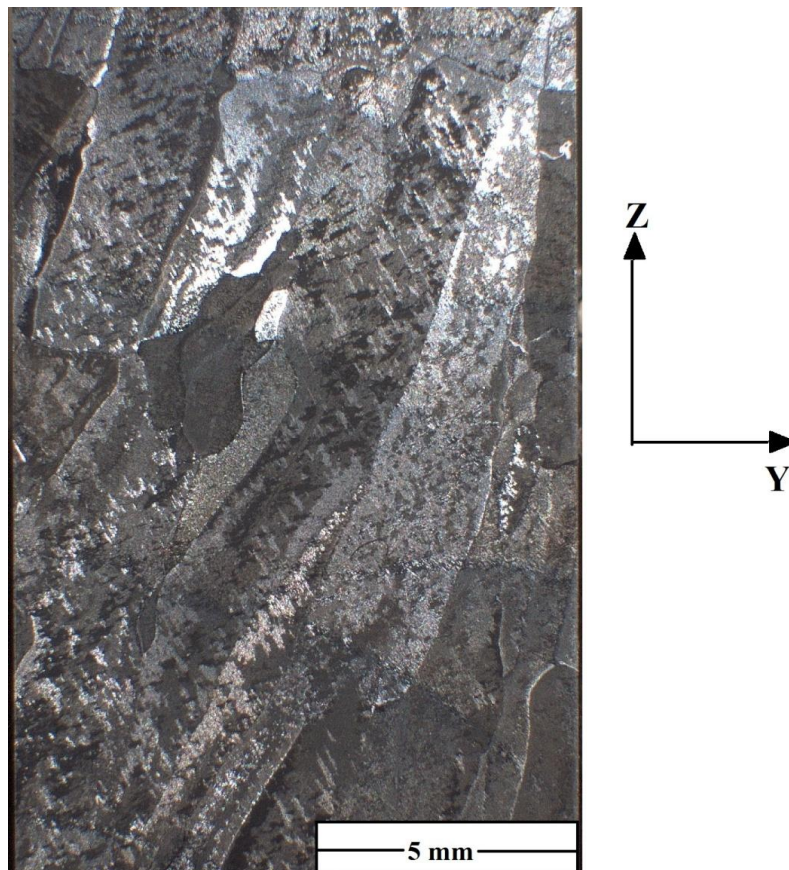
Figure 18: Macrograph of etched sample. Optical macroscope.

Combined EBSD beam and stage scan is able to reveal morphology at a similar scale, while also delivering orientation and phase data. Figure 19 presents such a large are scan. The presentation form (colours/filters etc.) is explained in figure texts. Other representations of this scan, i.e. illustrating phase content is placed in Appendix F.
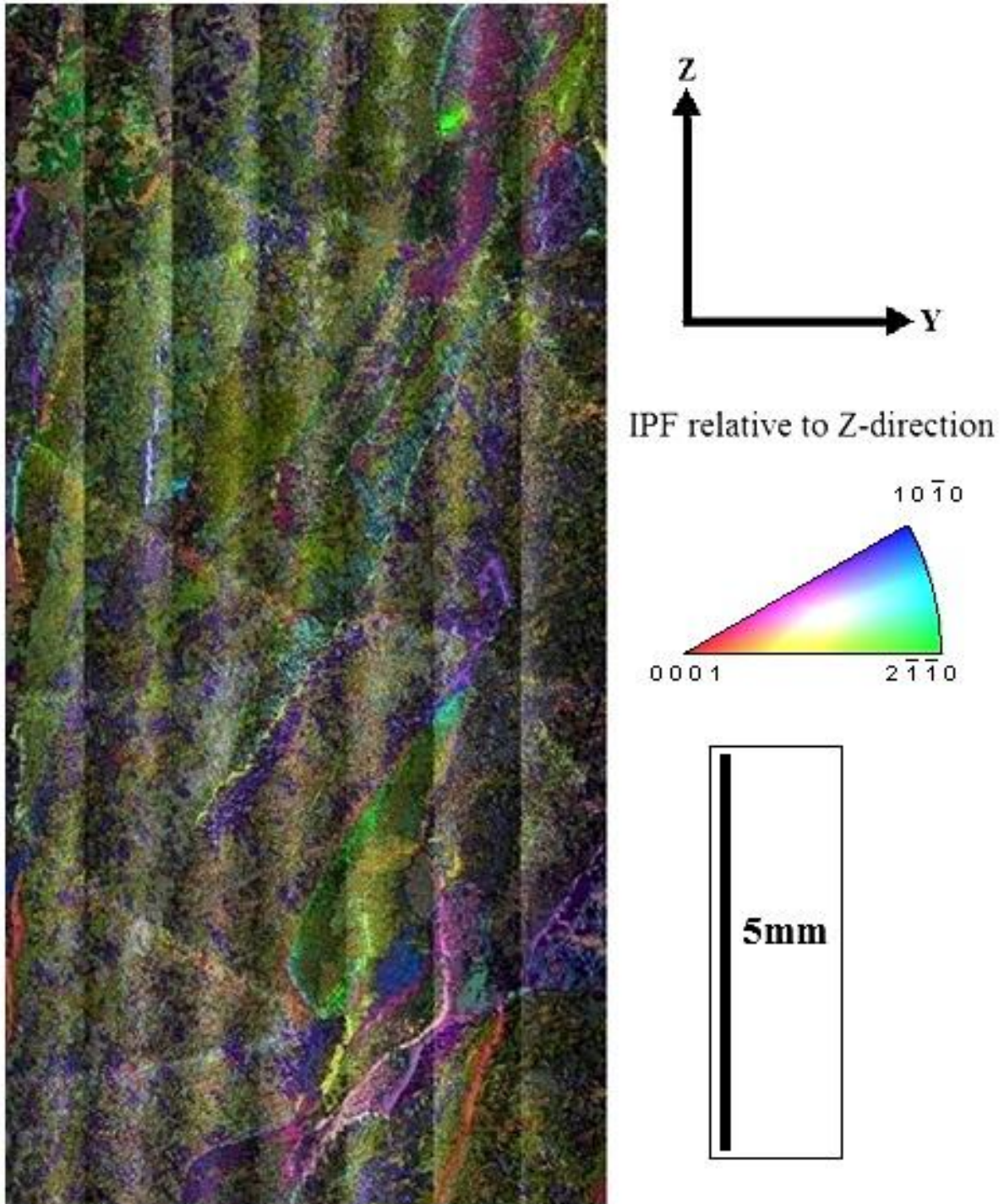
Figure 19: Combined scan over large area. Presented in composite form with colours according to IPF middle-right, overlaid with greyscale IQ-filter.

The software utilised as the analysis tool (TSL OIM analysis) allows for the calculation of texture intensity plots, such as presented in Figure 20. Reference is made to [5] for introduction and discussion of various forms of texture representation.
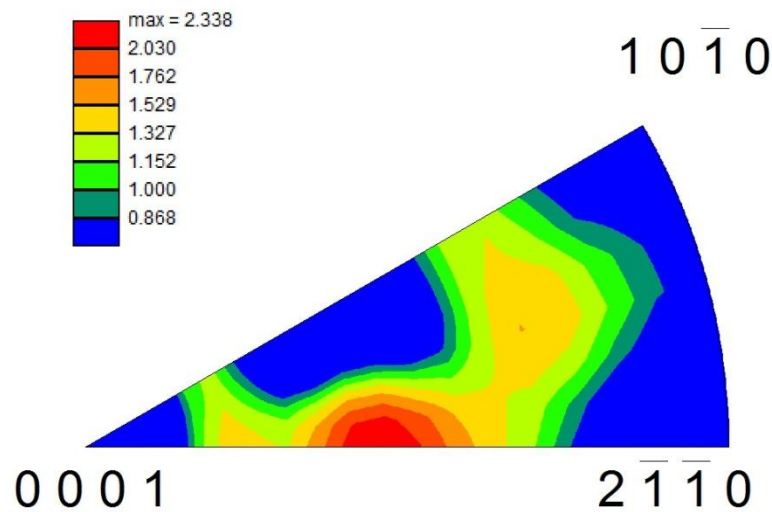
Figure 20: Texture plot for region in Figure 19. In reference to Z-direction.

The strength of the texture is indicated by the numbers assigned to the different colours along the gradient. The values refer to the parameter "n times random", giving the ratio of number of points with a certain orientation to the occurrence of such point in a random distribution of orientations.

4.1.2 Optical micrographs, SE and EBSD analysis

At low magnifications in the optical microscope, the segmentation into column grains is apparent (Figure 21).
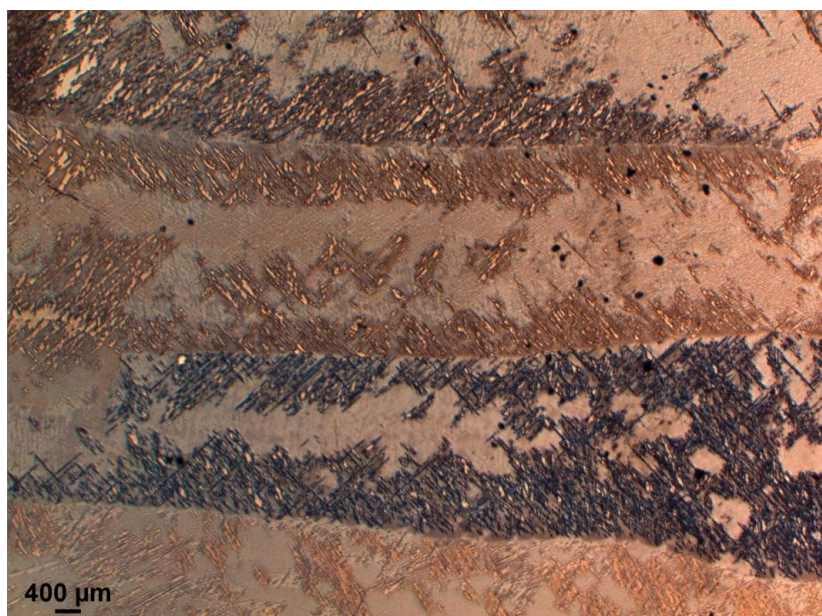
Figure 21: Columnar previous β-grains. Optical microscope.

Within each column grain are structures of finer plate colonies incorporated into coarser plate structures. This is shown in Figure 22.
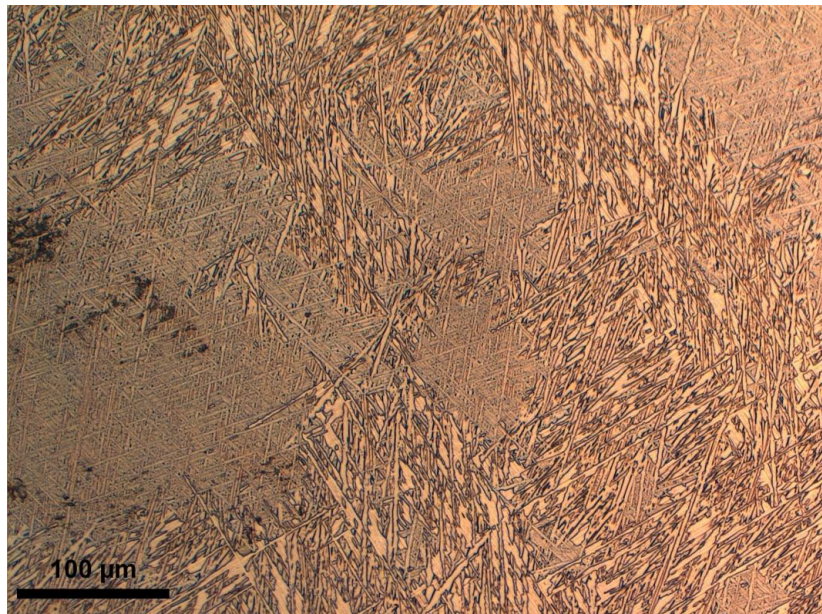
Figure 22: Micrograph showing different morphologies in colony structures. Optical microscope.

Study of the etched sample by SE-signal in SEM allows for collection of high-resolution images at higher magnifications. Figure 23 shows the high aspect-ratio grains observed at some colony boundaries.
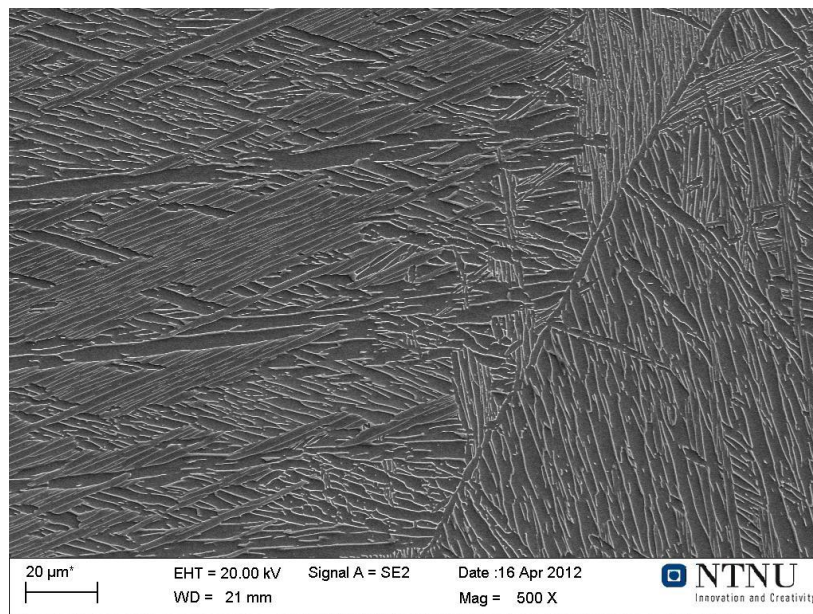
Figure 23: Colony structure imaged by SE.

Two regions which were deemed very illustrative of the microstructure were scanned with a very fine step-size relative to total area (parameters in Appendix C). These are presented in Figure 24. This was done on the Hitachi SU-6600 high vacuum FESEM which is capable of

delivering high beam current well in excess of 100 nA and allows collection of diffraction patterns at high rates (700 pps applied in this case).
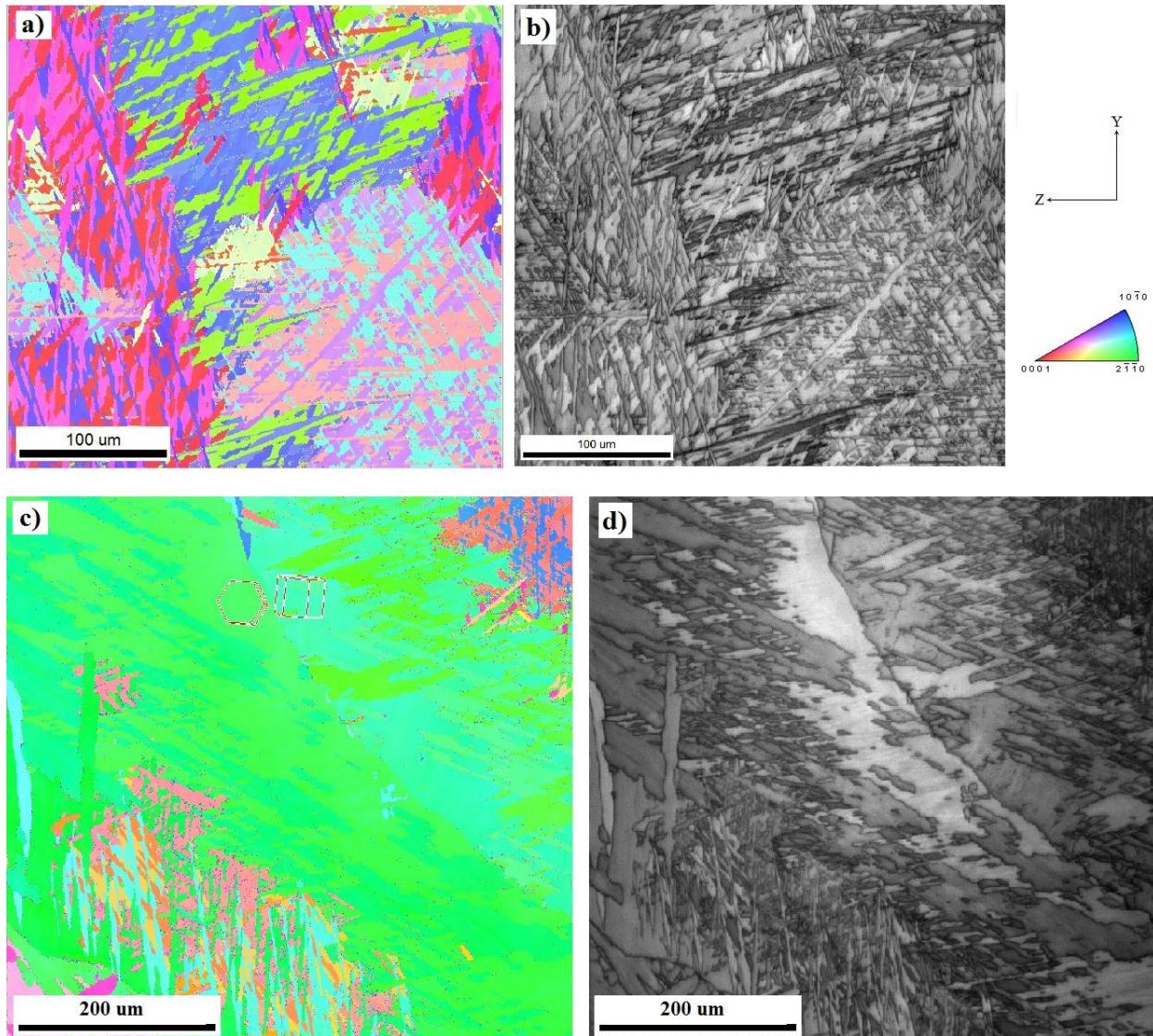
Figure 24: EBSD maps from two illustrative regions of the sample. For IPF maps the colour code given on the right hand side, reference direction is the horizontal Z-direction (see Figure 14 for definition of global axes. a) and b): IPF map and IQ map from colony-type morphology. c) and d): IPF- and IQ map from grain boundary α-type morphology.

4.2   In-situ tensile tests

The stress-strain curves for the 3 in-situ tests presented below can be found in Figure 37. Three of the in-situ tests will be presented in the following. Additional results are attached in Appendix F. EBSD comboscans were performed prior to- and after in-situ tensile testing. This was done to have a basis for determination of area to be analysed during in-situ tests. Comboscans after testing reveals any pronounced strain effects along the entire length of the deformed area. See Figure 14 for definition of planes and global orientation. The first index in the denomination lies along the direction of applied tension. I.e. plane ZX is stressed

along Z-direction. All IPF maps use the direction of applied tension as reference, i.e. they illustrate the crystallographic direction which is aligned with the stress axis.

After the large area scans, higher magnification scans performed at strain intervals during in-situ testing will be presented. In addition, sections of the analysed areas are presented in various forms to highlight certain features.

4.2.1 Plane ZX
Comboscans before/after strain

Figure 25: Combined EBSD maps of type IPF and IQ. Colour code for IPF map and global orientation given top right. a) Before In-situ straining, B) After in-situ straining.

In-situ scans at strain intervals

Figure 26: In-situ scans at strain intervals for area in plane ZX. Left to right: IPF map (see Figure 25 for colour code and reference direction), IQ map, SE image, stress-strain curve. Scale bar= 100 μm. Strain measurements: 1,5%-2%-2,5%-3%-4%-5%. Max stress: 846 MPa. Stress-strain curve is given in Figure 37.

In Figure 27 is an Isolated region from in-situ analysis on plane ZX (full sequence presented in Appendix F, sample ZX3). This is presented to highlight the behaviour of β-Ti during deformation. Figure 28 illustrates segmented behaviour and local texture plots from the same sample
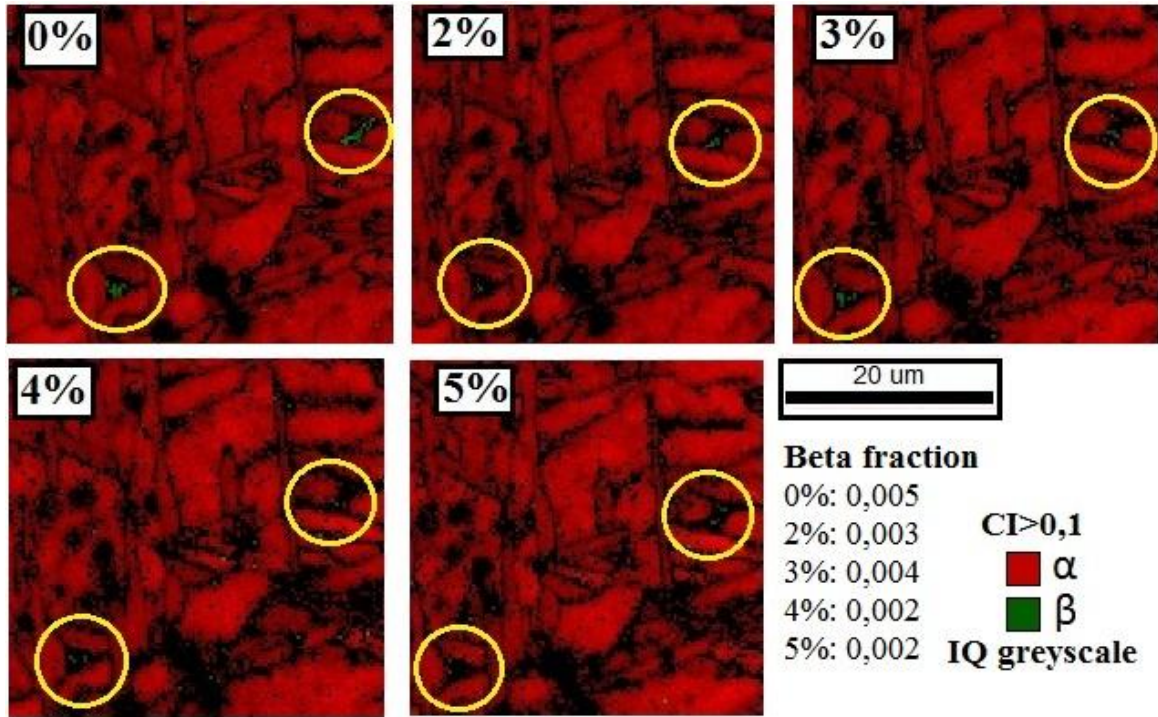
Figure 27: Observation of small β-regions during tension testing. Points with CI lower than 0,1 are excluded(black).
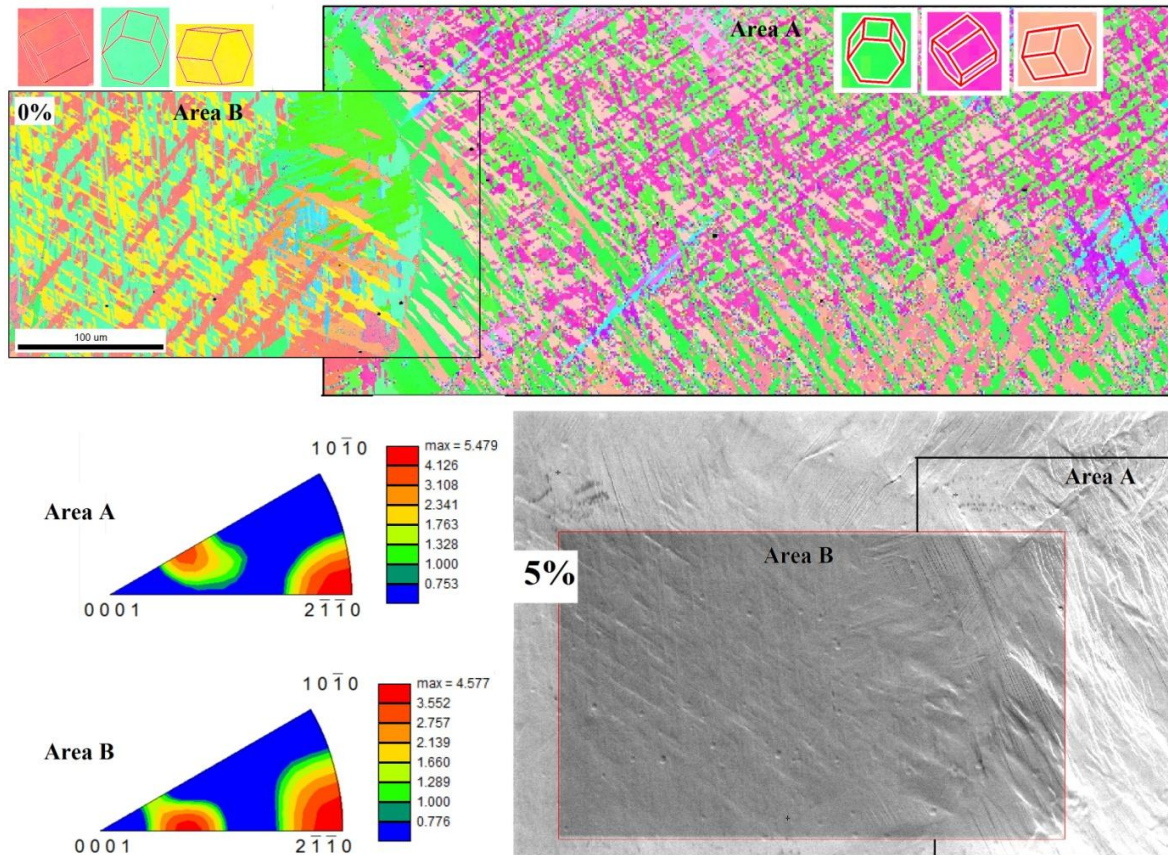
Figure 28: Neighbouring areas A and B were scanned prior to straining. Area B was analysed during in-situ testing (complete sequence in Appendix F, sample ZX3). Below IPF maps are texture calculations for the two areas, aswell as SE image obtained at 5% elongation.

4.2.2 Plane XZ
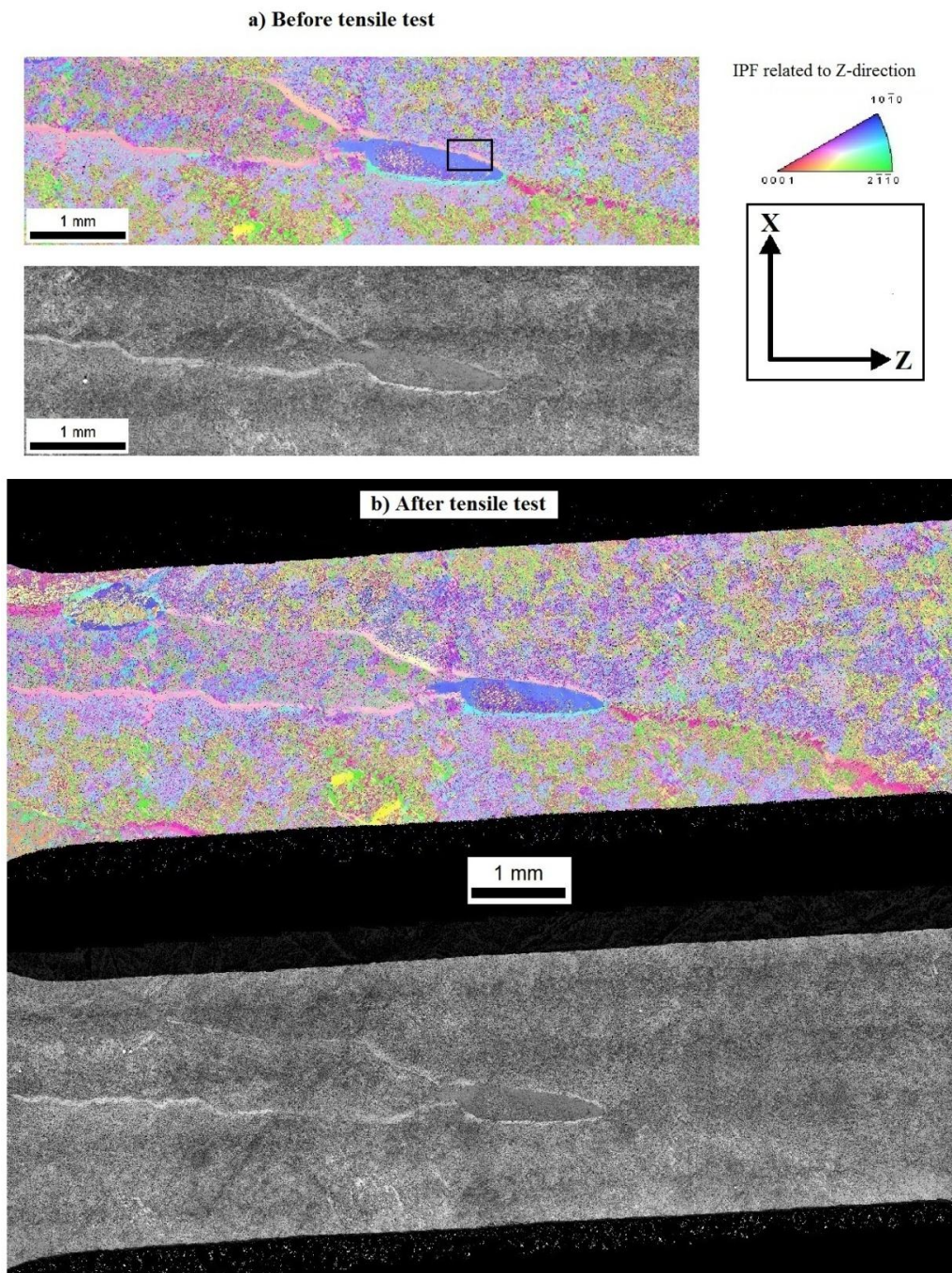
Comboscans before/after strain
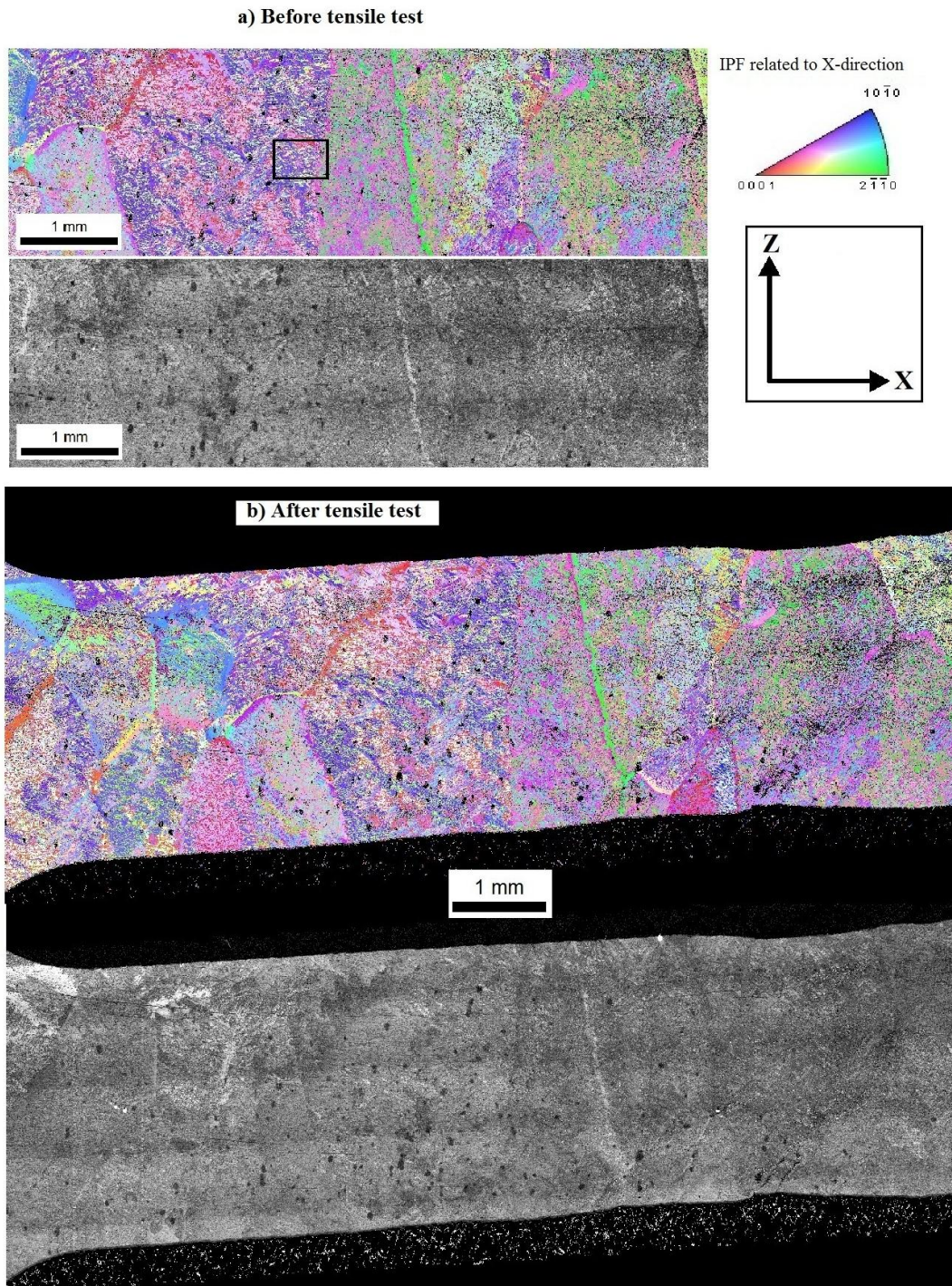
Figure 29: Combined EBSD maps of type IPF and IQ. Colour code for IPF map and global orientation given top right. a) Before In-situ straining, B) After in-situ straining.

At 5% elongation a crack was observed at a free surface of this sample. This is documented below in Figure 30 along with the surface of the entire specimen after tensile testing.
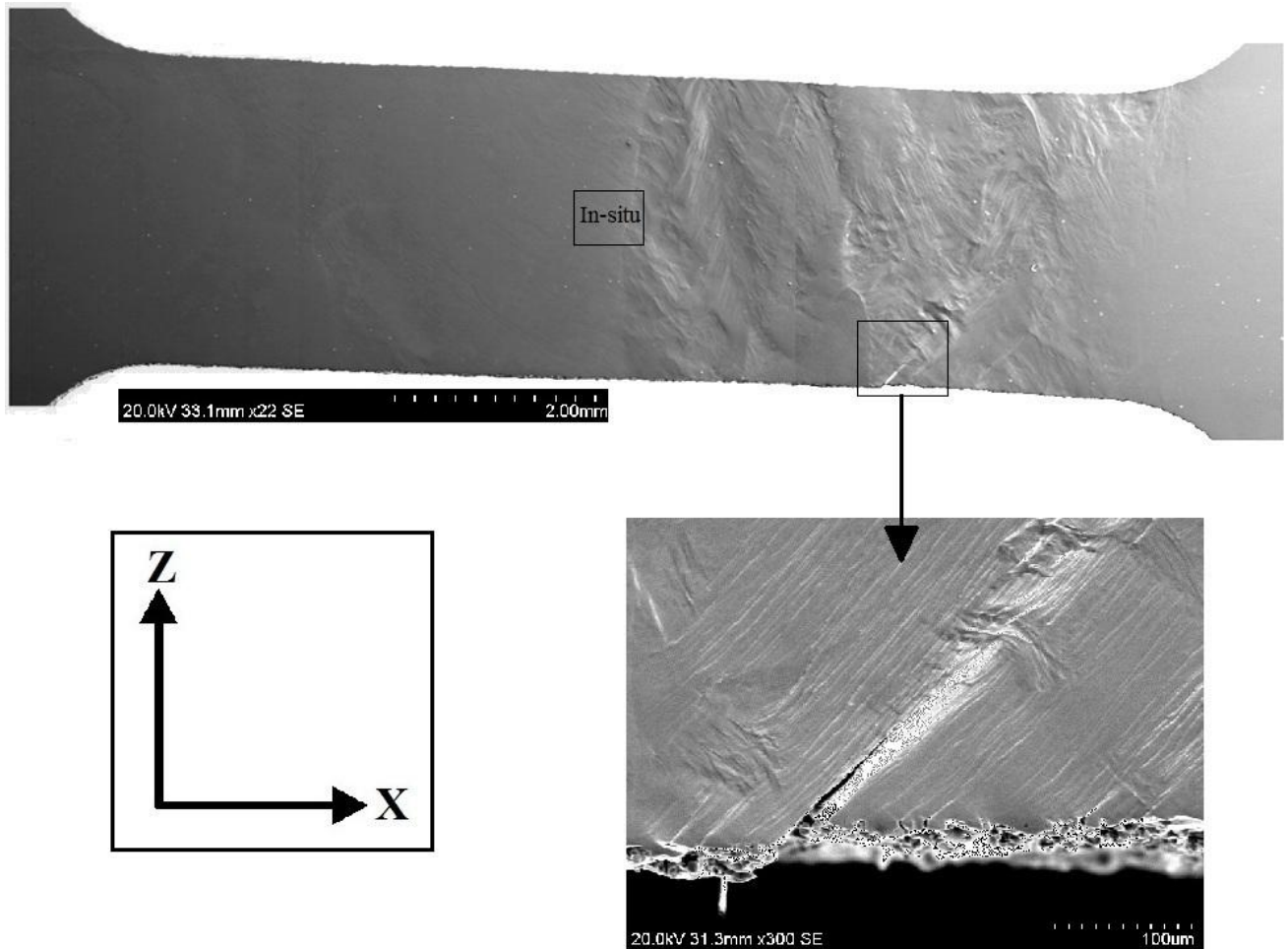
Figure 30: Surface topology and crack initiation in tensile specimen. Above: SE images stitched together to cover the length of the specimen. The placement of the in-situ scans (presented in the next section) is indicated. Below: Higher magnification image of crack.
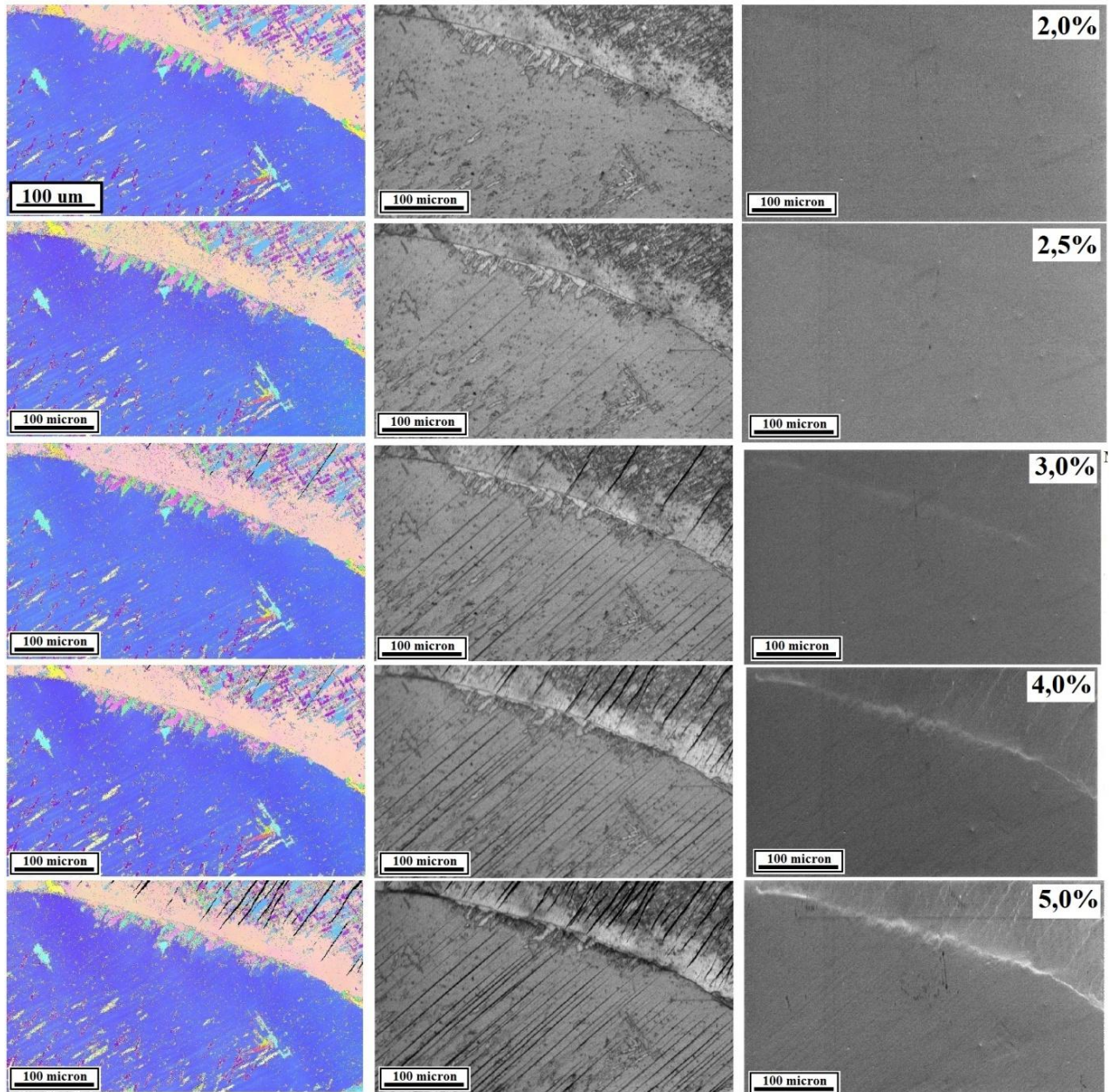
In-situ scans at strain intervals
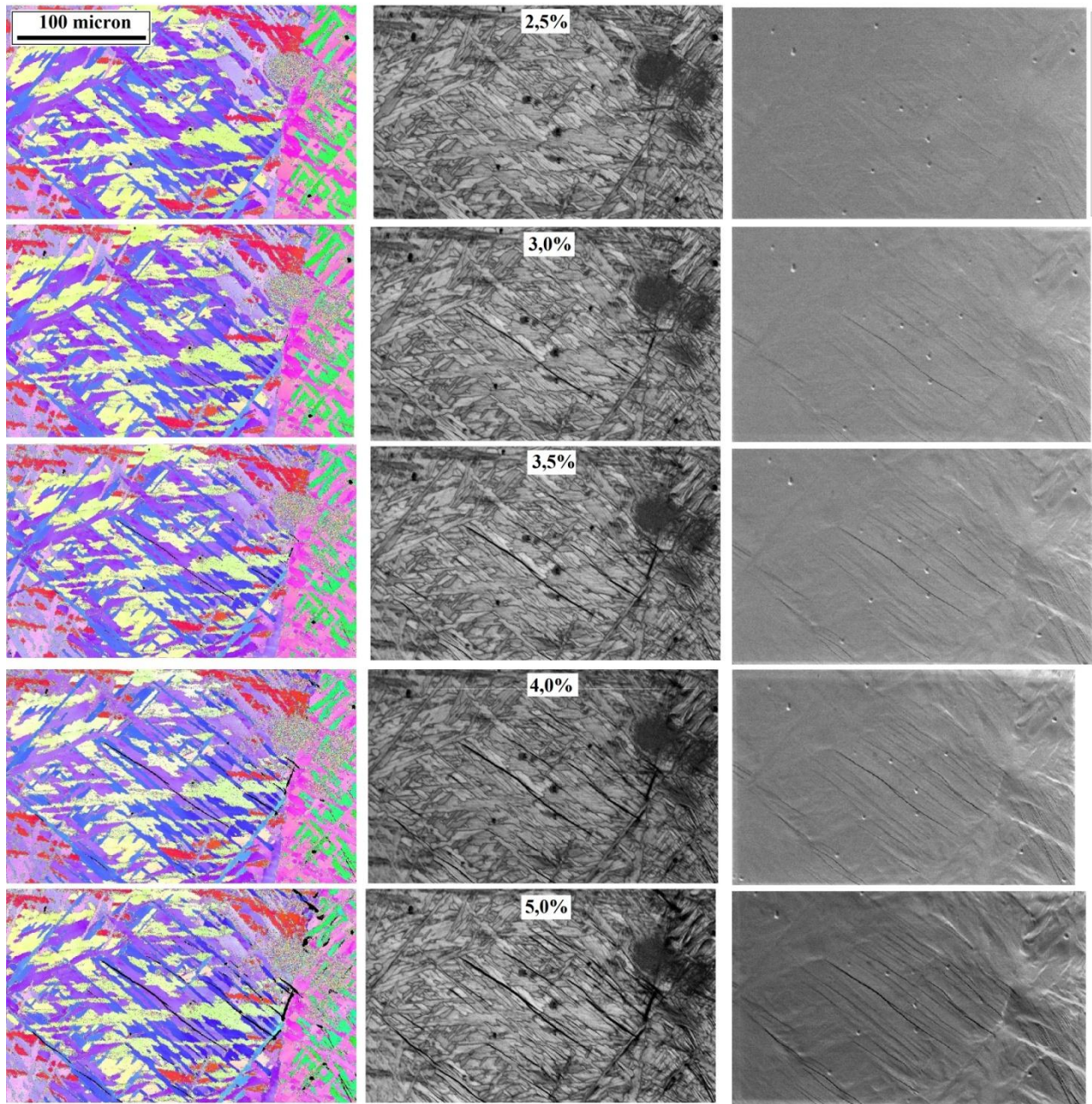
Figure 31: In-situ scans at strain intervals for area in plane XZ. Left to right: IPF map (see Figure 29 for colour code and reference direction), IQ map, SE image, stress-strain curve. Scale bar= 100 μm. Stress-strain curve is given in Figure 37.

4.2.3 Plane YZ

To make this section more compact, in-situ scans from this plane are included in Appendix F.
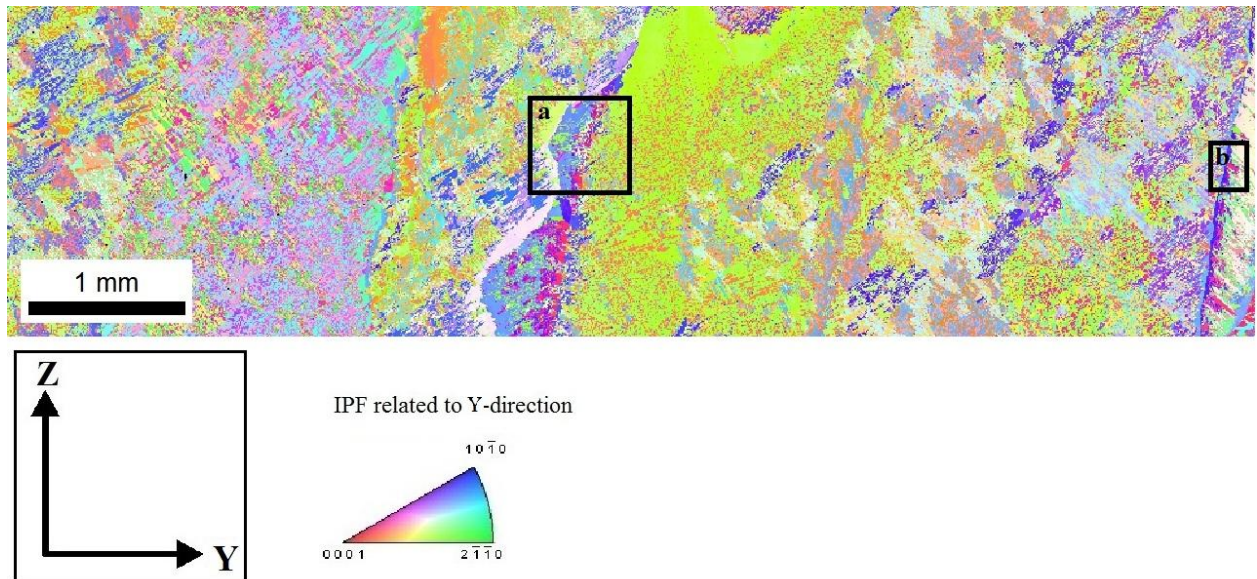
Figure 32: Comboscan performed prior to tensile test. Area (a) indicates position for in-situ scans (see appendix), area (b) shows position for image in Figure 35 and Figure 36.
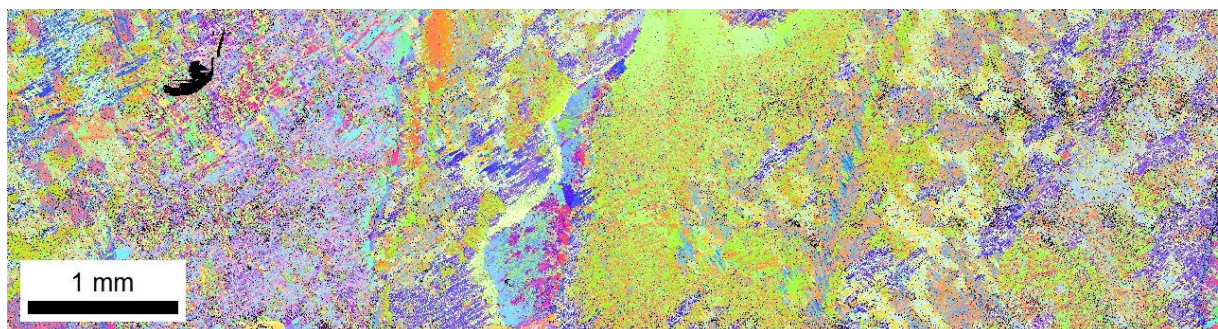
Figure 33: Comboscan after tensile testing. (Dark area towards top left is contamination/artefact and should be disregarded)

The surface appearance of slip bands were capture by SE imaging after strain in Figure 34.

| 2 µm* | EHT = 20.00 kV | Signal A = SE2 | Date :16 Apr 2012 | NTNU |
| | WD = 24 mm | | Mag = 4.44 K X | Innovation and Creativity |
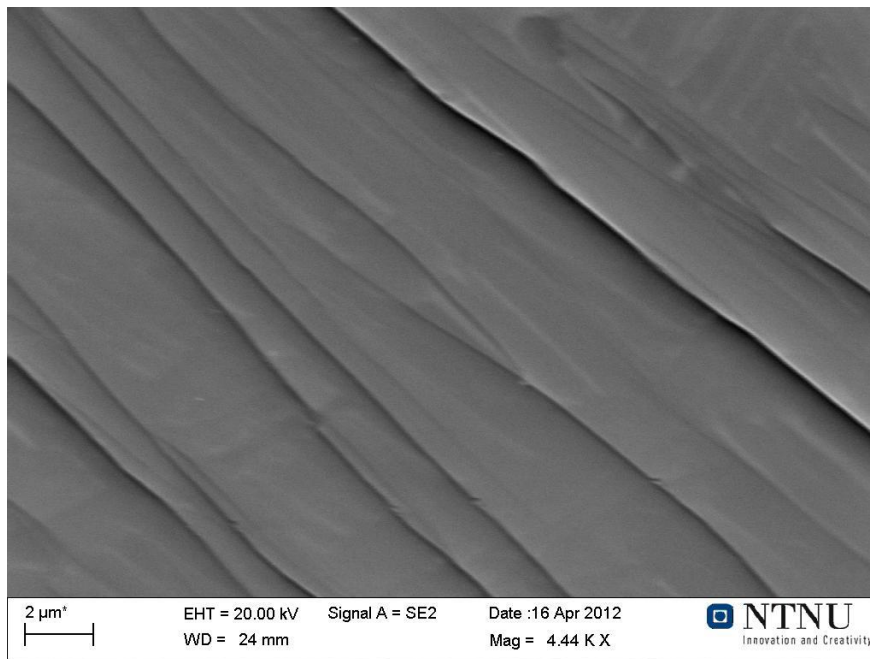
Figure 34: Appearance of slip bands at high magnification. SE-image.

The appearance of the surface along a previous β-grain boundary after 5% elongation is imaged by optical microscope in Figure 35 and Figure 36.

400 µm
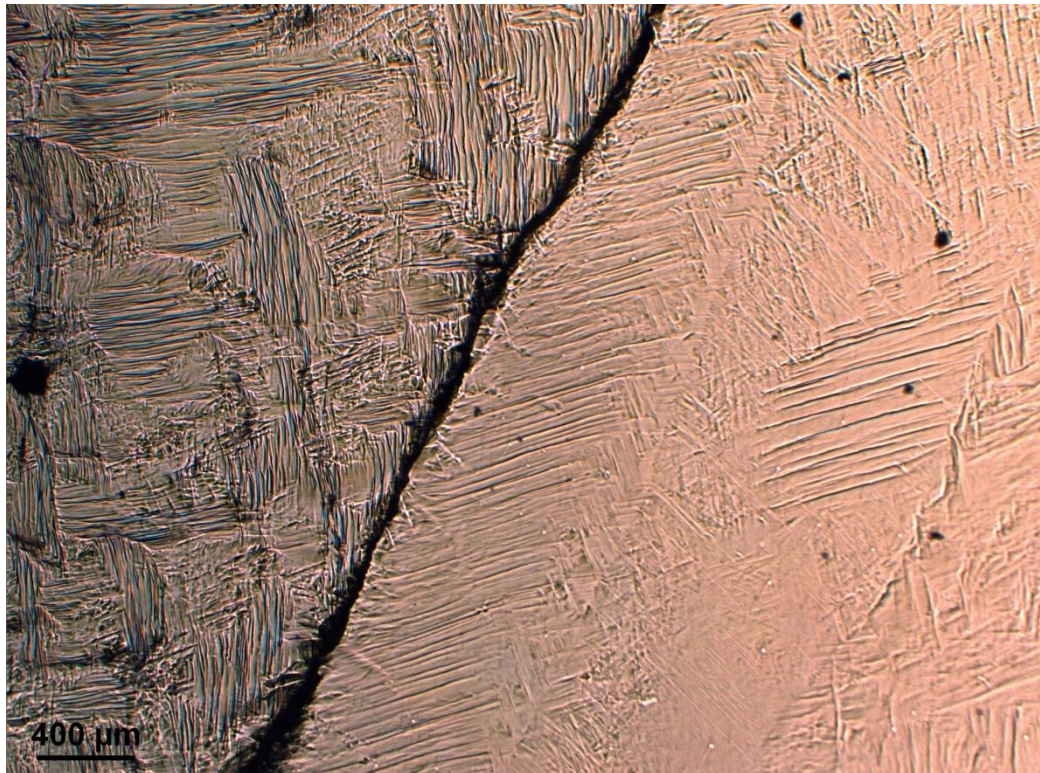
Figure 35: Segmentation in surface appearance after tensile testing. Optical microscope.
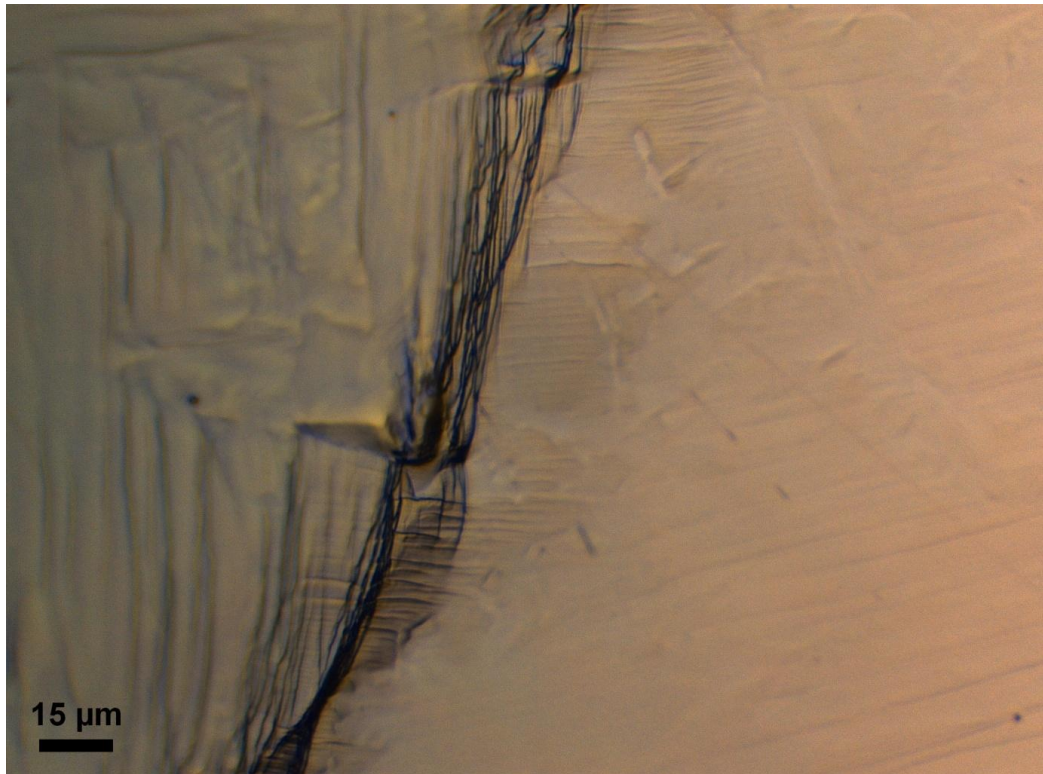
Figure 36: Ledges and steps on the surface between segments after tensile testing. Optical microscope.

4.2.4 Stress-strain curves

The validity of these curves is discussed further in chapter 5.3.3.
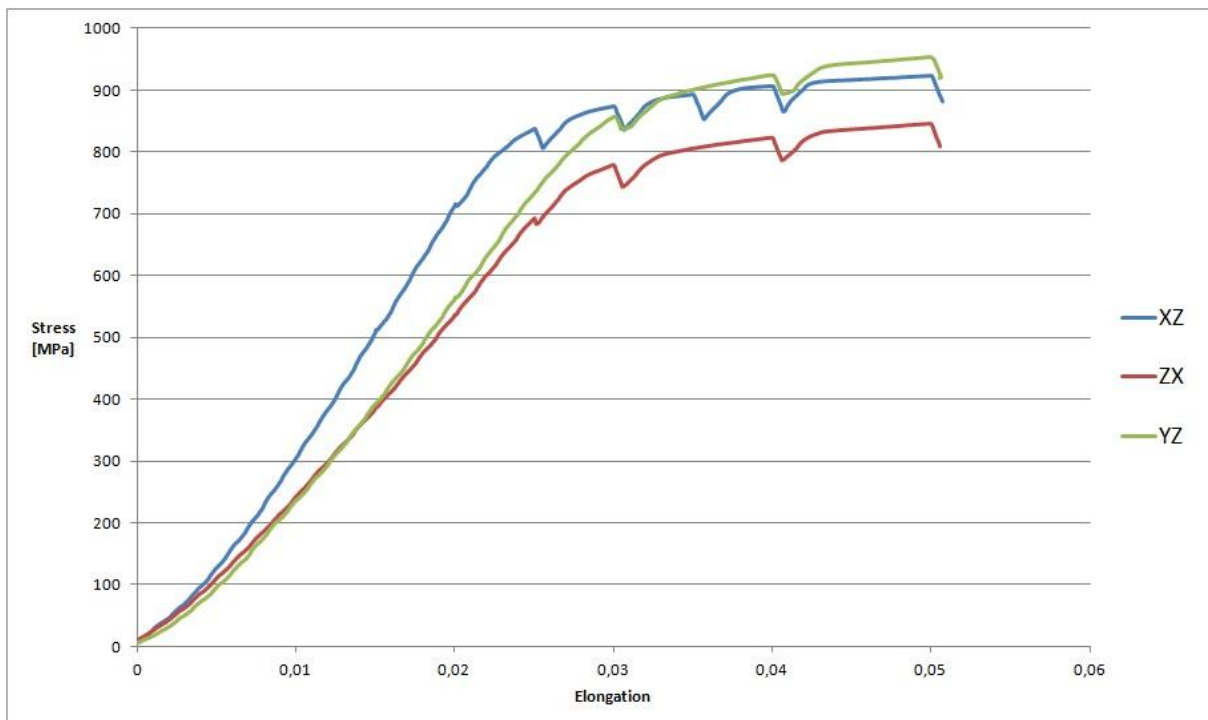
Figure 37: Stress-Strain curves for the 3 in-situ tests presented in the previous sections. The dips in the curves is caused by relaxation in the material as loading is halted.

5 Discussion

5.1 Characterisation of structure

Building parts by a three-dimensional array of welds produces a complex microstructure. The characteristics of the microstructure was generally found to be fairly inhomogeneous, with a segmented appearance even at the macro level. In the following sections the observed structure will be compared with similar reports from elsewhere and rationalised on the basis of known mechanisms that are suspected to be at work during the ALM process.

5.1.1 Macro level

Looking at Figure 18, columnar grains are a very prominent feature, with their long axis at a slight angle to the building direction, Z. This has been established as a common occurrence in most ALM processes, including laser melting and powder based methods, examples in [38, 39].

A similar region to Figure 18 analysed by EBSD is presented in Figure 19. A more or less continuous grain-boundary α-layer outline the columnar solidification structure. Using the EBSD comboscan technique one is not able to resolve the finer intricacies of the microstructure, the step size in this case was 10μm. A smaller step size would involve unfeasibly long scanning time with online pattern acquisition and indexing rate of around 40 PPS. Lighter bands are apparent across the image (the curved horizontal bands). These indicate a higher IQ-value. The dimensions and shape of the area outlined by the bands are reminiscent of the welds this sample is comprised of. Such bands are commonly observed in ALM processes, and are attributed to a certain sequence of heat treatment generated by the sequential application of layers. This is assumed to involve prolonged exposure to temperatures in the $\alpha+\beta$ region, around 800°C (ref. phase diagram in Figure 5) [39]. This has a strong grain coarsening effect. The quality of the diffraction pattern obtained at a point is generally degraded by the presence of grain boundaries in the proximity. This explains higher IQ values along these bands. It is this concluded that the bands are not a direct outline of the solidified welds, but an effect in the HAZ which mirrors the periodicity of weld deposition with their resemblance in shape and size.

The texture plot in Figure 20 reveals a fairly weak texture (2,3 times random). The highest intensity is indicated for an orientation where basal planes are inclined by 45° to the Z-direction. This texture is weaker but more uniform than the 2-component texture which was found in grade 2 Ti produced in the same manner [5].

The structure is composed almost entirely of α-phase, with β content indicated as low as 1% in most regions. The issue of phase composition, detection of phases and possible artefacts will be discussed in section 5.3.

5.1.2 Micro level

Figure 21 reveals what a strong bearing the columnar previous β-grains has on the morphology of the structure, and how the growth of the finer microstructure is dictated and constrained by these formations. As mentioned, grain boundary α forms spontaneously at the perimeter of previous β-grains. This is evident in Figure 24 (c) and (d). A breakup of the blocky grain boundary morphology into high aspect-ratio needles or plates towards the β-grain interior is also apparent. Figure 24 (a) and (b) show a typical colony type microstructure found within the prior β-grains. The colours in Figure 24 (a) and (c) indicate the crystallographic orientation with reference to the horizontal direction in the image plane. A clear relationship is found between plates within a colony, and also seemingly across previous β-grain boundaries. As indicated by the unit cells placed each side of the boundary in Figure 24, although both grains have the same crystallographic axis aligned with reference direction Z, their absolute orientation differs by a rotation of 90° about this basal direction. These geometric connections between grains are caused by the strict adherence to BOR (ref. Figure 2). Within the constraints of this geometric relationship, *variant selection* occurs. In Figure 38 boundaries with misorientations 90° +/- 5° and 60° +/- 5° are marked in an attempt to show the prevailing grain boundary types.
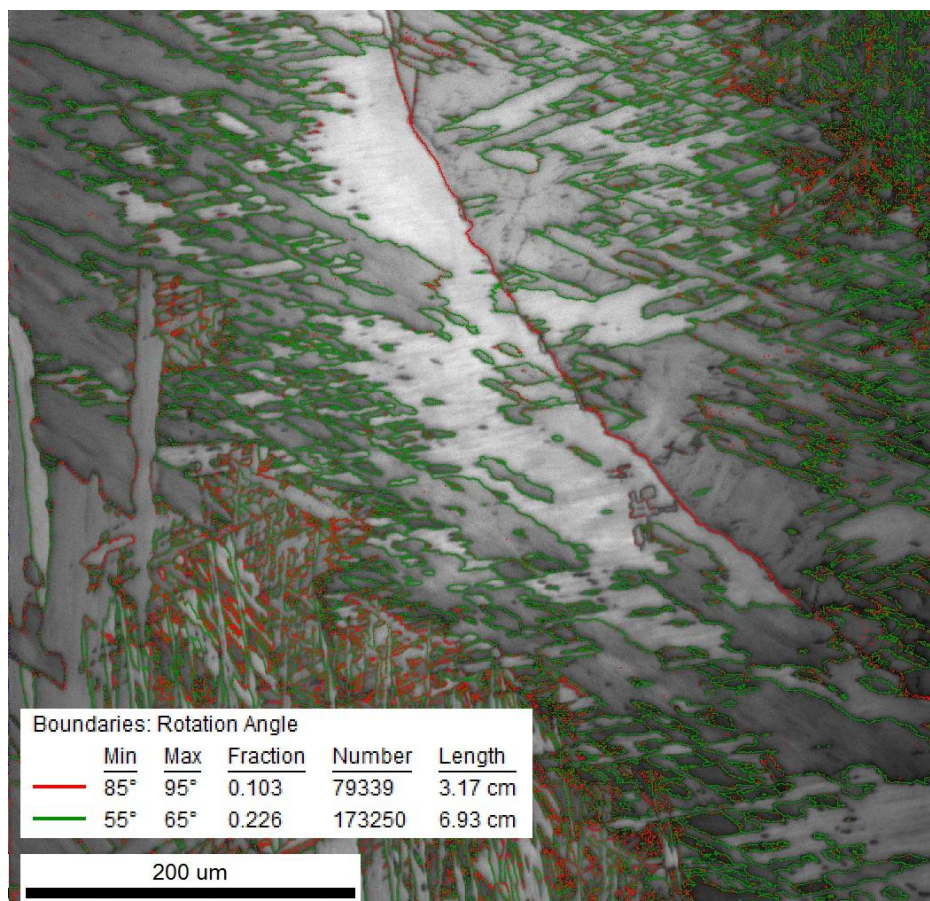
Figure 38: Misorientations between grains are indicated.

It is clear from this map that misorientations of c-axis by 60°(green lines) and 90°(red lines) dominate the structure. This is found throughout all scans. Also in larger, more

representative regions. Figure 39 indicates how these misorientations appear as a result of BOR (chapter 2.1).
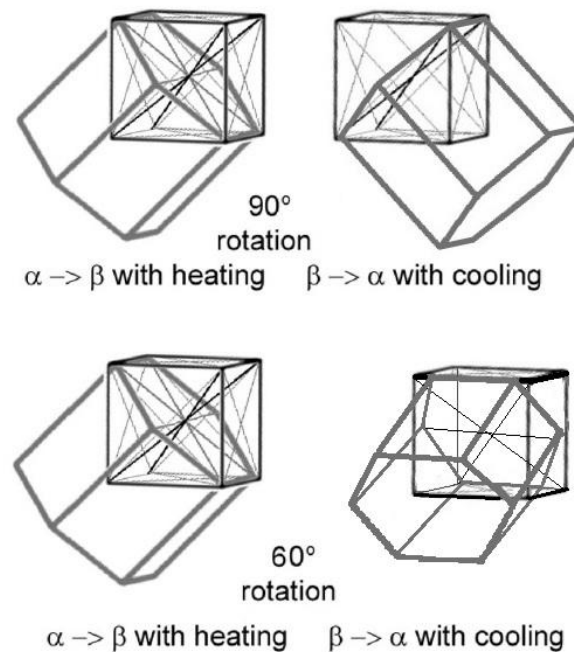
Figure 39: Allotropic transformation giving rise to 90 or 60 degree orientation difference (Adapted from [23]).

During the back-transformation to α, the number of variants means a 60° misorientation is more likely as the 90° rotation if variant selection is assumed to be random. Out of 6 {110}$_\beta$-planes, one gives zero rotation, one gives 90° rotation and four give 60° rotations. In purely colony-type areas these ratios seem to be upheld (for example in area in Figure 24 (a)), while at former β-grain boundaries, 90° rotations are more prevalent. This is most likely a result of the mutual alignment of grains each side of the β boundary. In [8] alignment of basal planes along the boundary plane of column grains in a Ti-8Al-XV alloy (V content was graded along the sample). In this study of Ti-6Al-4V, a clear preference for alignment of prismatic planes with the β-grain boundary was found. This is exemplified in Figure 24 (c) with unit cells placed each side of the boundary in the top region. The discrepancy could be caused by the higher Al content in the referenced study. As discussed in chapter 2.2.1, additions of Al change the relative densities of basal and prismatic planes, making basal planes denser and more active as slip planes at content above 6wt%. This effect could simultaneously influence the relative surface energies of the facets in the HCP cell. Low energy facets have a tendency to align themselves with the grain boundary plane [8]. The influence of interfaces along previous beta grains is important considering the columnar nature of these grains, and thus the far reaching implications of such ordered growth. As the IPF in Figure 20 suggests, it creates a certain macrotexture.

Further into the interior of prior β grains, a typical widmannstatten morphology is dominating (Figure 24a,b and Figure 23). The growth directions indicated in Figure 9 is observed to hold true in most cases, although it is often difficult to make assumptions about the angle between the plane of polish and the widmannstatten plates. An example is shown in Figure 40.

Crystal dir.

[-17 23 -6 0]

[15 -24 9 -1]

[28 11 -39 -3]
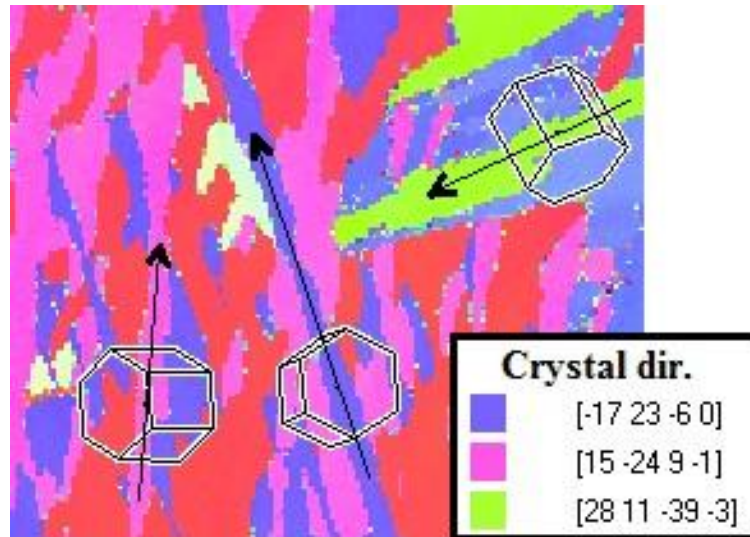
Figure 40: Growth direction of plates in colony structure. Crystal directions along indicated vectors are given.

It is clear that the tendency is for the long dimension of plates to lie along a direction in the basal plane, perpendicular to c-axis. This is indicated by the fact that the last vector component is zero/near zero for all vectors. As previously discussed, this growth configuration is favourable for effective solute shedding and heat transfer during growth. The structure also exhibits the tendency for plates belonging to different colonies to have their long dimensions perpendicular to each other, as would be expected after sympathetic nucleation. Sympathetic nucleation, meaning the formation of secondary colonies at the boundary of existing colonies, is favoured at higher undercooling. The extremely high aspect ratio of many grains, such as in Figure 24 (a) is partly caused by a mechanism observed in [17], whereby large β-grain sizes retard the transformation into α-phase towards a lower temperature. This causes lower diffusion rates, which will exacerbate the need for lateral diffusion over the shorter diffusion lengths. The result is extremely long and thin plates.

5.1.3   Relations to production process

Some suggestions are presented in chapter 7 regarding the possibility of achieving a more rigorous, quantitative description of microstructural development during the production process. In the following, some general, qualitative observations are presented.

Solidification dynamics

The strict directional solidification is evident. At least in the end result, as the remelting upon application of consecutive layers would remove any disordered solidification product which

sometimes is known to occur at the final stage of weld solidification, when temperature gradients are steepest (e.g. towards fusion line in conventional welds [10]) . This top layer would be rearranged in the next pass of the welding torch.

Column grains are the remnants of cellular solidification. They are generally oriented at a slight inclination to the Z-axis (ref. Figure 19 and Figure 18). This indicates that they grow along the steepest temperature gradients as the welding torch moves or as a neighbouring layer is being deposited.

In this earlier study of Grade 2 Titanium components produced in a similar manner, a suspected tendency for solute segregation was reported. The culprit in that case would be the contents of Fe, at 0,3 wt%. β-phase was found highly concentrated in a small region. No such tendency is observed in Ti-6Al-4V, although the description of phase content is fairly clouded by suspected detection problems and artefacts (This is discussed in chapter 5.3.1). Fe content is lower in Ti-6Al-4V, 0,16 compared to 0,3. The modest partition of both Al and V between solid and liquid phases (ref. phase diagrams in Figure 3 and Figure 4), combined with high diffusion rates give a lower segregation tendency.

Solid state transformations

According to [15], partly diffusionless phase transformation was observed down to a cooling rate of 20°C/s across the β-α-transus temperature (see Figure 8). No characteristic colonies of needle-like martensite was observed in any samples. Reheating of layers in this process could effectively give an aging treatment, and, if heated above the martensite transformation temperature of around 600°C, this structure would reform to a more energetically favourable morphology.

In [40] the transformation of metastable β-phase into martensite upon heating was observed. It was found that this transition depends on the dimension of β-inclusions. The fine structure transformed to martensite at 425 C°, the coarse structure at 575 C°. This mechanism is very likely present in certain segments during production.

In Ti grade 2, the solidification structure is not as apparent. It is obscured by uninhibited growth of α-grains in a similar ALM process [5]. The preservation of the cellular morphology in the Ti-6Al-4V samples is clear evidence of the previously discussed resistance to recrystallization in this alloy. As a segment is reheated, the previous β-grains reform by recombining after growth from retained β.

5.2 Strain response

By means of illustrative examples the deformation mechanisms both at micro- and macro level will be discussed. The inhomogeneous and segmented appearance of the microstructure means that the characteristic strain response varies significantly from region to region. First, examples of mechanisms at work at the microscopic level will be discussed as an aid to understand the observed macroscopic behaviour. Discussion culminates in a section devoted to the qualitative connection between production process and the particularities of the microstructural behavior.

5.2.1 Micro level

In [14], higher oxygen content(0,19wt% said to be sufficient) was correlated with non-homogeneity in dislocation glide. Specifically, ordering of oxygen(see 2.1Phase transformations in α/β-alloys) seemed to promote slip by first order pyramidal systems rather than the prismatic systems(Table 1). This was ascribed to the position of interstitial sites in the HCP cell relative to active slip planes. Oxygen would interact with and hinder slip on basal and prismatic planes to a larger extent than pyramidal planes.

Coarse slip bands on prismatic planes are promoted by Ti_3Al precipitation[14, 41].

Sample plane: ZX

The orientation of this plane and the placement of the tensile specimen is indicated in Figure 14. Figure 25 shows how this area places on the tensile specimen. Samples lying in this plane, along the Z-direction exhibit the columnar macrostructure along the entire length of the sample.

In Figure 41, the in-situ analyzed area is presented along with icons indicating the placement of unit cells (orientation of crystal lattice) within each grain (indicated by number and corresponding colours). These crystallographic orientations can then be correlated to the Schmid factor for each relevant slip system through Schmid factor contour plots in the IPFs (figures taken from [42]). Pyramidal refers to the first-order variant (see Table 1). The derivation of these contour plots is explained in [42].
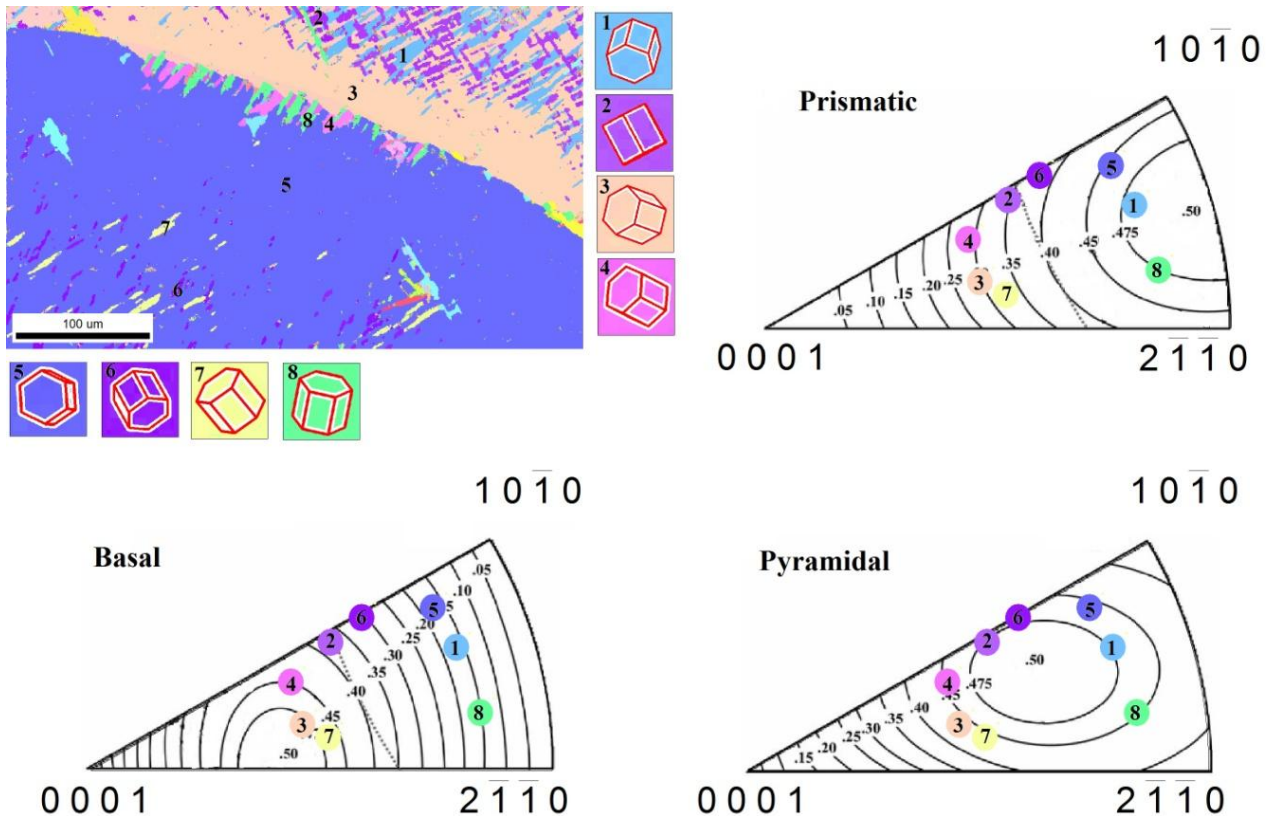
Figure 41: The IPF map of area subject to in-situ study is related to the Schmid factor for different slip systems through IPF contour plots. Sample plane: ZX. Contour plots as presented in [42] with grain orientations for area scanned in-situ overlaid.

Images from the sequence of straining are shown in Figure 26. The effects of deformation first becomes apparent at 2,5% elongation, where regularly spaced dark lines appear in the IQ image in grain 5, the large blue grain (ref. Figure 41). The dark lines are, as suggested earlier, a clear indication that plastic deformation has occurred in the grain. The lattice structure has dislodged and slipped along these deformation bands (or slip bands), which now contains a high density of dislocations. The lattice imperfections along slip bands weaken the diffraction signal relative to the background noise. While they are still indexable (ref. IPF map in Figure 26), the IQ parameter is significantly lowered.

Consulting the Schmid factor plots reveals that grain 5 is oriented just about equally favourable for prismatic and pyramidal slip systems, with a Schmid factor of around 0,46. Drawing from what was presented in the theory section, the general consensus after deformation tests on single crystal α-Ti is that prismatic planes require a significantly lower CRSS for activation. Deformation is thus expected to be accommodated on prismatic planes. At this stage no topology is visible on the surface (ref. SE image in Figure 26). This further confirms that prismatic planes are active, as prismatic slip would produce strictly in-plane deformation (noticing that the c-axis is perpendicular to the surface in grain 5).

At 3% elongation, coarser, more widely spaced slip bands are apparent. These seem to emanate from the grain boundary region between grain 5 and grain 3. Figure 42 presents a closer look at this boundary.

a)

b)

c)

d)
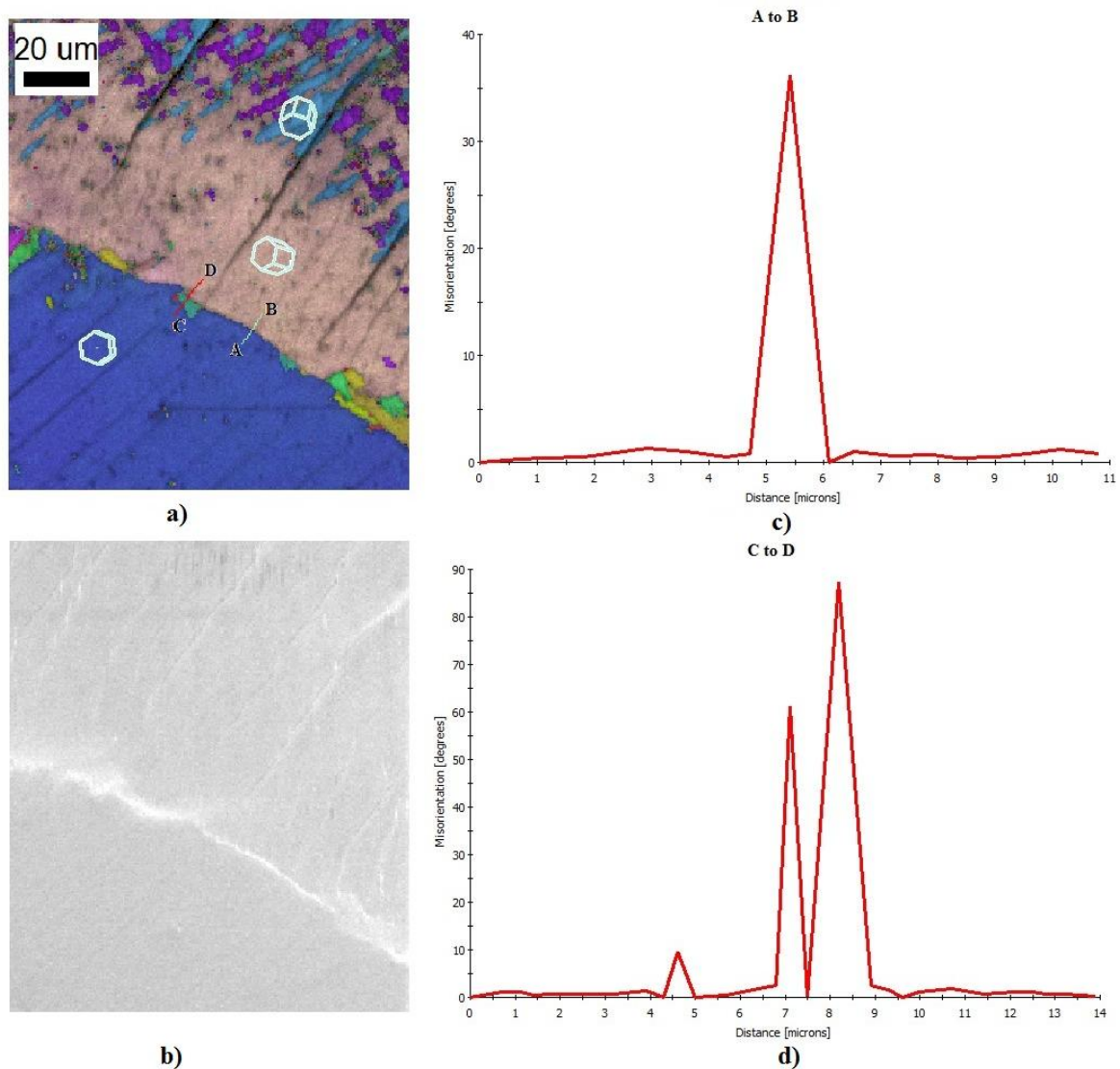
Figure 42: a) Composite image with colour code according to IPF and greyscale image quality filter overlaid. This scan was done at 3% measured elongation. Orientation of unit cell superimposed for certain grains(see also Figure 41). b) SE image from same area as in a after 5% measured elongation. c) Misorientation profile along torquise line A-B in image a. d) Misorientation profile along red line C-D in image a.

Grain 3 (beige in colour) is favourably oriented for basal-plane slip, with a Schmid factor of close to the maximum, 0,5. There is no sign of seamless slip transmission across the boundary. Figure 42 (c) shows that the misorientation between these grains is about 35°. The grain boundary appears brighter in the SE image. This indicates some topology caused by dislocation build up at the boundary to support the strain gradient across the boundary after deformation in grain 5. Grain boundaries as dislocation sources was discussed previously (chapter 2.2.2). Coupled with the interaction from the deformed grain 5, this is suspected to

induce deformation in grain 3. Clearly evident in the IQ map and the SE image at 4 and 5% elongation is the difference in slip line morphology between grain 5 and grain 3. The wide spacing of the lines indicate that plastic deformation is accommodated along fewer slip traces. The SE image(Figure 42 (b)) shows formation of topology at the surface, which reflects the slightly out-of-plane orientation of the basal slip system (see unit cell overlaid in Figure 42 (a)). Figure 34 shows the appearance of slip lines in the sample surface, with a clear "ledge" due to slip out of the surface plane. Such slip steps indicate dislocation(s) that have reached the surface and exited [43]. The small grain of type 8 also seems to hinder slip transmission, but acts as a stress riser to induce slip across the boundary.

On further loading, the colony structure, comprised of grains type 1 and 2, undergoes significant plastic deformation. Grain type 1 has orientation favouring prismatic slip, while grain type 2 favours pyramidal or basal slip. The boundaries within the colony seems to offer little resistance to deformation. Slip trace and orientation within the colony gives a more ambiguous picture of which slip systems are active.

In [42], basal slip was associated with finer, more densely spaced slip lines, while prismatic slip produced fewer and coarser slip traces with kinks and turns. This contrasts somewhat with what is observed here. Strain gradients across boundaries can induce slip along non-favoured slip systems [26]. Therefore, there is a possibility that prismatic slip is carried on across the boundary.

Sample plane: XZ

Figure 29 shows the position of the analysed area on the tensile specimen. Figure 31 shows in-situ scans, while Figure 43 presents the analysed area with absolute orientation of important grain types illustrated by unit cells. In this plane the column grains are perpendicular to the stress-axis.
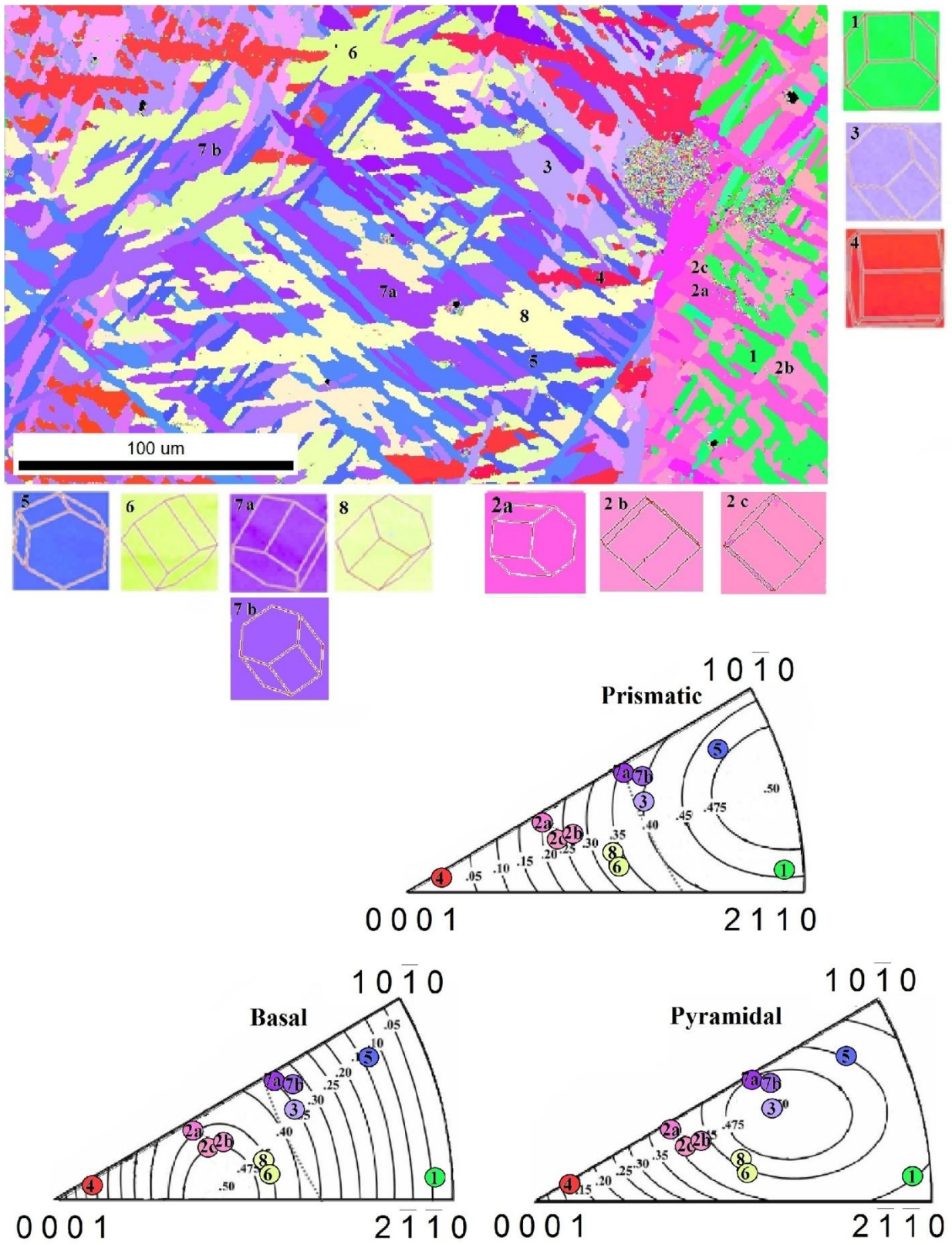
Figure 43: The IPF map for area subject to in-situ study related to the Schmid factor for different slip systems through IPF contour plots. Sample plane: XZ. Contour plots as presented in [42] with grain orientations for area scanned in-situ overlaid.

At 3% elongation slip lines are appearing in grains of type 5 and type 7a. Type 5 is oriented for prismatic slip. 7a has highest Schmid factor for pyramidal system, lies at equal Schmid factor for prismatic and basal. Again, determination of slip mechanism is difficult. Slip transmission seems to occur readily within the colony structure along the long dimension of plates. No clear indication of cross-slip (alteration between slip planes [26]) is observed, although the slip line is not strictly straight. This is shown in Figure 44. Deviations in the slip lines were attributed to stored GNDs in [43].
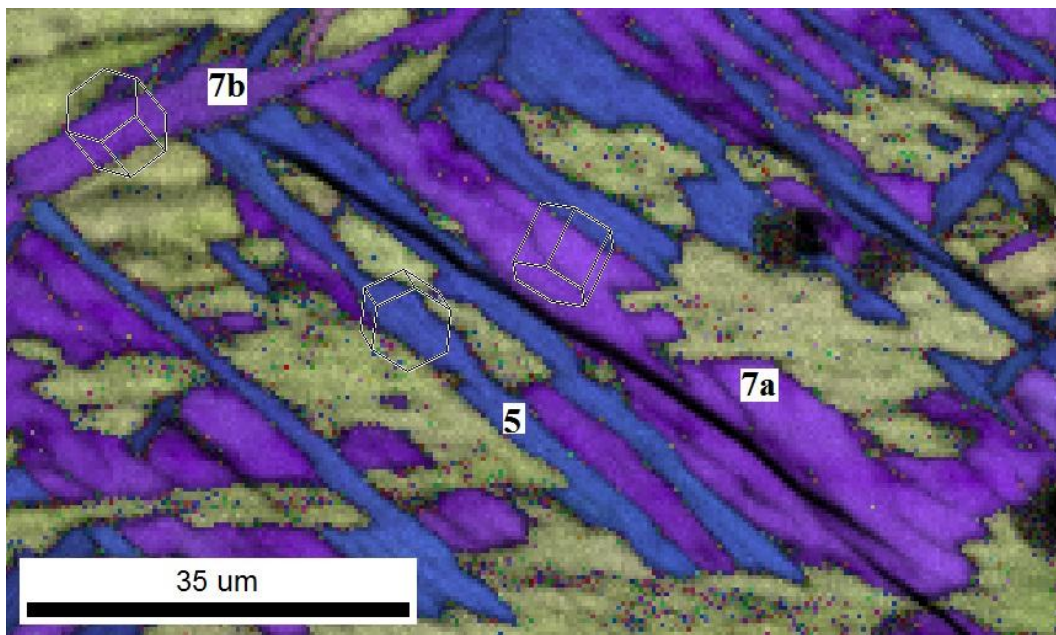
Figure 44: Slip lines crossing grain boundaries.

As grain 7b, belonging to another colony, impinges on plates of type 7a and 5, slip across the colony is halted. At 5% elongation in Figure 31, grain 7b appears slightly raised or embellished in the SE image, an indication of dislocation build up at this interface. A similar effect is seen in the region presented in Figure 45, cropped from the bottom right of the analysed area. At 5% elongation the perpendicular plate appears significantly brighter for a map overlaid with kernel average misorientation greyscale values (see chapter 2.3.2). This indicates a strain gradient within the plate, upheld by GNDs. Misorientation plots measured along the multicolour line indicated across the plate show how the misorientation is altered by straining. The effect is most prominent at the grain boundaries, which is in line with the theory of GND accumulation suggested in Figure 11. The IQ map at 5% elongation (middle right, Figure 45) shows how a slip band propagates through the perpendicular plate only after heavy build up of dislocations. This shows the strengthening effect of a relatively low angle grain boundary of about 10°.
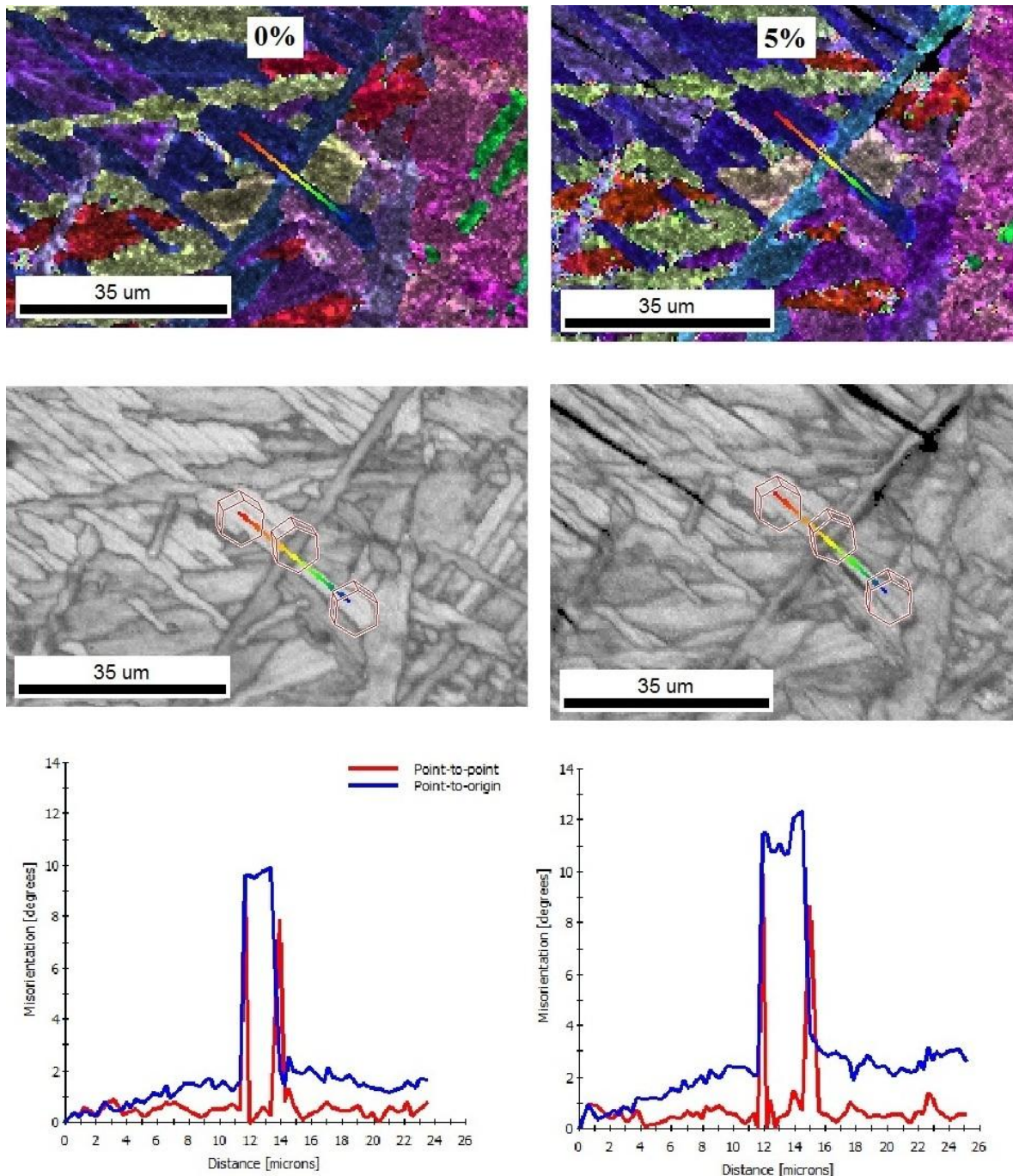
Figure 45: Comparing a section of the scan at 0% elongation(left side) and 5% elongation(right side). Top: IPF colour coded maps with Kernel average misorientation (0-1,5°) greyscale shading overlaid. Middle: IQ-map showing line for misorientation plots and unit cells. Bottom: Misorientation plots for the lines indicated above.

The build up of strain gradients at boundaries due to mismatch in deformation characteristics have been observed to form facets and initiate brittle fracture in Ti-6Al-4V [44]. What seems very clear from these observations is the relative ease of plastic deformation along entire colonies. [41] reports a tendency for easy shearing of interlamellar β-phase and slip transmission in colonies oriented for prismatic slip, while in colonies oriented for basal slip exhibited fine, homogeneous slip lines and no slip transmission. The

finely spaced slip lines of the basal system gives increased strain hardening due to the higher rate of cross slip and slip band interaction. This non planar slip increases dislocation density.

The deformation behaviour in this sample is clearly segmented due to the presence of a previous β-grain boundary. The neighbouring colony to the right, consisting of grains of type 1 and 2, undergoes severe plastic deformation. This is obvious if one looks at the SE image at 5% elongation Figure 31. Deformation is mainly accommodated by prismatic slip in grains of type 1 (green). Localised heavy deformation is seen along boundaries between undeformed grains of type 2 and the actively deforming grains of type 1. Compensation for this mismatch through generation of GNDs is likely to cause the distinctive topology in this region. There is also evidence of localised deformation along the previous β-grain boundary. This could be attributed to a colony-wide mismatch in deformation characteristics.

Figure 28 shows two regions with widely differing behaviour. The topology in area B is mostly unchanged, while the neighbouring colony, and the grain boundary α in-between, is subject to heavy deformation. Area A represents a colony very similar to what was seen on the right hand side in Figure 43. Extensive slip along plates oriented for prismatic activation occurs here as well (green grains). The colony in Area B should overall be more favourably oriented for deformation if one looks at the texture plots. The prevailing orientations in this area coincide with easy activation of basal and prismatic respectively. The influence of *slip length* seems to be at play here. Grains with active slip directions aligned with the long dimension of the plate are more likely to accommodate deformation.

β-Ti exhibits higher strength than α-Ti within two-phase microstructures. It is up to 3 times harder than α-Ti [45]. Studies of single colony deformation in α+β alloys tend to focus on the transmission of slip across interlamellar β. Observed anisotropy in colonies has been attributed to the direction of slip in relation to β-platelets. Slip normal to platelets is more difficult [45]. The low (detected) β-content in the studied samples is not expected to have a large influence on deformation characteristics. Even so, anisotropy beyond what can be explained by Schmid factors or texture is observed in this study. The direction of slip compared to the spatial orientation of colony plates seems like a significant factor, independent of retained β-phase.

Figure 27 shows how small β-inclusions disappear during straining. This could be attributed to signal degradation and non-detection as strain increases. However, transformation into strain induced martensite is commonly observed, and suspected to be the case here. The low activation stress associated with this transformation (discussed in chapters 2.1.2 and 5.3.1) suggests this could occur at these strain levels.

5.2.2 Macro level
Sample plane: ZX

Figure 25 indicates no significant changes at the macro level in these samples. Fairly homogeneous deformation along the sample is observed.

Sample plane: XZ

This sample exhibited localised deformation at the macro level. Figure 46 represents an attempt to envisage how slip activity would be connected to stress state in the necking region. The complex triaxial stress state introduced by necking would impart a compressive stress component along the width of the tensile specimen. The same figures for basal slip are presented in appendix F. Orientations favouring basal slip were more evenly spread out across the sample (see Figure 54). Therefore, the prevalence of easily activated prismatic slip planes in certain segments is identified as a significant feature. The highlighted regions seem to coincide quite accurately with the areas of most severe deformation. Orientation data is assumed to be reliant, even if heavy deformation and surface topology degrades and deflects the EBSD signal. The orientations indicated in the scan performed post-strain matches what was achieved pre-strain quite accurately. For some discussion on surface topology and its influence on reliability, see [43].
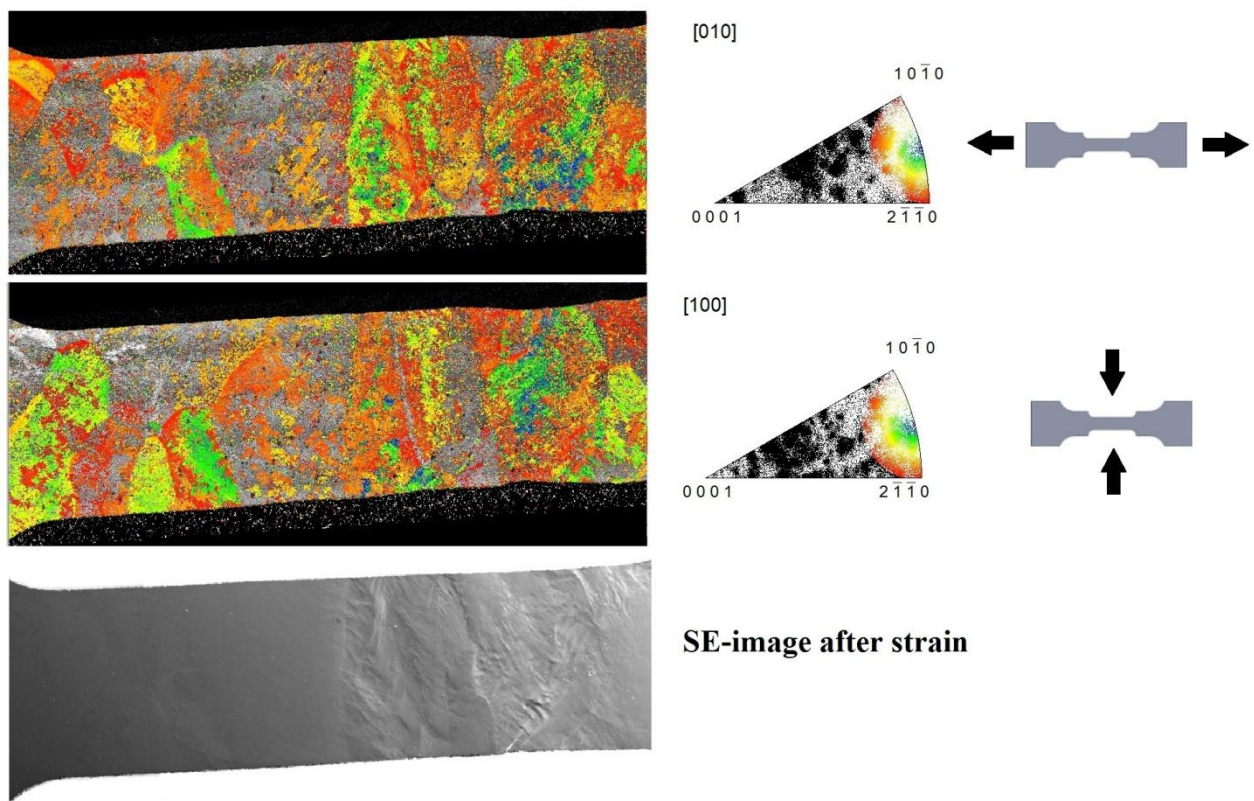
Figure 46: Grains oriented favourably for prism slip under tensile forces (top) and compressive forces (bottom) are highlighted according to the colour contours indicated in the discrete IPFs (Blue= max Schmid factor). SE-image is also included. See Figure 30 for complete image.

[26] describes necking in a sheet specimen occurring in two stages. Firstly, the *diffuse* neck forms, giving a contraction along the width of the specimen over a length which is much larger than the sheet thickness. The second stage is a localised neck which gives contraction along the thickness of the specimen, in a diagonal band of width about equal to sample thickness. The nature of the necked region in Figure 30 and Figure 29 bears some

resemblance to this description, with tendencies for diagonal banding extending from the cracked region. The occurrence of a surface crack in the sample is discussed in chapter 5.3.1.

The in-situ tests of this sample was discussed in the previous chapter (sample plane XZ). See Figure 30 and Figure 29 for the placement of the analysed area. The area lies at the border between the right hand side of the sample, associated with severe deformation, and the left hand side, showing minimal signs of deformation on the surface. Here the mechanism of deformation in a similar colony to the cracked area was observed directly. Heavy slip along prismatic planes, counteracted by slip resistance and stress build-up in differently oriented grains. Localized heavy strain hardening is expected to have occurred in the necked region. This would contribute to crack formation if further plastic deformation is not accommodated in other segments of the sample.

Sample plane: YZ

The microstructure in this plane is similar to what is observed for XZ. The column grains are generally slightly narrower (ref. Figure 32). Figure 35 and Figure 36 show how the heavily segmented strain response causes ridges to form at the column grain boundaries. These are attributed to the appearance and motion of GNDs to compensate for the significant mismatch in deformation dynamics between regions.

5.2.3 Qualitative assessment of mechanical properties

Stress-strain curves are presented in Figure 37 due to reasons that will be expanded upon in chapter 5.3.3, these are by no means exact, quantitative measurements. They still give an indication of the relative tensile properties. The tensile sample lying perpendicular to the welded layers (plane ZX) displayed the lowest flow stress. Overall texture plots of the strained areas are presented in Figure 47.
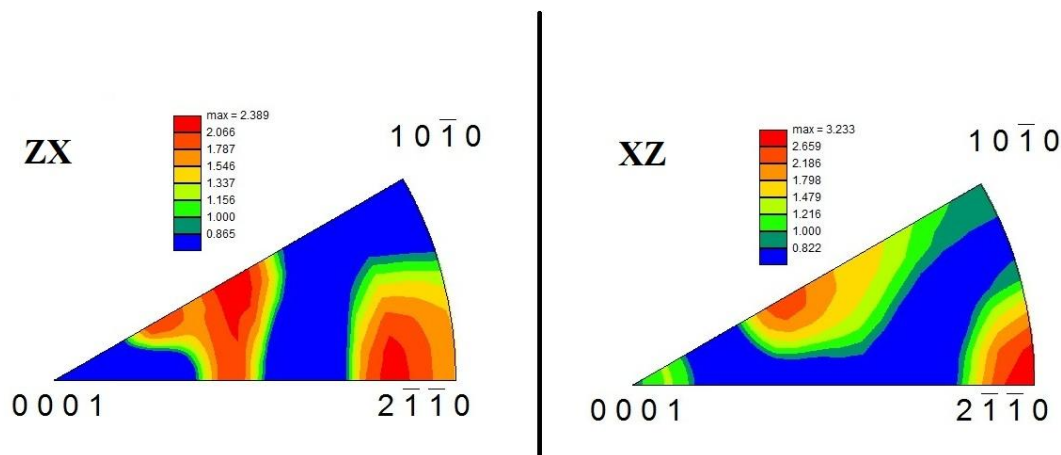

Figure 47: Texture plots for tensile samples, referenced to stress axis.

Although these plots could serve to explain the lower strength in ZX, the previous discussions have shown that pronounced heterogeneous deformation mechanisms dominate. The moderate two-component texture in ZX does indicate easy activation of

prismatic and basal systems in large areas of the sample. As the ZX sample area is strongly dominated by few (two) column grains, the uniform deformation characteristics of the colony structure within would give very little deformation mismatch, grain interaction and work hardening. The result is behaviour reminiscent of one single microstructural unit, analogous to single crystal material.

Samples XZ and YZ exhibit higher strength, but are suspected to posses greatly reduced ductility due to the segmented deformation behaviour. This effect would be especially detrimental in thin walled components. Thicker sections would comprise several column grains, which does alleviate this single colony effect.

Origins of "soft" colonies and possible consequences of thermal cycles

The growth of column grains such as in Figure 21, form far-reaching nucleation surfaces along Z-direction. They show a preference for growth along $<001>_\beta$-direction. Grain boundary α nucleates at this surface, and grow towards the column grain interior. There seems to be a preference for orientations with prismatic planes as aligned as possible with the grain boundary plane. The preferred alignment leads to variant selection within the confines of BOR. As growth proceeds, the growth morphology changes to plates. Growth direction of plates is usually in the basal plane. As dictated by BOR, the basal plane is parallel to $\{110\}_\beta$, meaning plates are likely to grow at an angle of about 45° with the long dimension of column grains. This produces a morphology exemplified by Figure 21. The structure consists of plates with the active basal slip systems (prismatic mainly) oriented at a favourable 45° angle, both relative to Z and X directions.

The severe deformation highly localised to coarse slip bands may also be brought about by ordering reactions after aging effects. As mentioned in chapter 2.1 and 2.2.1, ordering of Al and O does occur, and may influence slip characteristics greatly. This decreases strain hardening significantly due to the lack of interaction between dislocations in these widely spaced dislocation "highways".

A low β-content is most probably caused by decomposition after repeated thermal cycles. Higher contents of finely distributed β-grains would serve as a strengthening agent.

5.3   Experimental approach

5.3.1   Sample preparation

Preserving the residual β-phase after sample preparation to produce unambiguous diffraction patterns has proven difficult. Although not central to this work, the β-contents suggested by the EBSD scans are assumed to contain artefacts. In Figure 27 (see Figure 49 in appendix for more thorough phase distribution maps) β-phase is scarce and generally gives low diffraction pattern quality. Etching of the sample prior to EBSD analysis, in the manner described in chapter 3.1.3 and followed by thorough cleaning, is shown to make retained β-phase more apparent at a high CI-value. This is clear in Figure 50 (appendix). As discussed in the section covering martensitic transformations (in chapter 2.1.2) the martensitic reaction proceeds at relatively low stress levels. The "back stress", meaning the forces opposing the shear based martensitic transformation, is fairly modest. This again means that any retained, metastable β-phase, which has a chemical driving force for transformation to α, can undergo a transformation to martensite assisted by applied stress or deformation. It has been reported that such transformations can occur during mechanical grinding and polishing of Titanium samples[6]. This would obscure the actual phase contents. The issue of detecting this is also somewhat complicated. The fine martensitic structures are difficult to resolve and distinguish by EBSD techniques. The polishing regime presented in chapter 3.1.2 and 3.2.2 leaves the surface almost completely free of any contours or contrast. Detection of grain morphology by optical microscope or SEM investigations are not possible without etching of the sample (Could possibly identify martensite by use of backscattered electron imaging, not applied here) . The etching may in turn alter the surface slightly, so that artefacts are not as apparent. The Chemical-Mechanical preparation procedure was deemed preferential to electropolishing due to the possibility of preserving sample edges. During electropolishing, edges or corners are subject to significantly higher current densities, giving localised removal of material and uneven surfaces at the edge. The preservation of edges was of interest due to the possibility of EBSD comboscan to cover a large macroscopic area including the outer edges. This made it possible to attain diffraction patterns at the outer edges and correlating these with any apparent contraction and deformation of the tensile specimens side faces.

The tensile specimen geometry (see Figure 15) produces sharp edges which will act as stress risers. The study of actual crack initiation was beyond the scope of this study. Therefore no real significance should be attributed to the exact placement of the crack formed in tensile specimen of type XZ (see Figure 30). The side surfaces of the specimen are also untreated, meaning they have a certain surface roughness from machining. Again, this would influence localization of crack initiation. In [36] the effects of electrical discharge machining on Ti-6Al-4V were reported. A rough surface with microcracks, resolidified splats and debris were found. Just below the surface a thin layer (approximately 50 μm) of hard martensitic α' had formed due to the thermal input and high cooling during machining. Carbides were found in the outer layer, and assumed to stem from reaction with the dielectric fluid. The magnitude of these features depend strongly on machining parameters. Assessment of exact

parameters and further discussion of surface roughness effects are beyond the scope of this report, but as evident in Figure 30, there is considerable surface roughness.

5.3.2 EBSD and orientation imaging

A high rate of pattern aquisition is obtainable during offline EBSD analysis, 350-400 pps in this study, but rates as high as 1000pps are feasible[46]. This allowed the mapping of relatively large areas, while strain effects were clearly visible. Continuous slip bands over 200 µm in length were observed (ref. Figure 26). This reflects the large slip length in the highly elongated grains, and requires large-area analysis if grain interaction effects is to be observed.

Cross-correlation analysis of diffraction patterns promises to allow detection of minute shifts in patterns[34, 43, 47]. The application of such a methodology would allow more precise mapping of intragranular elastic and plastic strain. This would be highly useful, especially in coarse grained, anisotropic materials to gain a more complete picture of the relation between microstructure and properties.

5.3.3 In-situ testing equipment

Looking at Figure 37, there is clearly some tightening/displacement effects. As the strain measurement is not done through a dilatometer mounted directly, but by counting the turns of the motor, the whole mechanism will have some influence on the curves. The slope of the elastic region is not linear and very slight compared to the expected E-modulus of around 110 GPa. This makes the tensile rig a "soft" testing machine([26]), meaning that exact stress-strain curves are not replicated as reliably . The degree of displacement also varies slightly with each test. The intension is not for the tests to be quantitative, and the measured values should only be taken as indications of stress-strain levels. As a comparison between the samples they should have some worth however.

Although the machine is set in displacement controlled mode, relaxation of stresses as the motor is stopped are accompanied by an indicated slight elongation of 0,1% (see Figure 37). This is again attributed to the uncertainty of the strain measurements.

6 Conclusion

The combination of an in-situ tensile testing rig and high speed EBSD data collection allows for extensive insight into the intricacies of the ALM microstructure and its behaviour during loading. Deformation behaviour observed at the microscopic level has significant bearing on the macroscopic strain response. This is caused by the far-reaching influence of columnar solidification structures, brought about by unidirectional heat flow and epitaxial growth. Through preferred growth directions, energetically favourable crystallographic alignment and strict adherence to Burger's orientation relationship, certain types of colony structures are repeatedly produced. During in-situ tensile tests, the following was observed:

- The most severe deformation is associated with prismatic slip along coarse, widely spaced slip bands. There are some indications that the prismatic systems take precedence even in grains with less favourable orientations.
- Certain colonies act as microstructural units, where colony-wide slip occurs readily. While others exhibit more internal deformation mismatch leading to local stress concentration and strain gradients.
- The spatial orientation of plates within a colony is of great importance for dislocation motion. Deformation bands are often restricted to the long dimension of plates, where the slip length is large and orientation is frequently favourable due to the preferred growth direction of plates.
- Coarse grain boundary α does not appear significantly weaker than coarse colonies.
- At the macro level, inhomogeneous deformation manifests itself through a highly segmented strain response. With the stress axis perpendicular to the columnar previous β-grains, deformation may become highly localized in column grains inhabited by the weaker colonies. Loading along previous β-grains gives more uniform deformation but lower strength due to texture effects.

Finally, the formation of certain microstructural configurations can be rationalised through a qualitative consideration of the process and known transformation and growth characteristics, while a more rigorous description requires quantitative process data and systematic analysis. Suggestions regarding this, and further implementation of in-situ techniques will be presented in the next chapter.

7   Future work

Attaining thermal data from the production process, which in turn can be used to design an in-situ thermal treatment could greatly contribute in these studies. The capabilities of the equipment at NTNU currently allows heating up to 600°C in a special heating stage arrangement. Rapid cooling is also possible. Temperatures in the single phase β-region are currently not attainable. A thermal cycle with peak temperatures high up in the α-Ti single phase region could give good simulations of reheating of previous layers in the ALM process.

Preparation of sample materials with systematic analysis in mind would be very beneficial. Reducing the number of variables by depositing simple geometries (i.e. single weld walls etc.) would aid initial process investigations greatly.

In-situ tensile tests can also be carried out at low(-60°C) or elevated(around 500°C) temperatures to evaluate the performance in severe conditions.

In addition, the prospect of simulating low cycle fatigue in a setup similar to the tensile stage is alluring. OIM would be greatly applicable here as well, due to the significance of grain orientation in cyclic loading for Titanium [29].

Based on this work, different methods of sample preparation should be looked into. By doing systematic tests utilising chemical-mechanical polishing, electropolishing and ion milling with varying parameters. This in order to quantify the tendencies for artefacts, i.e. pressure induced martensitic transformation and selective removal of certain phases.

Important microstructural features related to ordering reactions, e.g. intermetallic phases such as Ti_3Al and Hydrides, remains to be studied in detail. Ordering of Oxygen is also known to influence deformation behaviour of α-Ti to a large extent[14].

The use of hardness test indents to mark and measure distances would allow for accurate elongation data with the current tensile stage set-up.

Strain mapping through application of cross-correlation or similar method would greatly increase the amount of information gained in such studies.

8   References

1.   Chater, J., *Titanium and aerospace: two interdependent industries.* Stainless Steel World, 2009(November): p. 4.

2.   Donachie, J.M.J., *Titanium - A Technical Guide (2nd Edition)*, ASM International.

3.   Zelinski, P. *Introduction To A Series*. How To Machine Aircraft Titanium, Modern Machine Shop 2009; Available from: http://www.mmsonline.com/articles/how-to-machine-aircraft-titanium-introduction-to-a-series.

4.   Seong, S., Obaid Younossi, Benjamin W. Goldsmith, Thomas Lang and Michael J. Neumann. Also available in print form., *Titanium: Industrial Base, Price Trends, and Technology Initiatives.* 2009, Santa Monica: CA: RAND Corporation

5.   Mathisen, M.B., *Direct metal deposition of Ti grade 2, Characterisation of microstructure and mechanical properties.*, in *Department of Materials Science*. 2011, NTNU: Trondheim.

6.   Lütjering, G. and J.C. Williams, *Titanium*. 2007, Berlin, Heidelberg: Springer-Verlag.

7.   Burgers, W.G., *On the process of transition of the cubic-body-centered modification into the hexagonal-close-packed modification of zirconium.* Physica, 1934. 1(7–12): p. 561-586.

8.   Banerjee, S. and P. Mukhopadhyay, *Phase transformations: examples from titanium and zirconium alloys*. 2007, Amsterdam: Elsevier. xxii, 813 s.

9.   Ivasishin, O.M. and R.V. Teliovich, *Potential of rapid heat treatment of titanium alloys and steels.* Materials Science and Engineering: A, 1999. 263(2): p. 142-154.

10.   Elmer, J.W., et al., *Phase transformation dynamics during welding of Ti-6Al-4V.* Journal of Applied Physics, 2004. 95(12): p. 8327-8339.

11.   Williams, J., *AFRL Ti Lect #1-5 090203*. 2009, Ohio State University: Ohio.

12.   Okazaki, K. and H. Conrad, *Effects of interstitial content and grain size on the strength of titanium at low temperatures.* Acta Metallurgica, 1973. 21(8): p. 1117-1129.

13.   Wriedt, J.L.M.a.H.A., *ASM Metals Handbook.* 1987. vol. 3: p. p. 356.

14.   Welsch, G. and W. Bunk, *Deformation modes of the α-phase of ti-6al-4v as a function of oxygen concentration and aging temperature.* Metallurgical and Materials Transactions A, 1982. 13(5): p. 889-899.

15.   Ahmed, T. and H.J. Rack, *Phase transformations during cooling in α + β titanium alloys.* Materials Science and Engineering A, 1998. 243(1-2): p. 206-211.

16.   Furuhara, T., T. Ogawa, and T. Maki, *Atomic structure of interphase boundary of an α precipitate plate in a β Ti[sbnd]Cr alloy.* Philosophical Magazine Letters, 1995. 72(3): p. 175-183.

17.   Gil, F.J., et al., *Formation of α-Widmanstätten structure: effects of grain size and cooling rate on the Widmanstätten morphologies and on the mechanical properties in Ti6Al4V alloy.* Journal of Alloys and Compounds, 2001. 329(1–2): p. 142-152.

18.   Cass, T.R., R.W. Quinn, and W.R. Spencer, *Growth of hexagonal titanium and titanium-aluminum single crystals.* Journal of Crystal Growth, 1968. 2(6): p. 413-416.

19.   Aaronson, H.I., et al., *Sympathetic nucleation: an overview.* Materials Science and Engineering: B, 1995. 32(3): p. 107-123.

20.   Kurz, W. and D.J. Fisher, *Fundamentals of solidification*. 1998, Uetikon-Zuerich: Trans Tech Publications. 305 s.

21.   Porter, D.A., K.E. Easterling, and M.Y. Sherif, *Phase transformations in metals and alloys*. 2009, Boca Raton, Fla.: CRC Press. XVI, 520 s.

22.   Rösler, J., M. Bäker, and H. Harders, *Mechanical Behaviour of Engineering Materials: Metals, Ceramics, Polymers, and Composites*. 2007, Berlin, Heidelberg: Springer-Verlag Berlin Heidelberg.

23.   Bieler, T.R. and S.L. Semiatin, *The origins of heterogeneous deformation during primary hot working of Ti–6Al–4V.* International Journal of Plasticity, 2002. 18(9): p. 1165-1189.

24.   Williams, J., R. Baggerly, and N. Paton, *Deformation behavior of HCP Ti-Al alloy single crystals.* Metallurgical and Materials Transactions A, 2002. 33(13): p. 837-850.

25.   Szczepanski, C.J., *The Role of Microstructural Variability on the Very High Cycle Fatigue Lifetime Variability of the alpha+beta Titanium Alloy, Ti-6Al-2Sn-4Zr-6Mo*. 2008, The University of Michigan.

26.   Dieter, G.E. and D. Bacon, *Mechanical metallurgy*. 1988, London: McGraw-Hill. XXIII, 751 s.

27.   Wu, X., et al., *Modeling Anisotropic Stress-Strain Response and Crystallographic Texture Evolution in <i>α</i>-Titanium during Large Plastic Deformation using Taylor-Type Models: Influence of Initial Texture and Purity.* Metallurgical and Materials Transactions A, 2008. 39(12): p. 3046-3054.

28.   Betsofen, S.Y., et al., *Texture and anisotropy in the mechanical properties of titanium alloys caused by the mechanism of plastic deformation.* Russian Metallurgy (Metally), 2007. 2007(5): p. 387-393.

29.   Dunne, F.P.E., A. Walker, and D. Rugg, *A systematic study of hcp crystal orientation and morphology effects in polycrystal deformation and fatigue.* Proceedings of the Royal Society A: Mathematical, Physical and Engineering Science, 2007. 463(2082): p. 1467-1489.

30.   Dunne, F.P.E., D. Rugg, and A. Walker, *Lengthscale-dependent, elastically anisotropic, physically-based hcp crystal plasticity: Application to cold-dwell fatigue in Ti alloys.* International Journal of Plasticity, 2007. 23(6): p. 1061-1083.

31.   Bullough, R., Philosophical Magazine 1964. Vol. 9.

32.   Ashby, M.F., *The deformation of plastically non-homogeneous materials.* Philosophical Magazine, 1970. 21(170): p. 399-424.

33.   Li, J.C.M., *Microstructure and properties of materials*. 1996, Singapore: World Scientific. 2 b.

34.   Schwartz, A.J., et al., *Electron Backscatter Diffraction in Materials Science*. 2009, Boston, MA: Springer Science+Business Media, LLC.

35.   Bill Taylor (Struers Ltd, G., Elisabeth Weidmann (Struers A/S, Copenhagen), *Application Note: Metallographic preparation of titanium.* 2008.

36.   Hasçalık, A. and U. Çaydaş, *Electrical discharge machining of titanium alloy (Ti–6Al–4V).* Applied Surface Science, 2007. 253(22): p. 9007-9016.

37.   Pedersen, J.H., *In situ strekkforsøk med EBSD karakterisering av HSLA-stål ved romtemperatur og -60 °C (In norwegian)*, in *Institute for Materials Science*. 2011, NTNU: Trondheim.

38.   Kobryn, P.A., E.H. Moore, and S.L. Semiatin, *Effect of laser power and traverse speed on microstructure, porosity, and build height in laser-deposited Ti-6Al-4V.* Scripta Materialia, 2000. 43(4): p. 299-305.

39.   Baufeld, B., O.V.d. Biest, and R. Gault, *Additive manufacturing of Ti–6Al–4V components by shaped metal deposition: Microstructure and mechanical properties.* Materials & Design, 2010. 31, Supplement 1(0): p. S106-S111.

40.   Majdic, M. and G. Ziegler, *Effect of the Metastable beta -Phase Transformations in the Ti-6Al-4V Alloy.* EINFLUSS DER METASTABILEN beta -PHASE AUF DAS UMWANDLUNGSVERHALTEN DER TITANLEGIERUNG TiAl6V4., 1973. 64(11): p. 751-758.

41.   Savage, M.F., et al., *Deformation mechanisms and microtensile behavior of single colony Ti–6242Si.* Materials Science and Engineering: A, 2001. 319–321(0): p. 398-403.

42.   Bridier, F., P. Villechaise, and J. Mendez, *Analysis of the different slip systems activated by tension in a α/β titanium alloy in relation with local crystallographic orientation.* Acta Materialia, 2005. 53(3): p. 555-567.

43.   Littlewood, P.D., T.B. Britton, and A.J. Wilkinson, *Geometrically necessary dislocation density distributions in Ti–6Al–4V deformed in tension.* Acta Materialia, 2011. 59(16): p. 6489-6500.

44.   Evans, W.J., J.P. Jones, and M.T. Whittaker, *Texture effects under tension and torsion loading conditions in titanium alloys.* International Journal of Fatigue, 2005. 27(10-12): p. 1244-1250.

45.   Suri, S., et al., *Room temperature deformation and mechanisms of slip transmission in oriented single-colony crystals of an α/β titanium alloy.* Acta Materialia, 1999. 47(3): p. 1019-1034.

46.   Schwarzer, R.A. and J. Hjelen, *Orientation microscopy with fast EBSD.* Materials Science and Technology, 2010. 26(6): p. 646-649.

47.   A. J. Wilkinson*, G.M.a.D.J.D., *High resolution mapping of strains and rotations using electron backscatter diffraction.* Materials Science and Technology, 2006 22(11): p. 1271-1278

9   Appendix

Appendix A

In uniaxial tension, the resolved shear stress acting on a plane is defined by the relation [22]:

$$\tau_{RSS} = \sigma cos\lambda cos\theta$$

where:

σ is the tensile stress acting on the cross section of the material
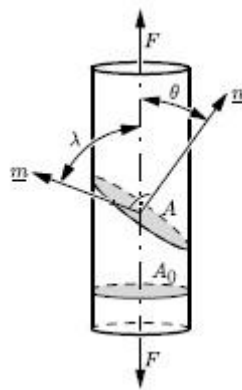
λ and θ are the angles as defined in Figure 48.

Figure 48: The resolved shear stress acting on an inclined plane under tensile stress[22].

$(cos\lambda cos\theta)$ =m is also referred to as the Schmid factor.

Appendix B

EBSD combined scans. Parameters.

Accelerating voltage	20 kV
Aperture	60 μm , High Current mode
Working distance	23mm
Magnification	75X
Tilt angle	70°
Rate of collection	40 pps
Binning	8x8
Exposure time	0,02
Step size	5-10 μm
Scan times	4-8 hours

Appendix C

In-situ scans at strain intervals:

Accelerating voltage	20 kV
Working distance	23 mm
Magnification	200-350 X
Aperture	300 μm , High Current Mode
Tilt angle	70°
Step size	0,2-0,6 μm
Frame rate	300
Resolution	120x120
Exposure time	3283
Gain	4
Scan times	15-20 min

Hough transform:

Hough type	Classic
Hough resolution	Low
Convolution mask	9x9
Min peak magnitude	5
Min pek distance	10
Peak symmetry	0,5
Binned pattern size	120
Theta step size	1°
Pho fraction	90%
Max peak count	7
Min peak count	3

Appendix D

CI:

$$\frac{f1 - f2}{f2}$$

where:

f_1=probability (or "votes") for the most likely solution

f_2= probability (or "votes") for the second most likely solution

Appendix F

a)

Phase	Total Fraction	Partition Fraction
▮ Titanium (Alpha)	0.982	0.982
▮ Titanium (Beta)	0.018	0.018

5 mm

b)

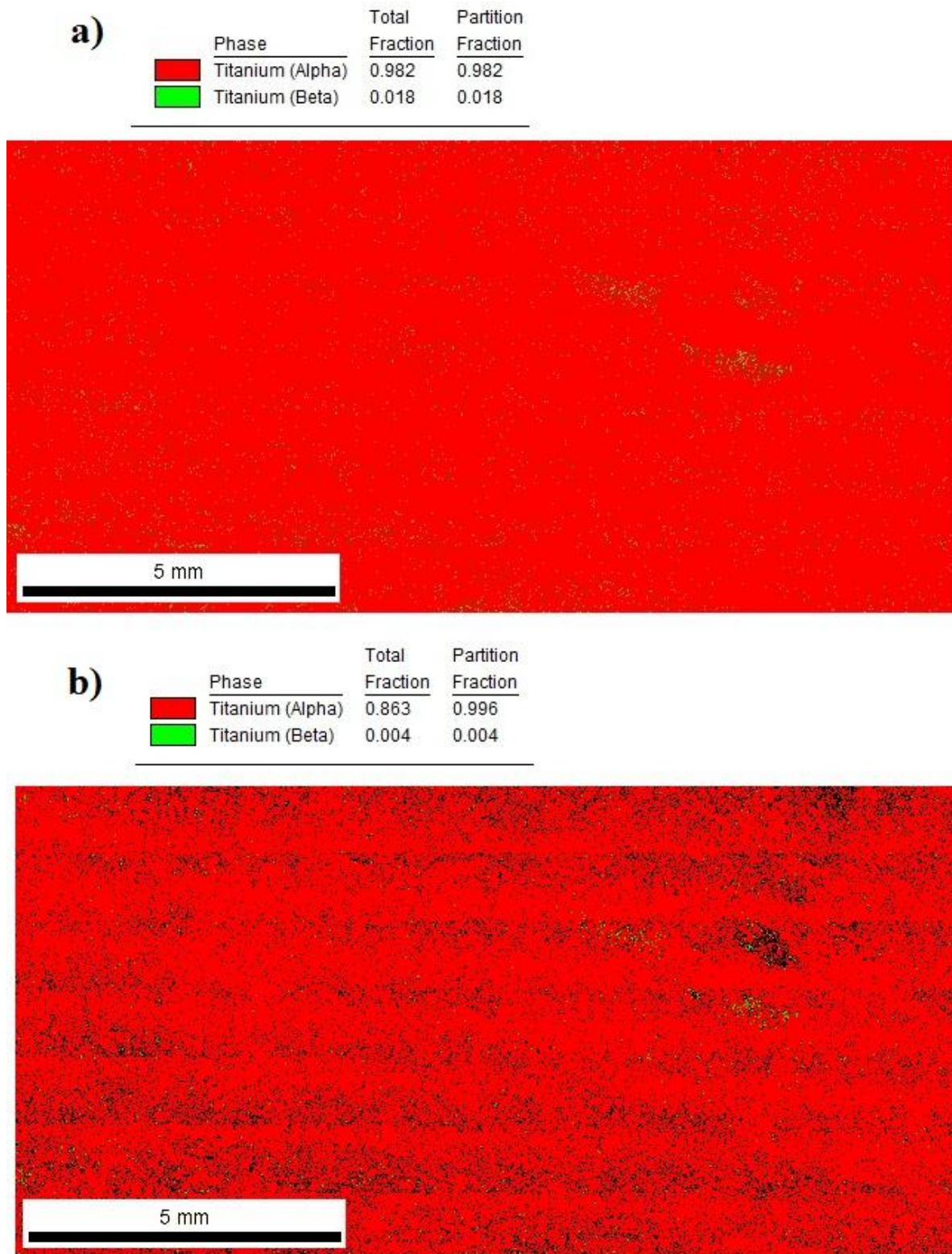| Phase	Total Fraction	Partition Fraction
▮ Titanium (Alpha)	0.863	0.996
▮ Titanium (Beta)	0.004	0.004

5 mm

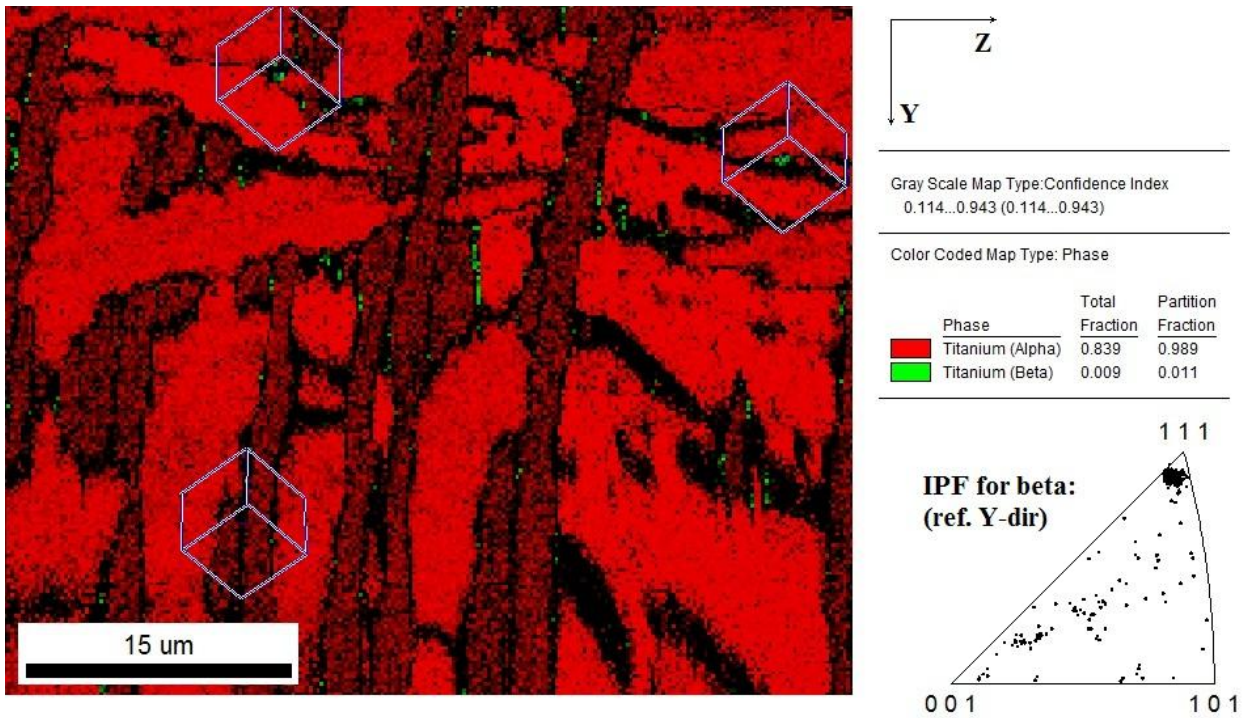**Figure 49: Phase distribution in comboscan (presented in Figure 19). a) Overall distribution, average CI is 0,49 in this scan. b) Points with CI below 0,1 have been removed (black).**

Figure 50: Etching previous to EBSD analysis gives a clearer image of β-phase content. Phase map is overlaid with greyscale map according to CI-value. Lighter areas represent high CI-values. All β-remnants share a common orientation.
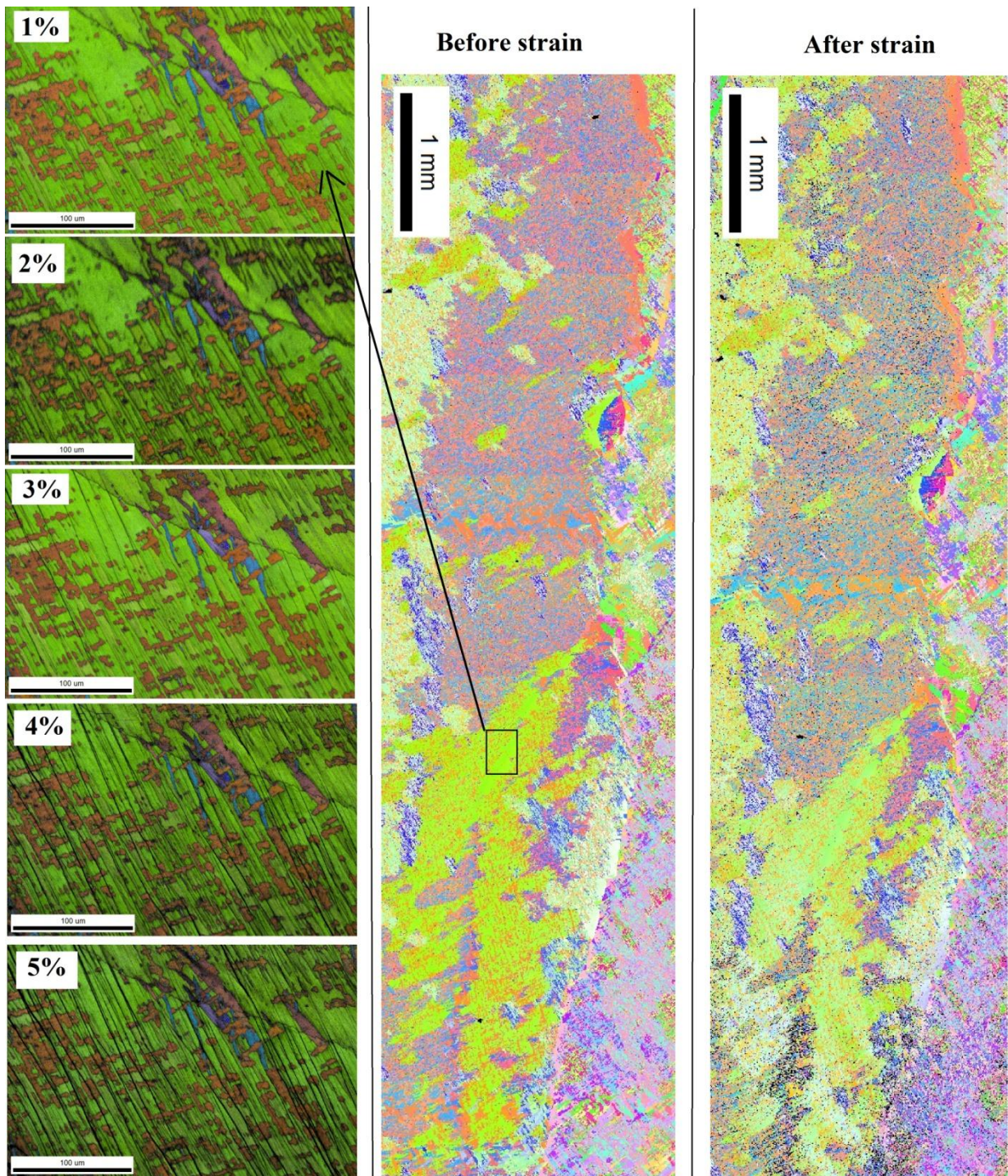
Plane: ZX (2)

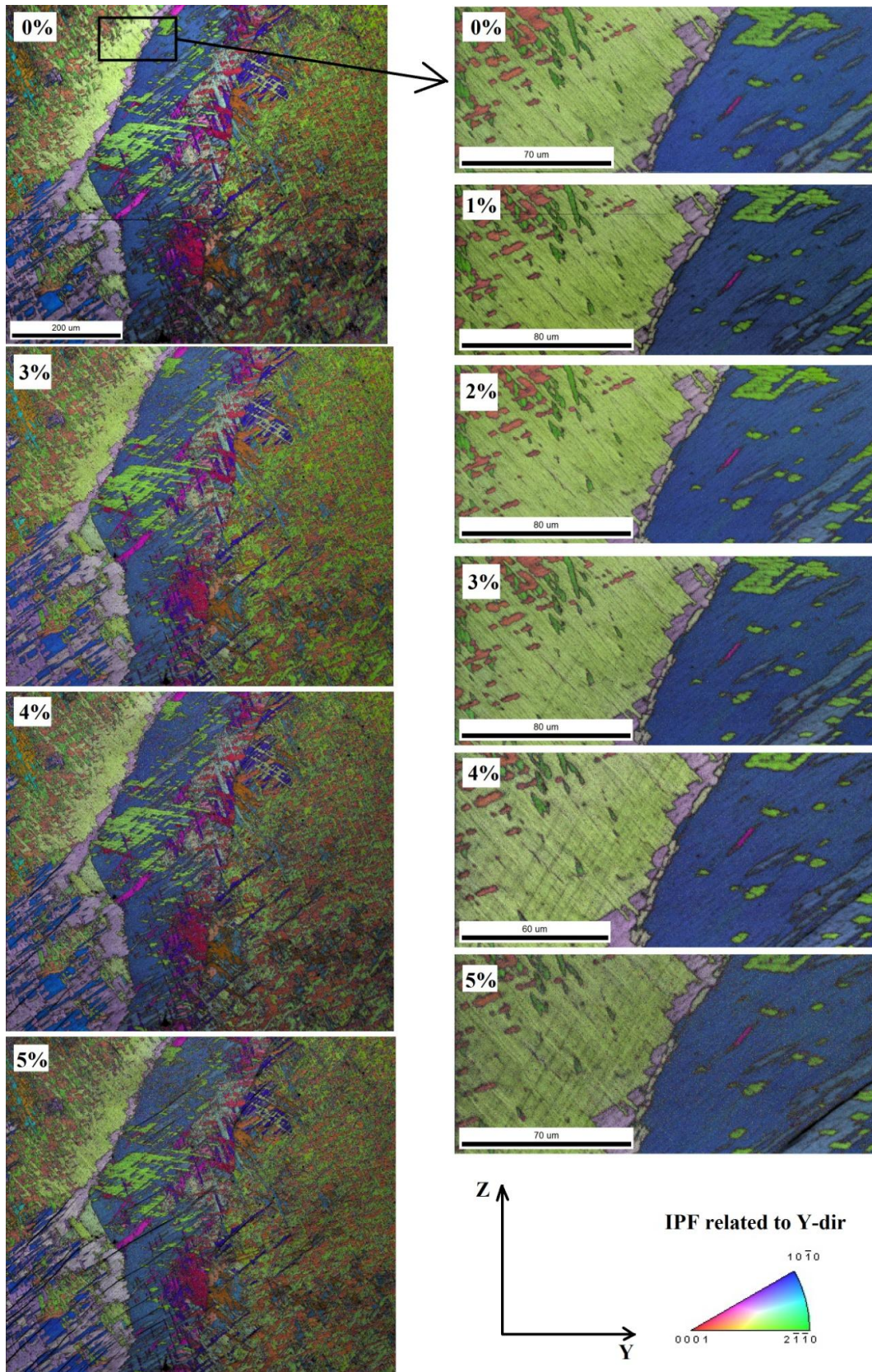Figure 51: In-situ scans on sample plane ZX. Comboscans before and after presented to the right.

Plane: YZ

Figure 52: In-situ scans from sample from plane YZ. Composite images with IQ greyscale values and IPF colours. See Figure 32 for macroscan and location of this region.
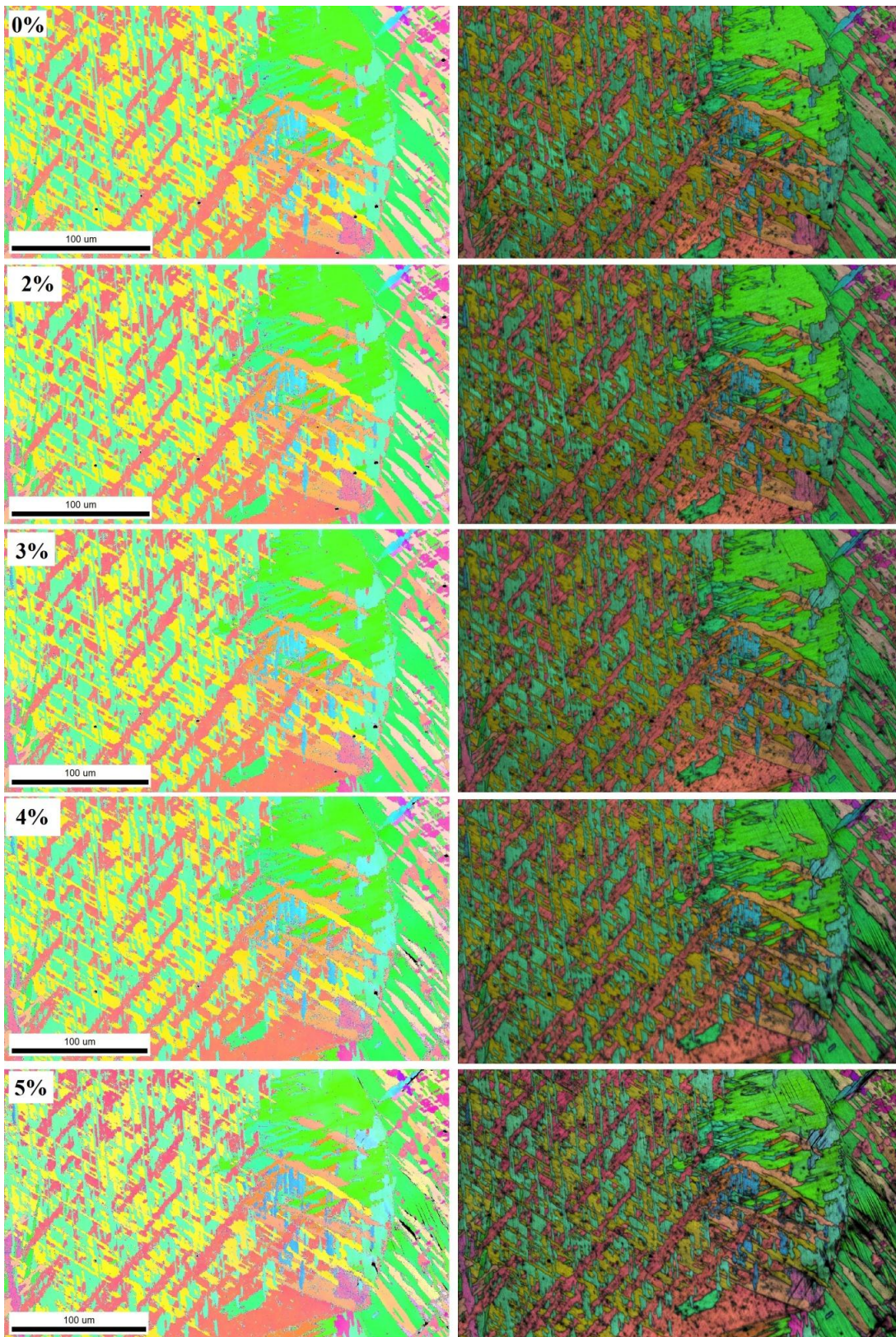
Plane: ZX (3)

Figure 53: In-situ scans from plane ZX. Left column: IPF maps. Right column: IPF maps with IQ superimposed.
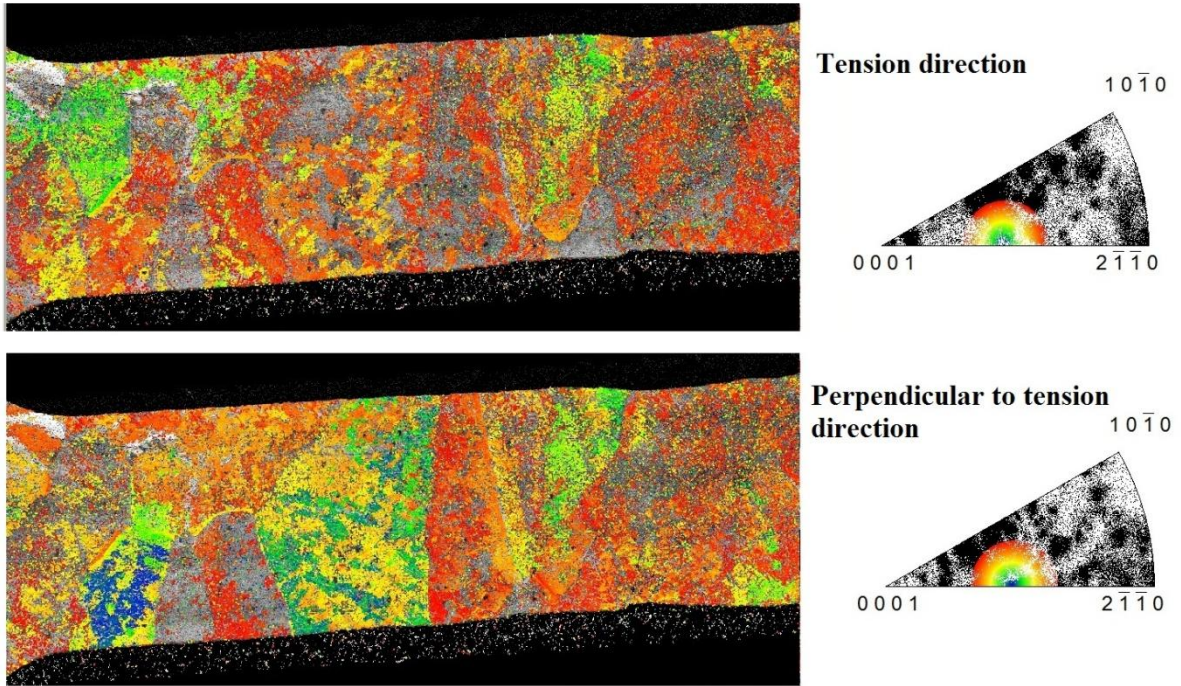
Plane: XZ

Figure 54: Highlighted are grains which are oriented favourably for activation of basal slip upon loading along tension direction(horizontal) or perpendicular direction(vertical).